REFINING OUR UNDERSTANDING OF THE
HEMATOPOIETIC STEM CELL NICHE

APPROVED BY SUPERVISORY COMMITTEE

Sean J. Morrison, Ph.D.

Ralph J. Deberardinis, M.D., Ph.D.

Michael Buszczak, Ph.D.

Eric N. Olson, Ph.D.

DEDICATION

For laughing at all my bad jokes; for never letting me over-interpret my data; for getting me ice when I burned my hands at four in the morning, I dedicate this dissertation to Malea Murphy. If I ever again have a co-worker half as talented and easy to work with as you, I'll count myself very lucky.

I want to thank my mentor, Sean Morrison, for continuing to support me even when everything was going wrong. Your unfaltering concern over my success kept me on the right track. Your guidance was always appreciated. Thank you.

I want to thank David Peyer and Kyle Lawson. I had to choose between my dissertation and our company, and you two were always supportive even as I abandoned all of our hard work. And finally, I would like to thank Karen Leung for critically reading this manuscript and putting up with me through the writing process.

REFINING OUR UNDERSTANDING OF THE HEMATOPOIETIC STEM CELL NICHE

by

JAMES GREGORY PEYER

DISSERTATION

Presented to the Faculty of the Graduate School of Biomedical Sciences

The University of Texas Southwestern Medical Center at Dallas

In Partial Fulfillment of the Requirements

For the Degree of

DOCTOR OF PHILOSOPHY

The University of Texas Southwestern Medical Center at Dallas

Dallas, Texas

December, 2015

REFINING OUR UNDERSTANDING OF THE
HEMATOPOIETIC STEM CELL NICHE

Publication No._____

James Gregory Peyer, Ph.D.

The University of Texas Southwestern Medical Center at Dallas, 2015

Supervising Professor: Sean J. Morrison, Ph.D.

A major therapeutic goal of studying blood-forming hematopoietic stem cells (HSCs) is to understand the mechanisms by which HSCs are maintained in the bone marrow, so that they can be grown outside of the body and used in lieu of or in combination with bone marrow transplantation to treat hematopoietic illnesses. HSCs, as well as other somatic stem cells from different organ systems and organisms, rely on signals from their local microenvironment for their maintenance. However, the identity of the HSC niche is still poorly understood. One new model of the HSC niche is that HSCs, periarteriolar stromal cells, and nerve fibers are closely associated in rare periateriolar niches. Using a novel marker to identify HSCs in three-dimensional confocal images, α*-catulin*-GFP, we measured the distances from thousands of HSCs to various landmarks in the bone marrow. We found that few HSCs are closely associated with either nerve fibers or arterioles. Mice lacking sympathetic nerves exhibit multiple changes in hematopoiesis, especially in response to injury, though all of the studies published so far have systemically ablated sympathetic nerves. This left unresolved the question of whether the changes in hematopoiesis reflect bone marrow denervation itself, or systemic effects of general sympathectomy. To test this, I developed a model for bone marrow-specific neuropathy by conditionally deleting nerve growth factor (Ngf) from bone marrow stromal cells. Using this model, I analyzed the role of bone marrow peripheral nerves in hematopoiesis. I demonstrated that while nerves play no role in bone marrow homeostasis, nerve signaling after bone marrow injury is essential for hematopoietic regeneration. Future studies will build on this work to understand how

nerve fibers promote the regeneration of HSCs and bone marrow cells despite not innervating the HSC niche themselves.

TABLE OF CONTENTS

PRIOR PUBLICATIONS

Zhou, Bo O., Rui Yue, Malea M. Murphy, **James G. Peyer**, and Sean J. Morrison. 2014. “Leptin-Receptor-Expressing Mesenchymal Stromal Cells Represent the Main Source of Bone Formed by Adult Bone Marrow.” *Cell Stem Cell* 15 (2) (August 7): 154–68.

Açar, Melih, Kiranmai S. Kocherlakota*, Malea M. Murphy*, **James G. Peyer***, Hideyuki Oguro, Christopher N. Inra, Christabel Jaiyeola, Zhiyu Zhao, Katherine Luby-Phelps, and Sean J. Morrison. 2015. “Deep Imaging of Bone Marrow Shows Non-Dividing Stem Cells Are Perisinusoidal.” *Nature,* In press.
(*, equal contributions from these authors)

CHAPTER ONE
A history of the hematopoietic stem cell and its niche

1.1 Introduction

Nearly twenty thousand hematopoietic stem cell (HSC) transplants are performed in the United States each year to treat genetic diseases, anemias, and malignancies of the blood (C.W. Bill Young Cell Transplantation Program, 2015). Despite the high volume of transplants being performed, many patients remain without a matched bone marrow donor, and the success rate of transplants is only about 75% (Mayo Clinic, 2015). Further study of the HSC and the mechanism by which it is maintained in the bone marrow holds the promise of improving the safety and efficacy of bone marrow transplants (Bowman and Zon, 2009). In addition to the medical payoffs of studying mechanisms of stem cell maintenance, understanding how the blood maintains homeostasis while generating billions of new cells every day is a question of incredible scientific interest. Furthermore, the cell-intrinsic and cell-extrinsic mechanisms used to maintain stem cells are often co-opted by cancer cells, so understanding these mechanisms may create new avenues to combat cancer. In this chapter, I will present a brief history of bone marrow transplantation and the challenges that the practice currently faces; then I will discuss the cell-extrinsic maintenance of HSCs.

1.2 A brief history of early organ transplantation

The oldest reliable records of organ transplantation date back to the sixth century BCE, when the Indian surgeon Sushruta performed a nose reconstruction with skin grafted from a patient's own forehead (Shiffman and Di Giuseppe, 2013). However, the modern history of transplantation medicine begins in the sixteenth century, when Gasparo Tagliacozzi recorded his efforts to perform both skin autografts, from a patient's own body, and allografts from an unrelated donor (Micali, 1993; Tagliacozzi, 1597). Tagliacozzi never succeeded in performing an allograft, due to what he surmised was the "force and power of individuality." This observation from 1597 represents the first recorded evidence of immune rejection.

The practice of transplantation was formalized in the modern sense by the Swiss surgeon Theodor Kocher, who performed the first thyroid transplant after perfecting the surgical procedure for removing the thyroid (Morris and Schirmer, 1990). Shortly afterwards, the brilliant surgeon and scientist Alexis Carrel was the first to scientifically pose the problem of transplant rejection while doing experiments in dogs as he was developing his method of arterial grafts (Morris and Schirmer, 1990). These two pioneers were the recipients of some of the first Nobel Prizes for their work: Kocher in 1909 and Carrel in 1912.

Building on Carrel's notes about transplant rejection, Peter Medawar, a research fellow at Oxford, performed the foundational work to understand why allografts were rejected. After years of characterizing the infiltration of hematopoietic cells into rejected rabbit allografts (Gibson and Medawar, 1943; Medawar, 1944), he successfully transplanted skin between dizygotic twin cattle, even while transplants

from an unrelated donor were rejected (Billingham et al., 1953). Afterwards, Medawar became aware that Ray Owen had previously found circulating red blood cells of an adult cow with genetic markers from its fraternal twin (due to a shared placental blood supply quite rare among mammals) (Owen, 1945). Medawar's results indicated that transplantation early in life creates a permissive environment for engraftment. For his observations, he was awarded a Nobel Prize in 1960, and the fields of hematopoietic biology and organ transplantation became inextricably linked.

1.3 Development of bone marrow transplantation

Interest in immune cells during transplantation was accelerated by concerns about radiation in the atomic age. As radiation technology entered common use in the laboratory in the late 1950s, it was rather quickly discovered that mice could be saved from radiation-induced lethality by shielding the spleen with lead (Jacobson et al., 1949) or by giving them a transplant of bone marrow cells (BMT) (Lorenz et al., 1951). Interestingly, both of these studies mistakenly attributed the rescue to humoral instead of cellular factors. However, this was rectified when it was shown that tolerance to skin transplants, such as those Medawar and colleagues had performed, could be induced by performing irradiation and bone marrow transplantation (Main and Prehn, 1955). Furthermore, the use of cytogenic techniques showed decisively that the hematopoietic cells of mice that had received bone marrow transplants were of donor origin (Ford et al., 1956).

These observations made the leap to the clinic rapidly, when E. Donnall Thomas and colleagues attempted to use irradiation, chemotherapy, and bone marrow transplants to treat patients with acute leukemia, a disease that was at the time almost universally lethal (Thomas et al., 1957). Although early experiments in humans to treat leukemia were unsuccessful, Thomas's group had some glimmers of success, such as a benign recovery in a leukemia patient given a transplant from their identical twin before the disease relapsed (Thomas et al., 1959). During this period, the incredible challenges facing marrow transplantation were laid out, including immunosuppression, donor matching, and the possibility of Graft Versus Host Disease (GVHD) (Mathe et al., 1963; Thomas et al., 1962, 1975). However, Thomas's conviction about the necessity of BMT as a medical tool was apparent from his very first writings:

"In an atomic age, with reactor accidents not to mention stupidities with bombs, somebody is going to get more radiation than is good for him. If infusion of marrow can induce recovery in a mouse or monkey after lethal radiation, one had best be prepared with this form of treatment in man. The leukemic patient who needs radiation and bone marrow and the uremic patient who needs a spare kidney are people who deserve immediate consideration. From helping them one will be preparing for the atomic disaster of tomorrow and it is high time one did." (Thomas et al., 1957).

It was not until a decade after the first attempts at BMT that Robert Good, working at the University of Minnesota in 1968, performed the first wholly successful

bone marrow transplant to treat an X-linked genetic immunodeficiency syndrome in a newborn child who would have otherwise died (Gatti et al., 1968).

The creation of tests for matching histocompatibility loci and the development of the immunosuppressive drug Cyclosporine A to help mitigate the response of transplant rejection and GVHD (Powles et al., 1978) established BMT as the most powerful tool for treating inherited defects of the blood, as well as leukemia.

1.4 History and challenges of early gene therapy

Good's success was the first example of using BMT to repair a genetic defect. However, with all the complications associated with BMT, not to mention the difficulty of finding an appropriately matched donor, the treatment options for most patients were still quite limited. In theory, the best way to correct faulty genes would be to modify the patient's own cells, thereby circumventing the complications of donor matching and potential GVHD. Stanfield Roger, writing in a 1970 edition of *New Scientist* magazine, first suggested using exogenous DNA to correct inborn genetic defects, a notion shortly thereafter championed by Ted Friedmann (Friedmann and Roblin, 1972), who performed much of the early work that laid a foundation for cell modification technologies (Friedmann, 1989; Gruber et al., 1985).

The concept of gene therapy is predicated on the ability to accurately manipulate DNA. In the early 1970s biochemist Paul Berg had succeeded in creating a hybrid DNA vector of the cancer-causing virus SV40 and the bacteriophage *Lambda* (Jackson et al., 1972). In response to a call from other investigators to halt

the experiments, Berg never inserted the hybrid virus into *E. coli* bacteria, for fear that the cancer-causing SV40 DNA could end up in the intestinal tract of humans who came into contact with the infected bacteria (Carmen, 1985). This concern caused Berg and others to enact a voluntary moratorium on recombinant DNA experiments. Inserting healthy human genes into viruses with the intention to infect diseased human cells, as advocated by Friedmann in 1972, carried with it a series of scientific questions. (1) Could DNA actually be designed and inserted into human cells? (2) Would inserted DNA have other effects besides repairing the damaged gene? And (3) How could we verify that the cells being targeted by the therapy were successfully modified? Although the answers to these questions were not immediately apparent, Berg organized the Asilomar Conference on Recombinant DNA in 1975 to lift the moratorium on experiments involving recombinant DNA. The attendees, including biologists, physicians, and lawyers, drew up voluntary guidelines which established a consensus for how recombinant DNA research would continue (Carmen, 1985). The power and potential of gene therapy captured the attentions of the public and eminent researchers alike, but it took fifteen years to develop the technology to a sufficient stage to begin the first human gene therapy trials.

The first attempts at gene therapy were performed in isolated T cells of patients with genetic immunodeficiency in 1990, but relief of the immunodeficiency symptoms was transient due to the fact that isolated T cells and not blood stem cells were genetically corrected (Blaese et al., 1995). Shortly afterwards, a new genetic

immunodeficiency trial was initiated using whole bone marrow as the target for gene therapy (Cavazzana-Calvo et al., 2000). Unfortunately, three out of the twenty patients in this trial developed leukemia as a result of the therapy, one of whom died as a result of their disease (Hacein-Bey-Abina et al. 2003; Woods et al. 2006; Thrasher et al. 2006). The fear of what Sheryl Gay Stolberg of the New York Times termed a “Biotech Death” induced a crackdown by the Food and Drug Administration and the National Institutes of Health on the practice of gene therapy (Stolberg, 1999).

The leukemias developed by these three patients had insertional mutagenesis of proto-oncogenes, which predisposed them to cancer development (Hacein-Bey-Abina et al. 2003; Woods et al. 2006; Thrasher et al. 2006). Modern gene therapy trials have avoided this pitfall by using viral vectors that integrate into the genome at predictable, indolent sites (Naldini, 2009; Ronen et al., 2011; Tubsuwan et al., 2013). Thanks to these vectors, recent gene therapy trials have succeeded with no reports of oncogenesis in patients (Cartier et al., 2009; Herzog et al., 2010; Takefman and Bryan, 2012).

1.5 Challenges facing gene therapy for hematopoietic cells

HSCs persist after a bone marrow transplantation and produce the full spectrum of red and white blood cells; they are the active cells that determine the genetic makeup of a transplant recipient’s new blood supply (Morrison et al., 1995). Hematopoietic stem cells used for transplantation can come from bone marrow,

mobilized peripheral blood, or umbilical cord blood. Bone marrow and mobilized peripheral blood donation is uncommon, and between twenty-five and eighty-five percent of patients (depending on the individual patient's genetic background) in need of a transplant are unlikely to find an HLA-matched donor (Gragert et al., 2014). Cord blood is more readily available and does not require the donor and recipient to have perfectly matched HLA loci (Norkin et al., 2012), but a single umbilical cord does not contain enough HSCs to fully reconstitute a patient (Barker et al., 2005; Norkin et al., 2012). To circumvent this issue, two cords are often combined and infused into a recipient, but this practice leads to a number of complications (Barker et al., 2005). Expanding HSCs *ex vivo* from either bone marrow or cord blood, and thereby enabling HSCs from a single donor to reconstitute multiple matched recipients, is a major clinical goal of HSC research (Norkin et al., 2012; Walasek et al., 2012).

Although we are able to isolate HSCs with exceptionally high purity in both mice and humans (Kiel et al., 2005; Notta et al., 2011), maintaining and expanding HSCs outside of the body for clinical use has remained challenging despite promising efforts (Boitano et al., 2010; Fares et al., 2014; Norkin et al., 2012; Walasek et al., 2012). HSCs exhibit incredible self-renewal potential *in vivo* (Pawliuk et al., 1996), so in order to reach the goal of growing HSCs *ex vivo*, a promising approach is to understand and then recreate key aspects of the HSC's microenvironment in the bone marrow, the stem cell niche. However, it remains a topic of disagreement among different groups which cells make up the HSC niche.

1.6 Early evidence for a hematopoietic stem cell niche

HSCs make up only a tiny fraction of all bone marrow cells—fewer than 1 in 20,000 (Kiel et al., 2005; Ng et al., 2009). However, only these cells give rise to all the various lineages of hematopoietic cells (Ng et al., 2009). Ernest McColloch and James Till performed the first definitive experiments showing that the hematopoietic system had a single common precursor by investigating the cell types in clonogenic colonies within the spleens of irradiated mice (Till and McCulloch, 1961). Furthermore, these spleen colonies (Spleen Colony Forming Units, or CFU-S) could be transplanted into new recipient mice and give rise to more spleen colonies, indicating that these cells had the potential to self-renew (Siminovitch et al., 1963). However, these cells could not self-renew indefinitely, as subsequent transplantations frequently failed to yield new CFU-S (Schofield, 1978). Another model of transplantation used at the time was the W/W^v mouse. This mouse, which carried a spontaneous mutation in the c-kit gene, would accept a bone marrow transplant without prior conditioning by irradiation (Sharkis et al., 1978). Of interest, wild-type donor cells could survive and proliferate in the bone marrow of W/W^v mice throughout the lifetime of the recipient.

In 1978, Ray Schofield was struggling with this apparent contradiction between these two models of HSCs. The CFU-S would form a colony and then fail to self-renew upon serial transplantation, but the W/W^v mice would host donor cells in their bone marrow for a seemingly unlimited time. It was not until much later that it

became apparent that most CFU-S are not HSCs (Ploemacher et al., 1989). So in Schofield's mind, the question was simple: why do CFU-S lose self-renewal capacity while HSCs transplanted into W/W^v mice retain it? From these fragments of data, combined with evidence from Dexter and colleagues, who were able to grow hematopoietic progenitors on feeder layers of bone marrow stroma (Dexter et al., 1977), Schofield hypothesized the existence of a niche for HSCs. He suggested that this niche would have five characteristics: 1) It would be a defined anatomic site, 2) stem cells would be maintained and proliferate there, 3) differentiation would be inhibited in the niche, 4) it would have limited space so that the number of stem cells would be limited, and 5) slightly more mature cells would revert to a stem-cell phenotype if they could take up residence in an unoccupied niche (Schofield, 1978).

Although many aspects of Schofield's niche were a far stretch from the available data, his hypothesis showed incredible creativity and prescience. However, it would be two decades before the existence of a stem cell niche would be demonstrated in any tissue; it would not be in mice or men, but in the ovaries of the fruit fly *Drosophila melanogaster.*

1.7 Evidence for niches in *Drosophila melanogaster*

Stem cells were first identified in the *Drosophila* ovary in 1966, when Ann Chandley used thymidine labeling to show clonogenicity of rare cells at the anterior region of each ovariole (Chandley, 1966). This observation was echoed in other descriptive studies (Carpenter, 1975; Koch and King, 1966) and later by more

rigorous clonal analysis (Schupbach et al., 1978; Wieschaus and Szabad, 1979). However, it was not until Haifan Lin and Allan Spradling developed a transplantation model for Drosophila ovaries, then deleted the ovary stem cells by laser ablation, that the identity of ovary stem cells was demonstrated functionally (Lin and Spradling, 1993). Then in 1998, Xie and Spradling reported the first molecular evidence for a stem cell niche, showing that BMP homolog *dpp* was required to maintain germline stem cells in the ovary (Xie and Spradling, 1998), and subsequently identified the cap cells as the key niche component for the germ line stem cells (Xie and Spradling, 2000).

The germline stem cell is not the only progenitor within the ovary. Developing germline cysts are surrounded by a layer of follicle cells, which are produced by a pair of follicle stem cells (FSCs) on opposite sides of the germarium, posterior to the germline stem cells (Margolis and Spradling, 1995). These FSCs are regulated by *wingless* and *DE-cadherin*, which regulate signaling of the *Drosophila* equivalent of the β-catenin pathway in mammals (Song and Xie, 2002, 2003).

To this point, powerful genetic tools to address the function of different cell types were limited to *Drosophila* and *C. elegans*. However, in the early 2000s, mouse genetics tools were becoming much more powerful with the maturation of *cre*-recombinase mediated deletion technologies (Rossant and McMahon, 1999) combined with the publication of the mouse genome sequence (Chinwalla et al., 2002). Equipped with these new tools, multiple groups wanted to test whether Schofield's hypotheses held up as well in the system he was originally describing,

the HSC niche in the bone marrow, as they did in the *Drosophila* germline. Would BMP or β-catenin signaling be critical for HSC maintenance, as they were for different populations of ovary stem cells? And more broadly, which types of cells created the niches for HSCs in the bone marrow? To better approach this second question, we should first discuss the different types of non-hematopoietic cells that make up the bone marrow microenvironment.

1.8 The development and anatomy of murine bone marrow

The marrow cavity in long bones is created during fetal development shortly before birth in mice, around day E15.5, during which a mass of cartilage rapidly undergoes endochondrial ossification and vascularization, starting from the center and spreading towards the ends of the bone (Gilbert, 2000). Hematopoiesis begins in the marrow at day E18.5, after vascularization is complete, and continues in the marrow for the remainder of the mouse's life. The bone marrow cavity consists of the diaphysis, the volume within the long shaft of the cortical bone, and the wider metaphysis and epiphysis that occupy the wide head of the bone. The metaphysis and the epiphysis are separated by the growth plate, and both have trabecular bone within their marrow. Both the cortical and trabecular bone are lined with bone-forming osteoblasts and punctuated by occasional bone-resorbing osteoclasts (Morrison and Scadden 2014).

Blood flows into the bone marrow primarily within the nutrient artery, which enters the diaphysis through a passage created during ossification called the

foramen that tunnels through the cortical bone. This large artery quickly branches in the central marrow into a series of small arterioles covered with smooth muscle cells, pericytes, nerve fibers, and glia (Calvo and Forteza-Vila, 1969; Yamazaki and Allen, 1990). These arterioles run longitudinally through the marrow towards the metaphases, branching at various times towards the endosteum, where they narrow, lose their smooth muscle sheathes, and supply a complex network of thin capillaries near the bone surface in a region termed the “transition zone” (Li et al., 2009). These capillaries connect to large diameter sinusoidal vessels, which run centripetally away from the bone surface towards a large central sinus parallel to the bone. The central sinus is drained by the nutrient vein, which exits the marrow through the foramen. Of these categories of blood vessels, sinusoids are by far the most abundant type of vessel in the bone marrow (Morrison and Scadden 2014).

Arterioles, capillaries, and sinusoids are all surrounded by perivascular stromal cells on their abluminal surfaces (Calvo and Forteza-Vila, 1969; Yamazaki and Allen, 1990). Similar stromal cells are also found stretching between vessels in addition to wrapping around them, forming a continuous lattice of reticular processes that spans the entire marrow cavity (Açar et al., 2015).

1.9 Cell types purported to create a niche for HSCs

1.9.1 The osteoblast niche hypothesis

Before Schofield had even hypothesized the existence of a hematopoietic niche, early experiments suggested that not all regions of the bone marrow were

created equal. Lord and Hendry reported that the frequency of CFU-S was higher closer to the femoral endosteum than in the middle of the marrow, (Lord and Hendry, 1972) and that CFU-S in that region were more highly proliferative (Lord et al., 1975). The notion that HSCs reside in close proximity to the endosteum started with these observations. Before investigations of the mammalian niche were started in earnest, credence to the notion of an osteoblastic niche was bolstered by Taichman and Emerson (Taichman and Emerson, 1994), who grew hematopoietic progenitors on a feeder layer of osteoblasts. They showed that osteoblasts expressed the myeloid growth factor GCSF and grew hematopoietic progenitors for up to two weeks—much shorter than experiments done by Michael Dexter in 1977, who used a general preparation of bone marrow mesenchymal cells (Dexter et al., 1977).

These studies, combined with the recent elucidation of the *Drosophila* germ cell niche, set the stage for studying the HSC niche using genetic tools. This was first done in the laboratories of Linheng Li and David Scadden in the early 2000's (Calvi et al., 2003; Zhang et al., 2003). Li's group followed the lead of *Drosophila* researchers and deleted the receptor for BMP from hematopoietic and stromal cells in the bone marrow. They reported an increase in bone density and ectopic bone growth concomitant with an increase in the frequency and number of HSCs. Scadden's group analyzed a mouse in which osteoblasts were engineered to overexpress an active form of the parathyroid hormone receptor. They too reported an expansion of both osteoblasts and HSCs. These observations were widely

interpreted to mean that osteoblasts create the niche for HSCs, although these studies did not directly test this.

The notion that HSC and osteoblasts numbers would always be correlated has not survived subsequent experimentation. Depletion of osteoblasts using multiple model systems depleted lymphoid and myeloid cells long before HSCs were affected (Kiel et al., 2007a; Visnjic et al., 2004; Zhu et al., 2007), and increased numbers of osteoblasts did not always increase HSC numbers either (Lymperi et al., 2008).

A major appeal of the osteoblastic niche for HSCs was the suggestion that osteoblasts and HSCs both expressed N-cadherin, and that N-cadherin acting through β-catenin promoted HSC maintenance (Reiss et al., 2005; Sugimura et al., 2012; Wilson and Trumpp, 2006). This hypothesis was closely analogous to studies from *Drosophila* follicle stem cells, which depend on DE-cadherin-mediated activation of β-catenin for their maintenance (Song and Xie, 2002). While it is intellectually appealing that the stem cell niche would function very similarly in both systems, claims about the role of N-cadherin in the HSC niche have failed to hold up to further testing. In fact, HSCs do not actually express N-cadherin (Kiel et al., 2007a; Morita et al., 2010), N-cadherin is not required for HSC function (Foudi et al., 2009; Kiel et al., 2007b; Li and Zon, 2010), and the HSC markers used by Zhang et al. yield a very low purity of HSCs (Kiel et al., 2009).

Another study localized HSCs in three dimensional confocal images (Kunisaki et al., 2013) and came to the conclusion that most HSCs were located near the

endosteum. However, the authors arrived at this conclusion by counting the number of HSCs in concentric cylinders that each accounted for 10% of the marrow radius, so that the outermost cylinders contained a much greater volume than the innermost cylinders (Kunisaki et al., 2013). Reanalysis of both their data and additional data after correcting the analysis to separate HSCs into cylinders of equal volumes suggested that HSCs are located in the central marrow, away from the endosteum (Açar et al., 2015).

In summary, the evidence does not support the conclusion that HSCs reside in an osteoblastic niche. However, multiple groups have shown that some more differentiated hematopoietic progenitors are regulated by osteoblasts, especially lymphoid progenitors, suggesting that there may be an osteoblastic niche for certain kinds of restricted progenitors (Ding and Morrison, 2013; Lymperi et al., 2008; Visnjic et al., 2004; Zhu et al., 2007).

1.9.2 The perivascular niche hypothesis

Early imaging studies of HSCs pointed to an endosteal niche, but substantial evidence also suggested a role for vasculature in regulating hematopoiesis. Shahin Rafii's work throughout the 1990s demonstrated that hematopoietic progenitors could be grown upon feeder layers of endothelial cells (Rafii et al., 1994, 1995, 1997). Rafii had also characterized the role of endothelial cells in promoting the maturation of megakaryocytes and the production of platelets (Avecilla et al., 2004), a process dependent upon the cytokines thrombopoietin and CXCL12, which act on

immature hematopoietic cells (Ara et al., 2003; Sugiyama et al., 2006a; Zou et al., 1998). Furthermore, HSCs can extravasate into the blood and mobilize to other tissues through the sinusoidal endothelium within minutes of receiving a mobilization signal (Fukuda et al., 2007; Pelus and Fukuda, 2008), indicating that at least some HSCs likely reside in close proximity to sinusoids.

Before 2005, imaging studies of HSC localization used BrdU retention (Zhang et al., 2003) or c-Kit staining (Calvi et al., 2003) to identify HSCs. These markers yield a very low purity of HSCs, such that fewer than one in twenty cells identified in sections were likely to actually be HSCs (Kiel et al., 2005, 2007b). In 2005, Sean Morrison's laboratory introduced the SLAM markers for HSCs, which improved the purity of stem cells to 1 in 2.5 or better (Kiel et al., 2005). With this tool, they performed the first imaging studies of HSCs with markers that give a very high purity. They found that fewer than fifteen percent of HSCs localized near the endosteum, and the vast majority of HSCs resided close to sinusoidal blood vessels (Kiel et al., 2005).

Shortly afterwards, Sugiyama and colleagues discovered that CXCL12 in the bone marrow is produced primarily by perivascular stromal cells (Sugiyama et al., 2006a) long known to exist (Yamazaki and Allen, 1990) but previously without a marker to identify them. Ding and Morrison went on to functionally demonstrate that these cells, along with endothelial cells, are the critical sources of CXCL12 and SCF in the bone marrow (Ding and Morrison, 2013; Ding et al., 2012). A follow-up study showed that conditionally deleting SCF from both endothelial cells and leptin

receptor (LepR) expressing stromal cells depletes all quiescent and serially transplantable HSCs (Oguro et al., 2013). These results prove that HSC maintenance depends on a perivascular niche.

This concept, however, challenged some parts of Schofield's 1978 hypothesis which had held up so well in studies of the fly ovary and testes. Both endothelial cells and perivascular stromal cells are very common in the bone marrow, with nearly 90% of the marrow volume within 10μm of a perivascular cell, and 85% of marrow volume within 10μm of a blood vessel (Açar et al. 2015, unpublished data). It remains possible that Schofield's hypothesis was correct, and that the HSCs are restricted in their localization to a subset of endothelial or perivascular cells that define a rare niche. However, this would require the identification of new markers that label only subsets of perivascular stromal or endothelial cells and for HSCs to preferentially localize in close proximity to those cells.

1.9.3 The neuro-arteriolar niche hypothesis

Paul Frenette's group had previously worked on the regulation of hematopoiesis by the sympathetic nervous system (Katayama et al., 2006; Méndez-Ferrer et al., 2008, 2010a). They demonstrated that mobilization of HSCs into the blood is influenced by signals from sympathetic nerves. Nerves primarily innervate stromal cells around arteries and arterioles, where they regulate blood flow by contracting or relaxing the smooth muscle sheathes surrounding the blood vessel

(Gilbert, 2000). Thus, the endothelial and perivascular cells near the nerves and arterioles seemed an intuitively promising site for the HSC niche.

Frenette's group identified cells in the bone marrow based upon their expression of a transgenic reporter using the promoter of the intermediate filament protein Nestin (Méndez-Ferrer et al., 2010b). The authors drew parallels to the *Drosophila* germline, where germline stem cells reside in close proximity to cyst progenitor cells (male) (Yamashita et al., 2005) or escort stem cells (female) (Decotto and Spradling, 2005). They claimed that HSCs reside adjacent to rare *Nestin*-GFP-expressing cells and that *Nestin*-GFP cells are mesenchymal stem cells (MSCs), capable of producing osteoid, chondrocyte, and adipocyte progeny. Unfortunately, the claim that HSCs and rare arteriolar *Nestin*-expressing cells form a unique niche, a pairing in line with Schofield's original predictions in 1978, is not supported by data.

There are at least two populations of cells marked by the *Nestin*-GFP transgene, a very rare population that runs along the arterioles and expresses high levels of the transgene (*Nestin*^{bright} cells), along with a much more common population of perivascular stromal cells present throughout the marrow. This second population overlaps strongly with the LepR^{+} cells that are functionally important in the perivascular HSC niche (Ding et al., 2012; Oguro et al., 2013; Zhou et al., 2014). The abundant LepR^{+} population contains over 90% of CFU-F in the bone marrow, a surrogate marker of MSCs, while the *Nestin*^{bright} population contains less than 10% of all CFU-F (Zhou et al., 2014). LepR^{+} cells are abundant throughout the marrow

(Açar et al., 2015; Zhou et al., 2014), and roughly one in six LepR^{+} cells has CFU-F activity (Zhou et al., 2014). Therefore, *Nestin*^{bright} cells are not the only MSCs in the bone marrow.

HSCs are approximately twice as likely to be within twenty microns of a perivascular cell compared to a *Nestin*^{bright} cell, with 70% of all HSCs found localizing farther than twenty microns from a *Nestin*^{bright} cell. The vast majority of HSCs are in close proximity to LepR^{+} perisinusoidal stromal cells (Açar et al., 2015; Kunisaki et al., 2013). Thus, *Nestin*^{bright} cells and HSCs are not frequently associated with each other. These data dispel the notion that HSCs can only exist in rare niches created by *Nestin*^{bright} cells, although they do support the idea that MSCs play a role in the HSC niche, since LepR^{+} cells are MSCs (Zhou et al., 2014) and associate with nearly all HSCs (Açar et al., 2015). However, because LepR^{+} cells are abundant throughout the marrow, the vast majority cells contacting LepR^{+} cells are not HSCs.

Despite the low frequency of association between HSCs and arteriolar *Nestin*^{bright} cells, Frenette's group claimed that *Nestin*^{bright} cells were crucial to HSC maintenance by selectively eliminating *Nestin*-expressing cells using *Nestin*-CreER or *NG2*-CreER paired with an inducible diphtheria toxin receptor. They observed a slight depletion of HSCs in the marrow after administration of diphtheria toxin, but the deletion of any cell population from the bone marrow leads to a modest reduction in HSCs, even when the deleted cells are not a significant source of HSC maintenance factors (Visnjic et al., 2004; Zhu et al., 2007), suggesting that this response may be a non-specific consequence of tissue damage. *Nestin*-CreER and

NG2-CreER-expressing cells do not detectably express *Scf* or *Cxcl12* (Kunisaki et al., 2013; Méndez-Ferrer et al., 2010b), and when the critical niche factors *Cxcl12* and *Scf* were deleted from *Nestin*-CreER or *NG2*-CreER-expressing cells, HSCs were not affected (Açar et al., 2015; Ding and Morrison, 2013; Ding et al., 2012).

Another group led by Hiromitsu Nakauchi presented data suggesting that HSCs reside in close proximity to bone marrow nonmyelinating Schwann cells, which surround nerve fibers in the marrow (Yamazaki et al., 2011). Similar to the *Nestin*^{bright} cells, only a minority of Schwann cells are closely associated with HSCs (Açar et al., 2015; Yamazaki et al., 2011). However, the authors presented compelling evidence that the activation of latent TGF- β signaling maintains stem cell quiescence. But because few HSCs localize close to Schwann cells, it remains unclear whether stem cell quiescence is directly maintained through the diffusion of active TGF-β from distant Schwann cells or TGF-β receptor indirectly regulates HSCs.

A unique cell type that creates a specialized niche for HSCs may exist, as in the *Drosophila* germline. However, there is no evidence for such a cell based on current data. While Schofield's hypotheses, if true, would have significant implications for understanding the biology of hematopoiesis as well as improving transplantation therapy, much of the past fifteen years has been spent fitting the data to the hypothesis, as opposed to rigorously testing hypotheses based on the data. A huge number of variables that are just beginning to be investigated could define specific stem cell niches in the bone marrow, including oxygen tension, shear

forces, extracellular matrix structures, secreted factors, and markers that allow for the detection of rare subpopulations of perivascular or endothelial cells uniquely suited to maintain HSCs (reviewed in Wang and Wagers, 2011). As a null hypothesis, however, future studies must always evaluate their data against the possibility that the entire central bone marrow serves as a niche for HSCs—that long-range signals such as TGF-β or abundant signals such as SCF and CXCL12 regulate both stem cells and differentiated cells. In this model, the intrinsic differences between the stem cells and other cells are what determine their behavior in response to these signals—not a difference in their localization within the bone marrow. Future studies of the HSC niche and regulation of HSC function will have to distinguish between these two possibilities.

1.10 Evidence for neural regulation of hematopoiesis and marrow regeneration

There are substantial data suggesting that various aspects of hematopoiesis are regulated by the sympathetic nervous system (SNS). Afan and colleagues were the first to report that marrow cellularity and CFU-C decrease in the marrow after surgical or chemical sympathectomy (Afan et al., 1997). However, attempts to repeat these experiments have given variable results, with some groups reporting the same decrease in marrow cellularity and CFU-C (Yamazaki et al., 2011) and others seeing no effect on steady state hematopoiesis after sympathectomy (Katayama et al., 2006; Lucas et al., 2013).

The SNS has also been reported to play a role in regulating the mobilization of hematopoietic cells into the blood, either during natural circadian oscillations (Lucas et al., 2008; Méndez-Ferrer et al., 2008) or upon administration of a chemical agent designed to mobilize progenitors (Katayama et al., 2006; Lucas et al., 2013; Méndez-Ferrer et al., 2008). Sympathectomized mice and humans fail to mobilize hematopoietic progenitors into their blood during circadian cycles or upon chemical mobilization (Lucas et al., 2008; Méndez-Ferrer et al., 2008). The physiological importance of this HSC mobilization is not clear, however, since mice with disrupted circadian rhythms do not develop any hematopoietic complications.

While the data suggest that the SNS does not play a critical role in steady state hematopoiesis, one recent study found that nerves may play a critical role during regeneration of the bone marrow after injury (Lucas et al., 2013). In this study, the authors used the chemotherapeutic agent cisplatin or a dopamine analog, 6-hydroxydopamine (6OHDA) to chemically sympathectomize mice and then performed bone marrow transplants. To their surprise, sympathectomized mice did not recover hematopoiesis after BMT as well as control mice. They repeated these observations with another model of SNS depletion, activation of diphtheria toxin receptor on peripheral nerves using Tyrosine hydroxylase-Cre (*TH*-Cre) paired with an inducible diphtheria toxin receptor, and saw the same effect of nerve loss. The authors went further to demonstrate that the impaired recovery was due to the nerves themselves, as mice with p53-deficient nerves and mice treated with the

neuroprotective drug 4-methylcatechol were resistant to nerve depletion caused by cisplatin treatment and recovered normally from hematopoietic injury.

While striking, the mechanism governing this impairment of regeneration in the context of nerve loss is not clear. The authors observed a modest (roughly twofold) reduction in the number of *Nestin*-GFP-expressing cells and endothelial cells one month after bone marrow transplantation. (It is not clear from their text whether the authors analyzed *Nestin*^{bright} arteriolar or *Nestin*^{dim} perivascular cells, but based upon the frequency of the reported cells I believe they must have quantified *Nestin*^{dim} cells, although all of their images show only *Nestin*^{bright} cells). They also evaluated the cell cycle status of these cells either under steady state or after three days of treatment with chemical antagonists to β2- and β3-adrenergic receptors, which are required for marrow cells to internalize norepinephrine signals from peripheral nerves (Méndez-Ferrer et al., 2008). They reported that the frequencies of both *Nestin*-expressing and endothelial cells in cell cycle by Ki-67 staining increased after adrenergic receptor blockade. From these experiments the authors concluded that nerves are required to maintain quiescence of perivascular and endothelial cells, so after nerve loss these cells are more susceptible to genotoxic stress such as that from irradiation. Thus, since more of these cells are destroyed during irradiation, fewer are left to repair the marrow, leading to the failure of hematopoietic recovery.

Both their data and conclusions conflict with earlier observations concerning the mechanism by which the SNS regulates the bone marrow. Firstly, the authors'

data which showed an increase in perivascular and endothelial cell cycling after adrenergic receptor blockade suggested that ~55% and ~50% of these cells, respectively, are in cell cycle (Ki-67+) in the steady state. This observation is at odds with other data suggesting that both perivascular and endothelial cells are highly quiescent (Li et al., 2008; Zhou et al., 2014). Despite being highly quiescent, the vast majority of marrow endothelial cells are destroyed following irradiation, suggesting that cell cycle status has no bearing on the sensitivity of these cells to irradiation (Hooper et al., 2009; Li et al., 2008). The authors did not perform BrdU incorporation experiments to test whether these cell populations are truly driven to proliferate after adrenergic blockade, nor did they attempt to quantify levels of apoptosis in these cell populations after genotoxic insult.

Despite these shortcomings, Lucas and colleagues discovered a context in which the nerves do affect hematopoiesis. Nerve signaling during injury may be important in therapeutic contexts, as two recent reports have suggested that the presence of nerves slows the progression of myeloproliferative neoplasms (MPNs) or acute myeloid leukemia (AML) (Arranz et al., 2014; Hanoun et al., 2014).

1.11 Statement of purpose

In every model of sympathetic nervous system activation or inhibition thus far studied in the context of hematopoiesis, experimental systems have used either systemic ablation of the SNS (Katayama et al., 2006; Lucas et al., 2013; Méndez-Ferrer et al., 2008) or highly invasive surgeries that may induce injury responses

(Yamazaki et al., 2011). There have been no studies that determine whether the effects of nerve loss on hematopoietic regeneration, mobilization of HSCs, or circadian release of progenitors are the result of bone marrow nerves or a consequence of the whole-body inactivation of the SNS.

I identified nerve growth factor (*Ngf)* as the only neurotrophin produced in the bone marrow microenvironment. Deletion of *Ngf* from perivascular stromal cells using *LepR-Cre* or *Prx1-Cre* led to a depletion of peripheral nerves specifically within the bone marrow. I showed that HSCs do not acutely depend on bone marrow nerves for their maintenance, the circadian mobilization of hematopoietic progenitors is dependent upon their marrow nerves, and that regeneration of the bone marrow following irradiation is dependent upon local innervation.

By clarifying the role of bone marrow nerves in hematopoiesis both in steady state and after injury, as well as identifying the cells responsible for maintaining peripheral innervation of the bone marrow, my work lays a foundation for further study of the regulation of hematopoiesis and leukemia by the SNS.

I also performed work to aid in the identification of cellular or anatomical landmarks that define HSC niches. I created computational tools to compare the distributions of cell populations in three dimensional spaces. Working as part of a team, we dispelled many of the claims made about HSC localization relative to various bone marrow landmarks.

Whether original conclusions were mostly correct, as with the SNS regulation of hematopoietic regeneration, or incorrect, as with the arteriolar niche hypothesis,

performing conclusive experiments to definitively test hypotheses is a prerequisite to move forwards in studying the hematopoietic niche.

CHAPTER TWO
Deep imaging of bone marrow shows non-dividing stem cells are perisinusoidal

The following manuscript is in press at Nature*. Melih Acar is the first author on this study, and I am a co-second author with Kiran Kocherlakota and Malea Murphy. I have included an additional discussion of my role in this research and the computational tools I generated in Appendices A and B.*

2.1 Abstract

Hematopoietic stem cells (HSCs) reside in a perivascular niche but the location remains controversial (Morrison and Scadden, 2014). HSCs are rare and few can be found in thin tissue sections (Kiel et al., 2005, 2007a) or upon live imaging (Lo Celso et al., 2009), making it difficult to comprehensively localize dividing and non-dividing HSCs. Here we describe the ability to image all HSCs in large segments of optically cleared bone marrow using deep confocal imaging and digital tissue reconstruction. We discovered that in the hematopoietic system *α-catulin* is nearly uniquely expressed by HSCs. *α-catulin*$^{GFP/+}$ was expressed by only 0.02% of bone marrow hematopoietic cells, including virtually all HSCs. One in 3.5 *α-catulin*-GFP^{+}c-kit^{+} cells gave long-term multilineage reconstitution of irradiated mice. We systematically localized thousands of *α-catulin*-GFP^{+}c-kit^{+} cells in optically cleared bone

marrow. HSCs were more common in central marrow than near bone surfaces and in the diaphysis relative to the metaphysis. Nearly all HSCs contacted Leptin Receptor^{+} and Cxcl12^{high} niche cells. Approximately 85% of HSCs were within 10μm of a sinusoidal blood vessel. The vast majority of HSCs were distant from arterioles, transition zone vessels, and bone surfaces. This was true of Ki-67^{+} dividing HSCs and Ki-67^{-} non-dividing HSCs. Dividing and non-dividing HSCs thus reside in perisinusoidal niches throughout bone marrow marked by contact with Leptin Receptor^{+}Cxcl12^{high} cells.

2.2 Introduction

Adult hematopoietic stem cells (HSCs) reside in a perivascular niche in the bone marrow in which leptin receptor^{+} (LepR^{+}) perivascular stromal cells and endothelial cells secrete factors that promote their maintenance (Ding and Morrison, 2013; Ding et al., 2012; Greenbaum et al., 2013; Kobayashi et al., 2010; Poulos et al., 2013). Nearly all of the cells that express high levels of *Scf* or *Cxcl12* in the bone marrow are LepR^{+} (Zhou et al., 2014). Conditional deletion of *Scf* from LepR^{+} cells and endothelial cells eliminates all quiescent and serially-transplantable HSCs from adult bone marrow (Oguro et al., 2013). The perivascular niche cells that we identified based on LepR expression have also been identified by others based on their expression of high levels of *Cxcl12* (Ding and Morrison, 2013; Omatsu et al., 2014; Sugiyama et al., 2006b), low levels of the *Nestin*-GFP transgene (Kunisaki et

al., 2013; Méndez-Ferrer et al., 2010b), PDGFR (Morikawa et al., 2009; Zhou et al., 2014), and *Prx-1*-Cre (Greenbaum et al., 2013).

Established elements of the HSC niche localize primarily around sinusoids in bone marrow tissue sections including HSCs (Kiel et al., 2005, 2007a; Nombela-Arrieta et al., 2013), $LepR^{+}$ stromal cells (Ding et al., 2012), *Angiopoietin-1*-expressing stromal cells (Sacchetti et al., 2007; Zhou et al., 2015), *Scf*-expressing stromal cells (Ding et al., 2012), $Cxcl12^{high}$ stromal cells (Ding and Morrison, 2013; Omatsu et al., 2010; Sugiyama et al., 2006b) and mesenchymal stem/stromal cells (Omatsu et al., 2010; Sacchetti et al., 2007; Zhou et al., 2014). Moreover, sinusoidal endothelial cells are functionally important for hematopoiesis after myeloablation (Hooper et al., 2009). HSCs have also been suggested to reside in a hypoxic niche (Parmar et al., 2007) and the most hypoxic region of the bone marrow is around sinusoids (Spencer et al., 2014). Nonetheless, some have suggested that HSC niches are concentrated near bone surfaces (Arai et al., 2004; Lo Celso et al., 2009; Nilsson et al., 2001; Zhang et al., 2003) or around arterioles close to bone surfaces (Kunisaki et al., 2013). The differences among studies arise partly from the rarity of HSCs—all of these studies are based on very small numbers of HSCs. No study has been able to comprehensively image HSCs throughout the bone marrow.

It has been speculated that dividing HSCs reside in a niche that is spatially distinct from quiescent HSCs, which have been proposed to reside near arterioles or bone surfaces (Kunisaki et al., 2013; Li and Clevers, 2010; Wilson et al., 2009).

However, dividing HSCs are even more rare than non-dividing HSCs making it difficult to find significant numbers of those cells within tissue sections.

HSC imaging throughout the bone marrow is also limited by the inability of even multiphoton microscopy to penetrate more than 150μm into bone marrow (Lo Celso et al., 2009; Malide et al., 2012; Takaku et al., 2010). Optical clearing techniques (Chung et al., 2013; Dodt et al., 2007; Hama et al., 2011; Renier et al., 2014; Susaki et al., 2014; Yang et al., 2014) have enabled deep imaging of other tissues and have been used to image hematopoietic progenitors in embryos (Yokomizo et al., 2012). However, to our knowledge these approaches have not been applied to the imaging of rare stem cells or to the digital reconstruction of bone marrow.

2.3 Results

To systematically identify HSCs throughout the bone marrow, we sought a single, highly specific HSC marker. By re-examining gene expression profiles of highly purified HSCs, multipotent hematopoietic progenitors (MPPs), and whole bone marrow (WBM) cells (Kiel et al., 2005) we found that *α-catulin* is highly restricted in its expression to HSCs. *α-catulin* encodes a protein with homology to α-catenin that has been suggested to function as a cytoskeletal linker(Janssens et al., 1999) or a modulator of the Rho guanine nucleotide exchange factor(Park et al., 2002). By quantitative real time RT-PCR (qRT-PCR) we found that *α-catulin* was expressed at 19±9.3 (mean±SD) fold higher levels in $CD150^{+}CD48^{-}Lin^{-}Sca\text{-}1^{+}c\text{-}kit^{+}$

(CD150^{+}CD48^{-}LSKs) HSCs as compared to unfractionated bone marrow cells and 3.3±0.8 fold higher levels in HSCs as compared to CD150^{-}CD48^{-}LSK MPPs.

To assess *α-catulin* expression in detail we knocked *GFP* into the first exon of *α-catulin* in frame with the start codon (Figure 1a). Although this was predicted to be a loss of function allele, both *α-catulin*$^{GFP/+}$ and *α-catulin*$^{GFP/GFP}$ mice were born and survived into adulthood with expected Mendelian frequencies (Figure 1e). Young adult *α-catulin*$^{GFP/GFP}$ mice were normal in size and body mass (Figure 1d) as well as bone density and bone volume (Figure 1f) relative to littermate controls. *α-catulin*$^{GFP/+}$ and *α-catulin*$^{GFP/GFP}$ mice exhibited normal hematopoiesis as well as normal HSC frequency, HSC cell cycle kinetics, and normal HSC function upon primary and secondary transplantation into irradiated mice (Figure 2).

Only 0.021±0.006% of WBM cells in *α-catulin*$^{GFP/+}$ mice were *α-catulin*-GFP^{+} (Figure 3a). Most of the *α-catulin*-GFP^{+} cells were c-kit^{+} (Figure 4a) and 49±8.3% of CD150^{+}CD48^{-}LSKs HSCs were *α-catulin*-GFP^{+} (Figure 4c). We did not detect *α-catulin*-GFP expression among MPPs (Figure 4c), CLPs, CMPs, GMPs, or MEPs (Figure 4d). *α-catulin*-GFP^{+}c-kit^{+} cells appeared to be highly purified HSCs as they represented only 0.007±0.003% of WBM cells and were uniformly CD150^{+} and CD48^{-} (Figure 3b and Figure 4b).

To test the function of *α-catulin*-GFP^{+} cells we performed long-term competitive reconstitution assays in irradiated mice. One in 37,000 WBM cells gave long-term multilineage reconstitution (Figure 3c). One in 6.7 *α-catulin*-GFP^{+} cells

gave long-term multilineage reconstitution (a 5500-fold enrichment over WBM; Figure 3c). In contrast, only 1 in 2,847,000 α-*catulin*-GFP$^-$ bone marrow cells gave long-term multilineage reconstitution (a 77-fold depletion over WBM; Figure 3c). The α-*catulin*-GFP$^+$ fraction of CD150$^+$CD48$^-$LSK cells gave long-term multilineage reconstitution (1 in 3.1 cells) but the α-*catulin*-GFP$^-$ fraction had little HSC activity (1 in 110 cells) (Figure 3c). Therefore, virtually all HSC activity in adult bone marrow is contained within the α-*catulin*-GFP$^+$ fraction of cells.

We further increased the purity of HSCs in the α-*catulin*-GFP$^+$ fraction by staining with an antibody against c-kit. One in 3.5 α-*catulin*-GFP$^+$c-kit$^+$ cells gave long-term multilineage reconstitution of irradiated mice (Figure 3c). α-*catulin*-GFP$^+$c-kit$^+$ cells are thus comparable in purity to the best HSC markers available. All of the primary recipient mice that were long-term multilineage reconstituted by 1 or 5 α-*catulin*-GFP$^+$c-kit$^+$ cells also gave long-term multilineage reconstitution in secondary recipient mice (Figure 5).

α-*catulin*-GFP$^+$c-kit$^+$ cells are largely quiescent, comparable to CD150$^+$CD48$^-$ LSKs HSCs, with only 1.2±0.5% of cells in S/G2/M phase of the cell cycle (Figure 6a). The α-*catulin*-GFP$^+$ fraction of CD150$^+$CD48$^-$LSK cells divided significantly less frequently than the α-*catulin*-GFP$^-$ fraction of CD150$^+$CD48$^-$LSK cells (Figure 6c).

To systematically identify all of the α-*catulin*-GFP$^+$c-kit$^+$ HSCs within a large segment of bone marrow we implemented a clearing technique (Becker et al., 2012; Dodt et al., 2007), which permitted deep confocal imaging as well as computational

approaches to digitally reconstruct three-dimensional segments of bone marrow. After antibody staining of half bones or bone marrow plugs from *α-catulin*$^{GFP/+}$ mice we cleared the specimens (Figure 3d versus e) then used confocal microscopes to acquire tiled, Z-stacked optical sections throughout the bone marrow to a depth of up to 600 μm.

We identified all *α-catulin*-GFP^{+}c-kit^{+} HSCs within large segments of bone marrow and assessed their localization relative to other cell types (Figure 3f-m). Isotype controls showed low levels of background fluorescence that could readily be distinguished from positive signals (Figure 7). The complex, three-dimensional datasets are difficult to present effectively in two-dimensional images. In some figures, we computationally masked specific features of images so that the relationship of HSCs to other features could be presented more clearly (e.g. Figure 3f versus 2.3g). We also include videos that animate three-dimensional images of the bone marrow to show the localizations of HSCs, niche cells, vasculature, and bone surfaces (Supplementary videos 2.1-2.3). Note that when thick specimens are collapsed into a single 2 dimensional image on the printed page, *α-catulin*-GFP^{+} cells and c-kit+ cells can appear much more frequent than they actually are because all of the cells from the thick specimens are collapsed into a single 2 dimensional image (e.g. see Figure 8i versus 2.8j). Note as well that in thick specimens there are cases in which an *α-catulin*-GFP^{+} cell and a c-kit^{+} cell are present in different optical planes but appear to be a single *α-catulin*-GFP^{+}c-kit^{+} cell when collapsed into a single 2 dimensional image. For this reason, cells we identified as *α-catulin*-GFP^{+}c-

kit$^+$ were individually examined at high magnification in a three-dimensional rendering of the entire dataset to confirm double labeling of single cells.

To systematically analyze the location of α-*catulin*-GFP$^+$c-kit$^+$ HSCs relative to bone surfaces we divided the bone marrow in the tibia diaphysis (shaft) into concentric cylindrical volumes that each encompassed 10% of the marrow volume (Figure 9a). Although HSCs were found throughout the marrow, they were significantly enriched toward the center of the marrow and depleted near the bone surface (Figure 10a). A recent study that divided bone marrow into concentric cylinders that each accounted for 10% of the marrow radius concluded that HSCs were more enriched close to bone surfaces (endosteum) (Kunisaki et al., 2013). However, that study did not control for the increase in marrow volume due to the increased circumference of outer versus inner cylinders (Figure 9b). When we normalized those data to control for differences in marrow volume, they also appeared to show a higher HSC density in the central marrow (data not shown).

HSCs have been suggested to be enriched within trabecular bone (metaphysis) as compared to cortical bone (diaphysis) (Sugimura et al., 2012; Zhang et al., 2003), though these studies did not use HSC-specific markers(Kiel et al., 2007a, 2007b). We found that the frequencies of CD150$^+$CD48$^-$LSK HSCs and *catulin*-GFP$^+$c-kit$^+$ HSCs were both significantly lower in the epiphysis and metaphysis as compared to the diaphysis by flow cytometry in the femur and tibia (using WBM from crushed bones; Figure 8a,c,f,g). Consistent with this, three-dimensional confocal imaging of bisected tibias showed the frequency of α-*catulin*-

GFP$^+$c-kit$^+$ HSCs was significantly lower in the metaphysis as compared to the diaphysis (Figure 8h). Thus, both deep imaging and flow cytometric analysis indicate that HSCs are more enriched in the diaphysis as compared to the metaphysis when using markers that give high levels of HSC purity.

We measured the nearest distance from each *α-catulin*-GFP$^+$c-kit$^+$ HSC in a bisected tibia to a bone surface in three dimensions. In the diaphysis, HSCs were significantly less likely than randomly placed spots to localize close to a bone surface (Figure 10b; random spots were distributed throughout areas occupied by hematopoietic cells but excluded from areas occupied by bone or blood vessel lumens). Only 0.65±0.58% of HSCs were within 10μm of a bone surface in the diaphysis (Figure 10d) and 86±6.1% were more than 80μm away (Figure 10b). In the metaphysis, the localization of HSCs relative to bone surfaces did not significantly differ from the distribution of random spots: 7.0±4.1% of HSCs were within 10μm of a bone surface (Figure 10e) and 53±11% were more than 80μm away (Figure 10c). These data are consistent with our observation that fewer than 10% of CD150$^+$CD48$^-$Lineage$^-$ HSCs were within 10μm of bone in femur sections (Kiel et al., 2005, 2007a).

Schwann cells and nerve fibers are present in the bone marrow (Katayama et al., 2006; Méndez-Ferrer et al., 2010b; Yamazaki et al., 2011) but it is not clear whether HSC niches are innervated or how the position of nerve fibers compares to HSCs. We found that GFAP$^+$ Schwann cells and nerve fibers clustered in the center of the marrow in the diaphysis (Figure 11a,b). HSCs did not significantly differ from

random spots in their distance from GFAP$^+$ cells (Figure 10f). Only 6.2±3.0% of α-*catulin*-GFP$^+$c-kit$^+$ HSCs were within 10μm of GFAP$^+$ cells in the bone marrow but 28±3.8% were within 30μm (Figure 10f). Thus, HSCs and niche cells rarely have contact with Schwann cells or nerve fibers but a subset of HSCs may be close enough to be regulated by diffusible factors secreted by Schwann cells (Yamazaki et al., 2011).

HSCs were significantly more likely than random spots to be close to *Cxcl12*-DsRed^{high} stromal cells. 97±1.2% of HSCs were within 5μm of *Cxcl12*-DsRed^{high} stromal cells (Figure 10h), which are an important element of the HSC niche (Ding and Morrison, 2013; Greenbaum et al., 2013; Omatsu et al., 2014; Sugiyama et al., 2006b). Although the Cxcl12^{high} stromal cells represent only 0.3% of WBM cells (Zhou et al., 2014), they have long processes that extend throughout the marrow (Suppl. video 2). Consequently, 89.2±4.9% of random spots were also present within 5μm of a *Cxcl12*-DsRed^{high} stromal cell (Figure 10h). 94±2.5% of HSCs appeared to have cell-cell contact with a *Cxcl12*-DsRed^{high} stromal cell (Figure 10i). Of those, 30±3.6% appeared to contact the cell body (Figure 10j and 2.10k) and 70±3.6% appeared to contact a cellular process (Figure 10j).

Consistent with our observation that virtually all *Scf*-expressing and *Cxcl12*^{high} stromal cells are LepR$^+$ (Zhou et al., 2014), 93.±3.7% of α-*catulin*-GFP$^+$c-kit$^+$ HSCs were within 5μm of a LepR$^+$ cell (Figure 10m). LepR$^+$ cells were visualized using *LepR^{cre}; tdTomato* mice in these experiments but 99% of Tomato$^+$ bone marrow cells in 8-12 week old *LepR^{cre}; tdTomato* mice also stain with an antibody against

LepR(Zhou et al., 2014). HSCs were significantly more likely than random spots to be close to $LepR^+$ cells (Figure 10m) and almost always contacted a $LepR^+$ cell (Figure 10l).

We next imaged the localization of HSCs relative to three kinds of blood vessels in the bone marrow: arterioles, sinusoids, and transition zone capillaries[47]. Blood enters the marrow via arterioles, which are variable in diameter, lined by smooth muscle, and have a continuous basal lamina (Figure 12). Sinusoids carry blood to the central sinus where it leaves the marrow through venous circulation. They are large in diameter, with a fenestrated basal lamina (Figure 12). Transition zone capillaries connect arterioles to sinusoids, are close to the bone surface, small in diameter, and have a continuous basal lamina (Figure 12). We distinguished blood vessels based on these characteristics, using anti-laminin antibody staining to visualize the basal lamina (Figure 13a and 2.13b).

α-catulin-GFP^+c-kit^+ HSCs significantly differed from random spots in their distance to arterioles: they were slightly less likely than random spots to be within 25μm of an arteriole but slightly more likely than random spots to be 30 to 50μm away (Figure 13c). Only 15±2.3% of HSCs were within 10μm of an arteriole (Figure 13f). In contrast, 84±6.2% of HSCs were within 10μm of a sinusoid (Figure 13g). HSCs did not significantly differ from random spots in terms of their localization relative to sinusoids (Figure 13d), presumably because sinusoids are present throughout the bone marrow. This makes the important point that although HSCs are nearly always close to a sinusoid, they are not spatially restricted within the bone

marrow as has often been proposed. HSCs are modestly enriched within the central marrow of the diaphysis but otherwise are present throughout the entire bone marrow.

HSCs also significantly differed from random spots in their proximity to transition zone blood vessels because they were less likely than random spots to be within 25μm of these vessels (Figure 13e). Only 12±2.1% of HSCs were within 10μm of a transition zone blood vessel (Figure 13h). Since transition zone vessels occupy the outer 20% of bone marrow, close to the endosteum, the depletion of HSCs near these vessels is consistent with our observation that HSCs are less common near the endosteum (Figure 10a).

Overall, 85±3.1% of HSCs were closer to sinusoids than other blood vessels (significantly more than random spots; Figure 13i and 2.13k). Only 7.7±2.3% of HSCs were closest to an arteriole (not significantly different from random spots; Figure 13i and 2.13j) and 6.8±1.8% were closest to a transition zone vessel (significantly fewer than random spots; Figure 13i and 2.13l). We have not detected any differences between male and female mice in the localization of HSCs with respect to central marrow, arterioles, sinusoids, or TZ vessels (Figure 14). Since the vast majority of α-*catulin*-GFP^{+}c-kit^{+} cells were quiescent (Figure 6) and the vast majority of α-*catulin*-GFP^{+}c-kit^{+} cells (Figure 13i) localized nearest to sinusoids, this suggests that most quiescent HSCs are in perisinusoidal niches.

The ability to deep image large segments of bone marrow allowed us to localize much larger numbers of HSCs than prior studies. This allowed us to

systematically compare the localization of dividing Ki-67$^+$ *α-catulin*-GFP$^+$c-kit$^+$ HSCs (Figure 15b, c; which accounted for 15±2.0% of HSCs) and non-dividing Ki-67$^-$ *α-catulin*-GFP$^+$c-kit$^+$ HSCs (Figure 15a). Both dividing and non-dividing HSCs were most closely associated with sinusoids (Figure 15e): 81±5.9% of Ki-67$^+$ *α-catulin*-GFP$^+$c-kit$^+$ cells and 79±14% Ki-67$^-$ *α-catulin*-GFP$^+$c-kit$^+$ cells were within 10μm of a sinusoid (Figure 15h). In contrast, only 12±7.3% of Ki-67$^+$ *α-catulin*-GFP$^+$c-kit$^+$ cells and 16±7.4% Ki-67$^-$ *α-catulin*-GFP$^+$c-kit$^+$ cells were within 10μm of an arteriole (Figure 15d and 2.15g). 16±4.5% of Ki-67$^+$ *α-catulin*-GFP$^+$c-kit$^+$ cells and 14±4.8% Ki-67$^-$ *α-catulin*-GFP$^+$c-kit$^+$ cells were within 10μm of a transition zone vessel (Figure 15f and 2.15i). None of the differences between dividing and non-dividing HSCs were statistically significant except that dividing HSCs tended to be closer to transition zone vessels near the bone surface.

Overall, 79±9.3% of Ki-67$^+$ *α-catulin*-GFP$^+$c-kit$^+$ dividing HSCs were most closely associated with sinusoids, 14±9.8% were most closely associated with transition zone vessels, and 7.5±3.5% were most closely associated with arterioles (Figure 15j). Similarly, 81±6.0% of Ki-67$^-$ *α-catulin*-GFP$^+$c-kit$^+$ non-dividing HSCs were most closely associated with sinusoids, 9.0±6.8% with transition zone vessels, and 9.9±3.7% with arterioles (Figure 15j). Ki-67$^+$ *α-catulin*-GFP$^+$c-kit$^+$ dividing HSCs were significantly more likely than Ki-67$^-$ *α-catulin*-GFP$^+$c-kit$^+$ non-dividing HSCs to localize close to the bone surface (Figure 15k).

Our results are not consistent with the idea that quiescent HSCs reside in arteriolar niches associated with *NG2*-CreER-expressing stromal cells (Kunisaki et al., 2013). The data in our study and the study by Kunisaki et al. (Kunisaki et al., 2013) both show that there is a higher density of HSCs per unit marrow volume in the central marrow as compared to the endosteal marrow and that most HSCs are closer to sinusoids as compared to arterioles. While Kunisaki et al. concluded that NG2^{+}Nestin^{high} periarteriolar cells, not LepR^{+} perisinusoidal cells, express the highest levels of *Scf* and *Cxcl12*, the RNAseq data on which this conclusion was based showed that the "Nestin^{high}LepR^{-}" cells they analyzed were negative for *Nestin* and positive for *Lepr* expression (see GSE48764 in the Gene Expression Omnibus (Kunisaki et al., 2013)). Thus, their data also show that the cells that express *Scf* and *Cxcl12* are LepR^{+} (Zhou et al., 2014).

To address this issue directly we generated *NG2^{CreER}; Rosa$^{tdTomato/+}$; Scf$^{GFP/+}$* and *NG2^{CreER}; Rosa$^{YFP/+}$; Cxcl12$^{dsRed/+}$* mice. While 97% of *Scf*-GFP^{+} stromal cells and 96% of *Cxcl12*-DsRed^{high} stromal cells were LepR^{+}, we did not detect any expression of *NG2*-CreER in these cells (Figure 16a, b, g, h). We also conditionally deleted *Scf* or *Cxcl12* with *NG2*-CreER but did not detect any effect on bone marrow cellularity, HSC frequency, hematopoietic progenitor frequency, or bone marrow reconstituting capacity upon transplantation into irradiated mice (Figure 16c-f and i-l). *NG2*-CreER-expressing cells are therefore not a source of SCF or Cxcl12 for HSC maintenance in the bone marrow.

2.4 Discussion

Although Kunisaki et al. observed HSC depletion when *NG2*-CreER-expressing cells were ablated from the bone marrow with diphtheria toxin, there is no bone marrow cell population that when ablated has not led to HSC depletion, including osteoblasts (Visnjic et al., 2004; Zhu et al., 2007) and *Nestin*-CreER-expressing cells (Méndez-Ferrer et al., 2010b) neither of which are significant sources of HSC niche factors (Ding and Morrison, 2013; Ding et al., 2012; Greenbaum et al., 2013). The could reflect extensive cross regulation in the bone marrow in which many cell populations indirectly regulate each other, or the non-specific activation of HSCs by tissue damage. Our data are consistent with recent studies that found quiescent HSCs co-localize with megakaryocytes in the bone marrow (Bruns et al., 2014) as megakaryocytes localize around sinusoids (Lichtman et al., 1978).

Our data demonstrate that both dividing and non-dividing HSCs are most closely associated with sinusoids and that few cells from either population are closely associated with arterioles or bone surfaces. Our data provide little support for the idea that dividing and non-dividing HSCs reside in spatially distinct niches, with the exception that dividing HSCs were more likely than non-dividing HSCs to localize near the endosteum. Nonetheless, it remains possible that there are distinct perisinusoidal domains for dividing and non-dividing HSCs. Deep imaging and digital reconstruction of large three-dimensional segments of bone marrow makes it possible to systematically and quantitatively assess the localization of each

hematopoietic stem and progenitor cell populations relative to every other bone marrow component.

2.5 Methods

To perform bone and bone marrow imaging, tibias or femurs were removed from 8-12 week old *α-catulin*$^{GFP/+}$ mice and immediately fixed in 4% paraformaldehyde for 7 hours at 4°C. Fixed bones were cryoprotected in 30% sucrose in PBS overnight at 4°C, then immersed in OCT and flash frozen using liquid nitrogen. Frozen bones were longitudinally bisected using a cryostat, then the OCT was washed away and the half bones were incubated in blocking solution overnight at room temperature. The half bones were then incubated in primary antibodies for 3 days at room temperature, followed by one day of washes in PBS, then secondary antibody incubation for another 3 days at room temperature, followed by another day of washes. The antibody-stained half tibia bones were then cleared by ethanol dehydration followed by incubation in benzyl alcohol:benzyl benzoate 1:2 mix (BABB clearing (Becker et al., 2013; Dodt et al., 2007)). In some experiments, intact marrow plugs were first ejected from the diaphysis of the tibia using a 4% PFA filled-syringe with a 25G needle. The marrow plugs were then fixed for 3 hours at room temperature followed by the same staining protocol as described above. A Zeiss LSM780 or a Leica SP8 confocal microscope was used to take Z stack images of stained and cleared half bones or bone marrow plugs. In some samples, bone was visualized by second harmonic generation (SHG) imaging using a Zeiss LSM780

with a Coherent Chameleon Vision II pulsed NIR laser. The images were analyzed using Imaris (Bitplane) software.

Mice. The targeting construct for *α-catulin*$^{GFP/+}$ mice was generated by recombineering (Liu et al., 2003). Linearized targeting vector was electroporated into Bruce4 ES cells. Correctly targeted ES cell clones were identified by Southern blotting and injected into C57BL/6-Tyr$^{c\text{-}2J}$ blastocysts. The resulting chimeric mice were bred with C57BL/6-Tyr$^{c\text{-}2J}$ mice to obtain germline transmission. Then the *Frt-Neo-Frt* cassette introduced by the targeting vector was removed by mating with Flpe mice (Rodríguez et al., 2000). These mice were backcrossed onto a C57BL/Ka background and germ-line transmission was checked by PCR. C57BL/Ka-Thy-1.1(CD45.2) and C57BL/Ka-Thy-1.2(CD45.1) mice were used in transplant experiments. Male and female mice from eight to twelve weeks old were used for all studies. *Scf*$^{GFP/+}$ and *Scf*^{fl} mice (Ding et al., 2012), *Cxcl12*$^{DsRed/+}$ and *Cxcl12*^{fl} mice (Ding and Morrison, 2013), *LepR-Cre* mice (DeFalco et al., 2001), *Rosa26-CAG-loxp-stop-loxp-tdTomato* conditional reporter mice (Madisen et al., 2010), *Rosa26-loxp-stop-loxp-EYFP* conditional reporter mice (Srinivas et al., 2001), and *NG2-CreER* mice (Zhu et al., 2011) were all previously described. All mice were housed in AAALAC-accredited, specific-pathogen-free animal care facilities at the UT Southwestern Medical Center (UTSW). All procedures were approved by the UTSW Institutional Animal Care and Use Committee.

HSC isolation and flow cytometry. Bone marrow cells were isolated by either flushing the long bones (tibias and femurs), or by crushing the bones using a mortar and pestle in Ca^{2+} and Mg^{2+} free Hank's buffered salt solution (HBSS, Gibco) supplemented with 2% heat inactivated bovine serum (Gibco). Spleen cells were prepared by crushing the spleen between two glass slides. The cells were gently passed through a 25G needle then filtered using a 100 µm mesh to generate a single cell suspension. Viable cell number was calculated using a Vi-Cell cell counter (Beckman Coulter) or by counting manually with a hemocytometer. For HSC identification by flow cytometry, the cells were stained with antibodies against CD150 (TC15-12F12.2), CD48 (HM48-1), Sca1 (E13-161-7), and c-kit (2B8), as well as the following lineage markers: CD42d (1C2), CD2 (RM2-5), CD3 (17A2), CD5 (53-7.3), CD8 (53-6.7), B220 (6B2), Ter119 (TER-119), and Gr1 (8C5). Antibody staining of cell suspensions was always performed at 4°C for 20 minutes. After antibody staining, the cells were stained with the viability dyes 4′,6-diamidino-2-phenylindole (DAPI; 2 µg/ml in PBS) or propidium iodide (PI; 1 µg/ml) to exclude dead cells during flow cytometry. To identify other hematopoietic progenitors (CLPs, CMPs, GMPs and MEPs; see Figure 4) we stained cell suspensions with antibodies against CD34 (RAM34), CD127 (Il7Rα, A7R34), CD16/32 (FcγR, 93), Sca1 (E13-161-7), c-kit (2B8) and the lineage markers listed above. Stains that involved anti-CD34 antibody were conducted for 90 minutes on ice. To identify myeloid cells, erythrocytes, megakaryocytes, T cells, B cell progenitors and B cells the following antibodies were used: anti-Gr1 (8C5), anti-CD11b (Mac1, M1-70), anti-Ter119 (TER-

119), anti-CD41(MWReg30), anti-CD3 (17A2), anti-CD4 (GK1.5), anti-CD8 (53-6.7), anti-B220 (6B2), anti-IgM (II/41), anti-CD24 (M1/69), and anti-CD43 (1B11). For Figure 16, Ter119 (TER-119), CD45 (30-F11), and CD31 (MEC13.3) antibodies were used to mark erythrocytes, nucleated hematopoietic cells, and endothelial cells respectively. Goat anti-mouse Leptin Receptor biotinylated antibody (BAF497, Fisher Scientific) and Streptavidin-BV421 (405226, Biolegend) were used to mark $LepR^+$ cells. Antibodies were conjugated to one of the following dyes depending on the experiment and cell population: PE-Cy5, PerCP-eFluor710, PE-Cy7, PE, APC, APCeFluor 780, APC-H7, PerCP-Cy5.5, eFluor 660, Alexa Fluor 700, PE-Cy5.

Colony formation in methylcellulose. Individual HSCs were sorted into methylcellulose culture medium (3434, Stemcell Technologies) in 96 well plates (one cell/well). After sorting the plates were kept at 37°C in a cell culture incubator with 6.5% CO_2 and constant humidity for 14 days. Then colonies were counted and identified based on size and morphology using an Olympus IX81 inverted microscope.

Bone marrow preparation from metaphysis and diaphysis for FACS analysis. To compare bone marrow from the epiphysis/metaphysis to the diaphysis, the metaphysis was separated from the diaphysis using scissors at the point where the central sinus branches (see Figure 8). Then each segment of bone was crushed using a mortar and pestle and small bone fragments were suspended in staining

medium (Ca^{2+} and Mg^{2+}-free Hank's buffered salt solution (HBSS, Gibco) supplemented with 2% heat inactivated bovine serum (Gibco)) and gently triturated until no marrow was visibly attached to the bone. The cell suspension was filtered through a 100μm mesh to obtain a single cell suspension. The cell suspensions were then analyzed to determine cellularity and HSC frequency.

Competitive reconstitution assays in irradiated mice. Adult recipient mice were administered a minimum lethal dose of radiation using an XRAD 320 X-ray irradiator (Precision X-Ray) to deliver two doses of 540 rads at least 3 hours apart. Cells were transplanted by injection into the retro-orbital venous sinus of anesthetized recipient mice. 300,000 recipient whole bone marrow (WBM) cells were transplanted along with the donor cells. For secondary transplants, 3 million WBM cells from primary recipient mice were transplanted into irradiated secondary recipient mice. Blood was collected from the tail vein of recipient mice at 4 week intervals after transplantation for at least 16 weeks after transplantation. For analysis of the levels of donor cells in peripheral blood, red blood cells were lysed with ammonium potassium buffer then the remaining cells were stained with antibodies against CD45.1 (A20), CD45.2 (104), CD11b (Mac1, M1-70), Gr-1 (8C5), B220 (6B2), and CD3 (17A2).

Cell cycle analysis. For analysis of DNA content in HSCs and other hematopoietic cells, the cells were isolated by flow cytometry as described above and sorted directly into 70% ethanol then stored at -20°C for at least 24 hours. The cells were

washed multiple times with staining medium (see above) then incubated in staining medium containing 50µg/ml propidium iodide (Molecular Probes) for 30 minutes at room temperature and analyzed using a FACSAria or FACSCanto II flow cytometer (BD Biosciences). Data were analyzed using FACSDiva (BD Biosciences) or FlowJo (Tree Star) software. To assess 5-bromo-2'-deoxyuridine (BrdU) incorporation in vivo mice were intraperitoneally injected with a single dose of BrdU (1mg BrdU/10g body mass) then maintained on 0.5mg BrdU/ml drinking water for three days. For analysis of BrdU incorporation into HSCs bone marrow cells were stained with the following antibodies that were selected to survive fixation: anti-CD150-BV421, anti-CD48-AF700, anti-CD2-PE, anti-CD3-PE, anti-CD5-PE, anti-CD8-PE, anti-Ter119-PE, anti-Gr1-PE, anti-Sca1-PerCpCy5.5 and c-kit-APCH7 (BD Biosciences; antibody clones are as described above for HSC isolation and flow cytometry). For isolation of *α-catulin*-GFP^{+}c-kit^{+} cells, bone marrow cells were stained with anti-c-kit-APCH7 antibody. After antibody staining, the target cell populations were double sorted to ensure purity, then fixed and stained with an anti-BrdU antibody using the BrdU APC Flow Kit (BD Biosciences) according to the manufacturer's instructions.

Sorting of *α-catulin*-GFP^{+}c-kit^{+} cells to determine cell diameter. Bone marrow cells from *a-catulin*$^{GFP/+}$ mice were prepared for flow cytometric analysis as described above. Biotinylated anti-c-kit antibody (2B8 clone, 13-1171-85, eBiosciences) followed by streptavidin-AF647 (S32357, Life Technologies) were used to stain bone marrow cells. *α-catulin*-GFP^{+}c-kit^{+} cells were sorted into a drop of

staining medium on a slide coated with poly-D-lysine (0.5mg/ml poly-D-lysine in water was used to coat the slides over night at room temperature). Slides were incubated for 45 minutes at 4°C to let the sorted cells attach to the slide surface. Then a 16% PFA stock solution was added gently into the drop of staining medium to achieve a final PFA concentration around 4%. Cells were fixed for 10 minutes at room temperature and washed multiple times with PBS. Then the cells were stained with DAPI (2 µg/ml in PBS), with 0.1% IgePal630 (Sigma) for 30 minutes, followed by multiple washes in PBS. Prolong gold antifade (Life Technologies) was used to mount the cells. An LSM780 confocal microscope (Leica) was used to image the cells and Imaris software was used to measure cell diameter.

microCT analysis of bones. Dissected intact femurs from 10-12 week old littermate mice were fixed in 4% PFA overnight at 4°C. Then the bones were washed multiple times with 70% ethanol and stored in 70% ethanol until they were scanned using a Scanco Medical µCT 35 machine at the Texas A&M University Baylor College of Dentistry. The scan was performed with a 3.5 µm voxel size resolution, 55kV, 145µA, and an integration time of 800 ms. Scanco software was used for analysis. A common reference point was determined for all bones scanned based on the growth plate, and trabecular and cortical regions were analyzed for each bone.

PCR genotyping. The following primers were used to genotype *a-catulin*^{GFP} allele: Cin-G1, 5'- GAAGTAGTGGCACAAGGGTAGGGG-3'; Cin-G2, 5'-

GGCCGCGGTACCTGAGAAAC-3'; Cin-G3, 5'-GTTGCCGTCGTCCTTGAAGAAG-3'. Genotyping primers for *Cxcl12*^{DsRed} mice(Ding and Morrison, 2013) were previously reported.

Immunofluorescence, clearing, microscopy, and analysis.

Half bone whole mount tissue preparation for imaging: Freshly dissected tibia were fixed in cold 4% paraformaldehyde (PFA) in PBS (Affymetrix) for 7-8 hours at 4°C while shaking. The bones were washed with PBS to remove the PFA and cryoprotected in 30% sucrose PBS solution overnight at 4°C while shaking. The bones were embedded in OCT (Fisher) and flash frozen in liquid nitrogen. A Leica cryostat was used to longitudinally bisect the bones. Intact half bone was washed in PBS to remove OCT then processed for staining, clearing and imaging as below.

Bone marrow whole mount plug preparation for imaging: Intact bone marrow plugs from freshly dissected tibia were extruded from the bone using a PFA filled syringe with a 25G needle and placed directly into 4% PFA solution for 3 hours at room temperature. Fixed plugs were then washed in PBS before being stained, cleared and imaged as below.

Whole mount immunostaining: All staining procedures were performed in Eppendorf tubes on a rotator at room temperature. The staining solution contained 10% DMSO, 0.5% IgePal630 (Sigma), and 5% donkey serum (Jackson Immuno) in PBS. Half bones and plugs were blocked in staining solution containing anti-CD16/32 mouse Fc blocking antibody (BD Biosciences) and 1% BlokhenII (Aves Labs) over night at

room temperature. After blocking, half bones were stained for 3 days at room temperature with primary antibodies in staining solution. Then the tissues were washed multiple times in PBS at room temperature for one day and put into staining solution containing secondary antibodies for 3 days followed by a one day wash to remove any unbound secondary antibodies. Antibodies used for whole mount staining included chicken anti-GFP (GFP-1020, Aves Labs), goat anti-c-kit (BAF1356, R&D Systems), rabbit anti-Laminin (ab7463, abcam), rat anti-Ki-67 (SolA15, eBioscience), Alexa Fluor 647-AffiniPure F(ab')2 Fragment Donkey Anti-Chicken IgY, Alexa Fluor 488-AffiniPure F(ab')2 Fragment Donkey Anti-Rabbit IgG, AMCA-AffiniPure F(ab')2 Fragment Donkey Anti-Rabbit Ig, Alexa Fluor 488-AffiniPure F(ab')2 Fragment Donkey Anti-Rat IgG (all from Jackson ImmunoResearch), and 555 or 488 conjugated donkey anti-goat (A-11055 and A-21432 from Life Technologies). For isotype control staining in Figure 7, Goat IgG control (BAF108, R&D Systems), Rabbit IgG control (ab27478-100, Abcam), Rat IgG control (012-000-003, Jackson Immuno) and Non-Immune Chicken IgY control (N-1010, Aves Labs) were used along with the secondary antibodies described above. The fixation time of the tissue, using 0.5% IgePal630 and 10% DMSO in the staining solution, and incubation of the tissue for 3 days in both primary and secondary antibodies were critical factors for efficient deep penetration of antibodies throughout the whole mount tissue. For anti-Ki-67 antibody penetration, before the blocking step, treatment of the tissues with 0.05% SDS over-night in PBS was necessary.

Comparison of clearing protocols: Scattering and spherical aberration due to refractive index mismatch limit the maximum depth of penetration of visible light into aqueous tissue to about 100μm (Zhu et al., 2013). Optical clearing agents can decrease the amount of scattered light and therefore increases the depth of penetration. Most optical clearing agents work by replacing the low refractive index, aqueous components of the tissue with agents of a higher refractive index to match that of the tissue such as collagen and cell components. Because each tissue has unique properties, such as density of cells and extracellular matrix, the optimum tissue clearing method must be determined empirically. Bone marrow does not have a high lipid content and therefore, unlike brain, is not limited by the opacity of lipids. Therefore clearing methods that remove the lipid with SDS by either electrophoresis (Chung et al., 2013) or passive flow (Yang et al., 2014) were ineffective and had the additional disadvantage of SDS destruction of cell surface epitopes. Bone marrow is very densely packed with cells, which likely explains why optical clearing agents and methods with lower refractive indices such as Sca/eA2 (Hama et al., 2011), CUBIC (Susaki et al., 2014), and Focus Clear (Chung et al., 2013) did not efficiently clear the marrow in our hands. We found Murray's clear (1:2 Benzyl Alcohol: Benzyl Benzoate or BABB) (Becker et al., 2013) to be the most effective clearing method, but it is only compatible with antibodies conjugated with stable chemical fluorophores, such as the Alexa Fluor dyes. Murray's clear rapidly quenches fluorescent proteins, so GFP^+ cells were identified using an antibody against GFP when performing deep imaging of tissues. For imaging bone marrow cells from

Cxcl12^{dsRed} or *LepR*^{cre}*; tdTomato* mice we used the 3DISCO (Ertürk et al., 2012) clearing method because THF and DBE preserve endogenous fluorescence better than BABB, although they did not clear the tissue as effectively as Murray's clear.

Tissue clearing using modified Murray's clear: All clearing of half bones and bone marrow plugs was performed in Eppendorf tubes on a rotator at room temperature. Immunostained tissues were washed in PBS and dehydrated in either a methanol or ethanol dehydration series then incubated for 3 hours in methanol or overnight in ethanol with several changes of 100% alcohol. The alcohol was then exchanged with BABB. The tissues were incubated in BABB for 3 hours to overnight with several exchanges of fresh BABB. Half bones or bone marrow plugs were mounted in BABB between two cover slips and sealed with silicone (Premium waterproof silicone II clear, General Electric). As previously published(Becker et al., 2012), we found it necessary to clean the BABB of peroxides (which can accumulate as a result of exposure to air and light) by adding 10g of activated aluminum oxide (Sigma) to 40ml of BABB and rotating for at least 1 hour, then centrifuging at 2000xg for 10 minutes to remove the suspended aluminum oxide particles.

Confocal imaging of thick tissue: Three dimensional confocal microscopy of the bone marrow at sub-micron resolution requires specialized equipment. We used both a Zeiss LSM780 and a Leica SP8 resonant scanning confocal. Specifications for the Zeiss LSM780: AxioExaminer upright stand; 405, 488, 561, 594 and 633 nm visible laser lines; internal 32-channel GaAsP detector; Prior OptiScan motorized stage; Coherent Chameleon Vision II pulsed NIR laser for two photon excitation; Zeiss BiG

two channel nondescanned detector. Specifications for the Leica: Acousto Optical Beam Splitter, Spectral detection, 8kHz Resonant tandem scanner, HyD hybrid detectors, and 405, 488, 561, 633 nm laser lines. The optimum clearing agent (BABB) for bone marrow has a refractive index of 1.56, similar but not identical to standard immersion oil. Deep imaging also requires a long working distance objective. For the Zeiss LSM780 we found the best available objective was a Zeiss LD LCI Plan-Apo 25x/0.8 multi-immersion objective lens, which has a 570 µm working distance. We used Immersol 518F immersion oil for Zeiss LSM780 imaging. For the Leica SP8, we used an HCX APO L20x/0.95 BABB immersion objective with a 1.95 mm working distance. High resolution imaging of large volumes of thick tissue by acquisition of tiled Z-stacks is very time consuming, thus it was important to optimize the acquisition settings for each microscope to minimize acquisition time while preserving adequate resolution and signal to noise ratio. On the Zeiss LSM780 images were taken at 512X512 pixel resolution with 2 µm Z-steps, pinhole for the internal detector at 47.7 µm. Bone was imaged by second-harmonic generation (SHG) with 850 nm pulsed NIR excitation using the nondescanned detector. On the Leica SP8, images were taken using the resonance scanner using 8X line averaging with the minimum zoom of 1.25X at 812X812 pixel resolution, pinhole at 44.7 µm, and 2µm Z-steps.

Image annotation and analysis. Confocal tiled Z-stack images were rendered in 3 dimensions and analyzed using Bitplane Imaris v7.7.1 software installed on a Dell

Precision T7610 64-bit workstation with Dual Intel Xeon Processor E5-2687W v2 (Eight Core HT, 3.4GHz Turbo, 25 MB),128GB RAM, and 16 GB AMD FirePro W9100 graphics card. Individual α-*catulin*-GFP^{+}c-kit^{+} HSCs were identified using the Ortho slicer function in Imaris software to visualize digital serial sections of the large 3D image. We identified HSCs as having a round morphology, with GFP throughout the cell, and c-kit expression surrounding the cell surface. These criteria prevented false positive identification of cellular debris or α-*catulin*-GFP^{+}c-kit^{-} endothelial cells with elongated cell body morphology. HSC co-ordinates and size were interactively annotated using the Imaris spots function in manual mode. Bone and non-myelinating Schwann cells were segmented based on thresholding of the second harmonic generation (SHG, which detects collagen fibers in bone) or GFAP channels, respectively, using the Imaris surface function. Cortical and trabecular bone were then divided into separate surfaces interactively based on SHG signal and morphology. We used anti-laminin antibodies to immunofluorescently label all of the vasculature within the bone marrow. Arteries, arterioles, and capillaries have continuous basement membranes, which are observable as uniform laminin staining. In contrast, bone marrow sinusoids have a discontinuous fenestrated basement membrane (Inoue and Osmond, 2001). Laminin staining of sinusoids clearly demonstrates discontinuous basement membranes, thereby allowing unambiguous identification of sinusoidal vessels in the absence of other markers (Inoue and Osmond, 2001). Because we were able to image the entire marrow cavity we were able to trace and digitally label each artery and all of its subsequent branching into

smaller arteries and arterioles as they approached the endosteal surface. This is a great advantage of the deep imaging approach that allowed us to unambiguously identify vessels in a way that is not possible in thin sections where the connectivity of vessels cannot be traced.

Near the endosteum, arterioles connect to the smallest diameter vessels of the capillary network that line the endosteum. These capillaries then connect to larger diameter sinusoidal vessels. By carefully following the blood vessel paths in six samples, we determined that in the diaphysis the outer 20% of the marrow by volume contained all of the vessels involved in the transition from arteriole to sinusoid, i.e. the most distal portion of the arterioles, the connecting capillaries, and the initial portion of sinusoids. We identified this region as the transition zone in keeping with published criteria (Li et al., 2009). Therefore, we used the published morphological characteristics of orientation, location, and basement membrane continuity to subdivide blood vessels within the bone marrow. The Imaris surface function was used to create three distinct digital surfaces corresponding to each type of blood vessel. SHG signal was used to create bone surfaces. Three dimensional distances between HSCs and digital vessel or bone surfaces were calculated using the Imaris Distance Transform Matlab XTension and volumetric decile calculations were performed using a Matlab-based Imaris XTension. The annotated programs, entitled "Visualizing Progressive Zones of Equal Volume in a 3D Tissue (Matlab Extensions for Imaris)" are available for download from the Morrison lab protocols

webpage at the CRI website under "More Information" (http://cri.utsw.edu/sean-morrison-laboratory/more-information/).

Random spot generation and insertion. The original 3 dimensional images of the GFP channel in the Imaris format were used to generate random spots for each sample. In a 16 bit Imaris file of the original bone marrow image, 3 dimensional voxels were represented by signal intensity values that ranged between 0 and 65,535. Those signal intensity values were imported into MATLAB using the imreadBF package (http://www.mathworks.com/matlabcentral/fileexchange/32920-imread-for-multiple-life-science-image-file-formats) and the Bio-Formats software (http://www.openmicroscopy.org/site/products/bio-formats). The images were filtered to exclude low-intensity regions that included cracks in the specimen, blood vessel lumens, and fat bodies where HSCs were not found and random spots were not generated. The intensity-filtered images, of which the excluded portions were given zero intensity values, were processed with MATLAB's median filter to remove salt-and-pepper noise. Then the intensity images were converted to binary signals by turning any non-zero intensity value into “one”. Those “one” signals were used to determine the voxel locations that were used to generate random spots. The locations were randomly permuted, and enough random spot coordinates were designated to approximate the random spot distribution (more than 50,000 per bone). The random spot coordinates were transferred to Imaris to generate the random spots, and distances from random spots to cell types or landmarks in the

bone marrow were calculated based on the distance transformation files generated using landmark surfaces such as arterioles, sinusoids, transition zone vessels, and bone. We confirmed the randomness of the distribution of the random spots by measuring the frequency of random spots in each percentile of bone marrow volume. Random spots were given a diameter of 6 microns, similar to the observed average HSC diameter.

Statistical methods. To assess whether the distribution of HSCs significantly differed from random spots with respect to particular bone marrow landmarks, we used a normalized 2-sample Kolmogorov–Smirnov test. The 2-sample Kolmogorov–Smirnov test calculates and evaluates the maximum difference between the empirical cumulative distribution functions (ECDFs) of two test groups where each group is a vector of continuous values, which in our case were the distances from HSCs or random spots to particular bone marrow cell types or structures. Since we had multiple biological samples, we normalized them by the following approaches:

1. HSCs and random spot distances from the same sample were pooled to determine a range of distances, which was then used to generate 100 equal-length bins for each sample so that each bin represented 1% of the distance range for that sample.
2. For each sample, the number of HSCs or random spots in each bin was determined and normalized to percentages.

3. The average percentage of HSCs or random spots in each bin was calculated across all samples.

4. The averaged, binned percentages of HSCs or random spots were used to approximate the probability density functions (PDF), and the ECDFs were calculated based on those approximate PDFs.

5. MATLAB's 2-sample Kolmogorov–Smirnov test was used and slightly modified so that it accepted the two normalized ECDFs as inputs. The Kolmogorov–Smirnov p-values were adjusted using the Bonferroni method to account for multiple comparisons.

The data presented in figure panels reflect multiple independent experiments performed on different days using tissues from different mice. Sample sizes were not based on power calculations. No randomization or blinding was performed. Variation is always indicated using standard deviation. For analysis of the statistical significance of differences between two groups we first assessed whether variance in the two groups was similar using an F test (it always was) and then two-tailed Student's *t*-tests. Single factor ANOVA tests were used for comparisons in Figure 2.

Not all samples were suitable for image analysis and those that did not meet the criteria were not analyzed. Occasionally the antibody staining was not strong enough for us to detect HSCs or other landmarks in the deepest part of the bone marrow or the samples were damaged during processing. In these cases the samples were not analyzed. All mice used in our studies were between 8 and 12 weeks old, including both male and female mice. We did not observe any differences

in HSC localization among male and female mice (Figure 14), so the data were combined for purposes of analysis. All conclusions were based on data obtained from at least 3 independent experiments involving samples obtained from different mice and processed on different days.

Code availability. Code was written to separate bone marrow into volumetric deciles and to identify the transition zone in the outer 20% of bone marrow. This code is available on the Morrison lab protocols webpage at the CRI website under "More Information" (http://cri.utsw.edu/sean-morrison-laboratory/more-information/).

2.6 Figures

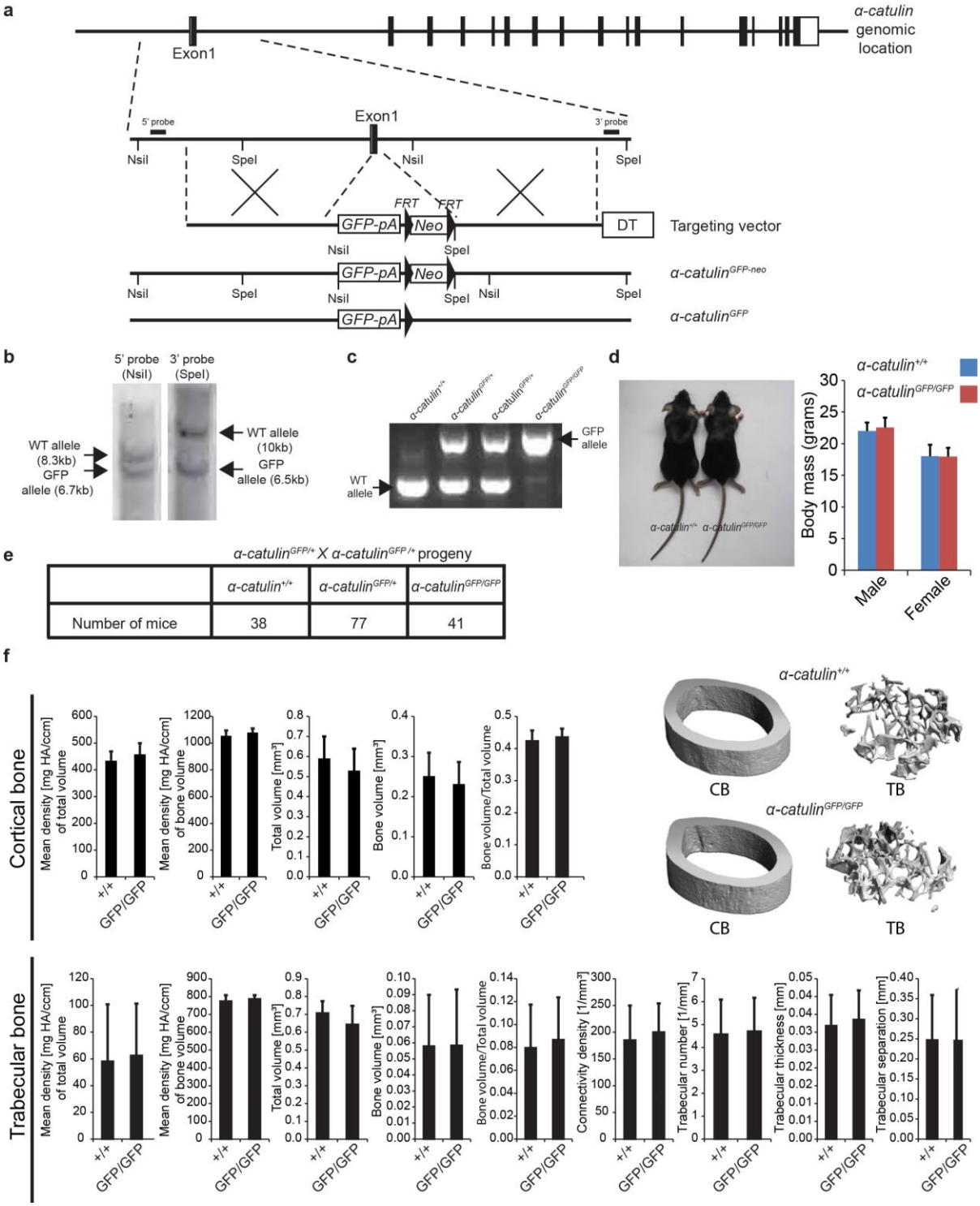
a
α-catulin genomic location
Exon1
5' probe
3' probe
NsiI
SpeI
FRT
GFP-pA
Neo
DT
Targeting vector
α-catulin^GFP-neo
α-catulin^GFP
b
5' probe (NsiI)
3' probe (SpeI)
WT allele (8.3kb)
GFP allele (6.7kb)
WT allele (10kb)
GFP allele (6.5kb)
c
GFP allele
WT allele
d
α-catulin+/+
α-catulinGFP/GFP
Body mass (grams)
Male
Female
e
α-catulinGFP/+ X α-catulinGFP/+ progeny
α-catulin+/+
α-catulinGFP/+
α-catulinGFP/GFP
Number of mice
38
77
41
f
Cortical bone
Mean density [mg HA/ccm] of total volume
Mean density [mg HA/ccm] of bone volume
Total volume [mm³]
Bone volume [mm³]
Bone volume/Total volume
+/+
GFP/GFP
CB
TB
Trabecular bone
Connectivity density [1/mm³]
Trabecular number [1/mm]
Trabecular thickness [mm]
Trabecular separation [mm]

Figure 1. Generation of *α-catulin*^{GFP} mice. a, The targeting strategy to generate the *α-catulin*^{GFP} allele is shown. The targeting vector was generated by retrieving a genomic fragment of the *α-catulin* gene, including exon1, from BAC clone RP24-146F11 by recombineering(Liu et al., 2003). The retrieved genomic region was then modified to replace most of the exon1 coding region and the exon1-intron1 junction with an *EGFP-bGH-pA-FRT-neo-FRT* cassette in frame with the first ATG of *α-catulin*. The final targeting vector was then linearized and electroporated into C57BL-derived Bruce4 ES cells. **b**, New NsiI and SpeI sites introduced with the *EGFP-bGH-pA-FRT-neo-FRT* cassette were used to screen correctly targeted ES cell clones by Southern blotting for 5' and 3' probes. Correctly targeted ES cells were used to generate chimeric mice. Upon confirmation of germ-line transmission by PCR, the *α-catulin*$^{GFP\text{-}neo}$ mice were crossed with *Flpe* mice(Rodríguez et al., 2000), to remove the neomycin resistance cassette. **c,** PCR genotyping of *α-catulin*$^{+}$ (*WT)* and *α-catulin*^{GFP} alleles from *α-catulin*$^{+/+}$, *α-catulin*$^{GFP/+}$ and *α-catulin*$^{GFP/GFP}$ mice. **d,** *α-catulin*$^{+/+}$ and *α-catulin*$^{GFP/GFP}$ mice did not show any difference in size or body mass (n=9 *α-catulin*$^{+/+}$ and 8 *α-catulin*$^{GFP/GFP}$ male mice, n=7 *α-catulin*$^{+/+}$ and 7 *α-catulin*$^{GFP/GFP}$ female mice, all were 8-10 weeks old). **e,** *α-catulin*$^{GFP/+}$ and *α-catulin*$^{GFP/GFP}$ mice were born at mendelian frequencies, survived into adulthood in normal numbers, and were apparently developmentally normal. The statistics reflect mice genotypes at 8-10 weeks of age. **f,** Cortical and trabecular femur bone (CB and TB) did not show any statistically significant differences among *α-catulin*$^{+/+}$ and *α-catulin*$^{GFP/GFP}$ mice by microCT (micro Computed Tomography) analysis (6 *α-*

catulin$^{GFP/GFP}$ and 5 *α-catulin*$^{+/+}$ controls at 10-12 weeks of age). HA refers to Hydroxyapatite. All data represent mean±s.d. The significance of differences between genotypes was assessed using Student's *t*-tests. None were statistical significant.

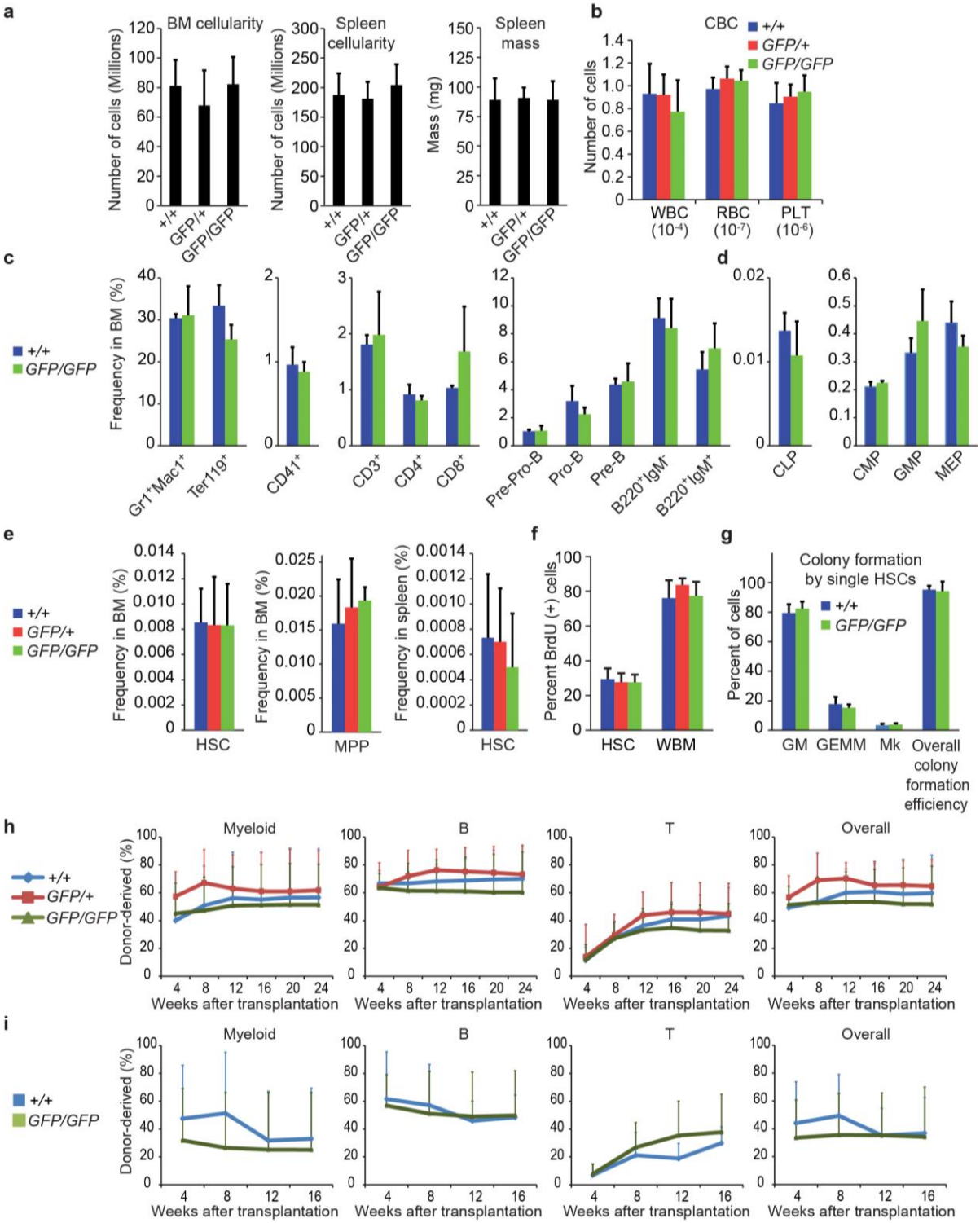
a
BM cellularity
Number of cells (Millions)
Spleen cellularity
Number of cells (Millions)
Spleen mass
Mass (mg)
+/+
GFP/+
GFP/GFP
b
CBC
+/+
GFP/+
GFP/GFP
Number of cells
WBC (10-4)
RBC (10-7)
PLT (10-6)
c
+/+
GFP/GFP
Frequency in BM (%)
Gr1+Mac1+
Ter119+
CD41+
CD3+
CD4+
CD8+
Pre-Pro-B
Pro-B
Pre-B
B220+IgM-
B220+IgM+
d
CLP
CMP
GMP
MEP
e
+/+
GFP/+
GFP/GFP
Frequency in BM (%)
HSC
Frequency in BM (%)
MPP
Frequency in spleen (%)
HSC
f
Percent BrdU (+) cells
HSC
WBM
g
Colony formation by single HSCs
+/+
GFP/GFP
Percent of cells
GM
GEMM
Mk
Overall colony formation efficiency
h
+/+
GFP/+
GFP/GFP
Donor-derived (%)
Myeloid
B
T
Overall
Weeks after transplantation
i
+/+
GFP/GFP
Donor-derived (%)
Myeloid
B
T
Overall
Weeks after transplantation

Figure 2. *α-catulin*$^{GFP/GFP}$ mice had normal hematopoiesis, normal HSC frequency, and normal HSC function. a, Hindlimb bone marrow cellularity (n=4-9 mice/genotype) and spleen cellularity (n=4-6 mice/genotype), spleen mass (n=4-7 mice/genotype). **b,** White blood cell (WBC), red blood cell (RBC) and platelet (PLT) counts per microliter of peripheral blood from 8-12 week old *α-catulin*$^{+/+}$, *α-catulin*$^{GFP/+}$, and *α-catulin*$^{GFP/GFP}$ mice (n=9 mice/genotype). **c**,d, Frequencies of mature hematopoietic cells and progenitors in the bone marrow of 8-12 week old *α-catulin*$^{+/+}$ and *α-catulin*$^{GFP/GFP}$ mice (Pre-ProB cells were B220^{+}sIgM^{-}CD43^{+}CD24^{-} ; ProB cells were B220^{+}sIgM^{-}CD43^{+}CD24^{+}; Pre-B cells were B220^{+}sIgM^{-}CD43^{-}; common lymphoid progenitors (CLPs) were Lin^{-}c-kit^{low}Sca1^{low}CD127^{+}CD135^{+}; common myeloid progenitors (CMPs) were Lin^{-}c-kit^{+}Sca1^{-}CD34^{+}CD16/32^{-}; granulocyte-macrophage progenitors (GMPs) were Lin^{-}c-kit^{+}Sca1^{-}CD34^{+}CD16/32^{+}; and megakaryocyte-erythroid progenitors (MEPs) were Lin^{-}c-kit^{+}Sca1^{-}CD34^{-} CD16/32^{-} (n=3 mice/genotype). **e,** Bone marrow CD150^{+}CD48^{-}LSKs HSC frequency, bone marrow CD150^{-}CD48^{-}LSKs MPP frequency (n=12 mice/genotype in 12 independent experiments), and spleen HSC frequency (n=3 mice/genotype in 3 experiments). **f,** Percentage of HSCs and whole bone marrow cells that incorporated a 3 day pulse of BrdU *in vivo* (n=6 *α-catulin*$^{+/+}$, 9 *α-catulin*$^{GFP/+}$, and 7 *α-catulin*$^{GFP/GFP}$ 8-12 week old mice in 3 independent experiments). **g,** Colony formation by HSCs in methylcellulose cultures (GM means granulocyte-macrophage colonies, GEMM means granulocyte-erythroid-macrophage-megakaryocyte colonies, Mk means megakaryocyte colonies; (n=5 mice/genotype in 5 independent experiments). **h,**

Reconstitution of irradiated mice by 300,000 donor bone marrow cells from 8-12 week old *α-catulin*$^{+/+}$, *α-catulin*$^{GFP/+}$, or *α-catulin*$^{GFP/GFP}$ mice competed against 300,000 recipient bone marrow cells (n=4 donor mice and 16 recipient mice for *α-catulin*$^{+/+}$, n=3 donor mice and 9 recipient mice for *α-catulin*$^{GFP/+}$, and n=4 donor mice and 18 recipients for *α-catulin*$^{GFP/GFP}$ in 3 independent experiments). **i,** Serial transplantation of 3 million WBM cells from primary recipient mice shown in panel d into irradiated secondary recipient mice (n=4 primary *α-catulin*$^{+/+}$ recipients were transplanted into 17 secondary recipients and n=6 primary *α-catulin*$^{GFP/GFP}$ recipients were transplanted into 20 secondary recipients). All data represent mean±s.d. The statistical significance of differences between genotypes was assessed using Student's *t*-tests or ANOVAs. None were significant.

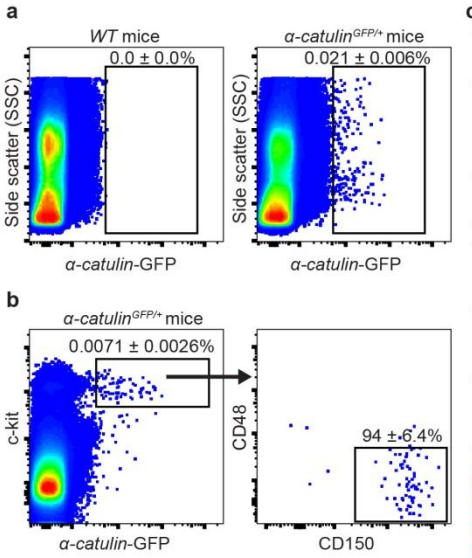

c

Donor cell population	Donor cell dose	LTMR mice	HSC frequency
Unfractionated bone marrow	25,000 50,000 100,000 300,000	19/27 15/25 21/23 14/14	1/37,000
α-catulin-GFP$^+$	1 5	2/13 13/25	1/6.7
α-catulin-GFP$^-$	300,000	2/20	1/2,847,000
α-catulin-GFP$^+$ c-kit$^+$	1 5 30	9/34 17/23 14/14	1/3.5
α-catulin-GFP$^-$ CD150$^+$CD48$^-$ Lin$^-$c-kit$^+$Sca1$^+$	5	2/44	1/110
α-catulin-GFP$^+$ CD150$^+$CD48$^-$ Lin$^-$c-kit$^+$Sca1$^+$	5	24/30	1/3.1

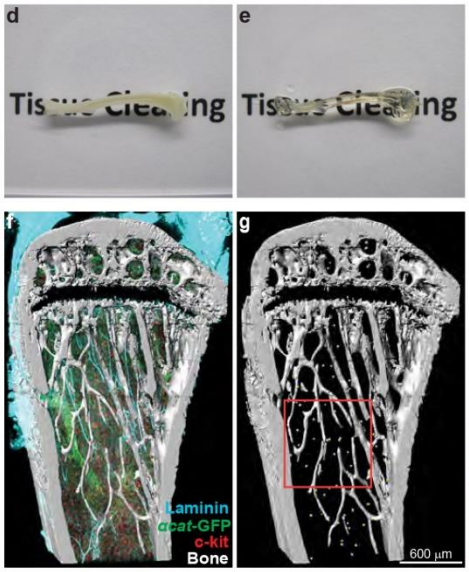

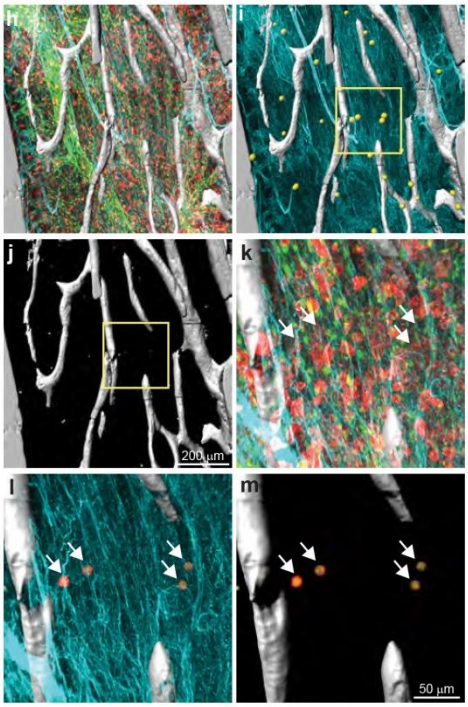

Figure 3. Deep imaging of *α-catulin*-GFP$^+$ HSCs in digitally reconstructed bone marrow. **a,** Only 0.021±0.006% of *α-catulin*$^{GFP/+}$ bone marrow cells were GFP$^+$ (n=14 mice in 11 independent experiments). **b,** Nearly all *α-catulin*-GFP$^+$c-kit$^+$ bone marrow cells were CD150$^+$CD48$^-$ (n=9 mice in 3 independent experiments Figure 4b shows ungated cells from this analysis; Figure 17 shows scatter profiles). **c,** Competitive reconstitution assays in irradiated mice showed *α-catulin*-GFP$^+$ cells were highly enriched for long-term multilineage reconstituting HSCs. Donor cells were competed against 300,000 recipient WBM cells. HSC frequency was calculated using Extreme Limiting Dilution Analysis(Hu and Smyth, 2009) software (http://bioinf.wehi.edu.au/software/elda/) (2-4 independent experiments per cell population). **d-e,** A half tibia before (d) and after clearing (e). **f-m,** Deep imaging of *α-catulin*-GFP$^+$c-kit$^+$ HSCs in the epiphysis and metaphysis of a half tibia (360 μm thick) showing digital bone surfaces (based on second harmonic generation, white), as well as blood vessels (laminin, blue), hematopoietic progenitors (c-kit$^+$, red), and *α-catulin*-GFP$^+$ cells (green). Endothelial cells also express *α-catulin*-GFP but were easily distinguished from *α-catulin*-GFP$^+$c-kit$^+$ HSCs based on c-kit expression and morphology. Note that in 2 dimensional projected images of thick specimens, *α-catulin*-GFP$^+$ cells and c-kit+ cells can appear much more frequent than they actually are because all of the cells from the thick specimens are collapsed into a single 2 dimensional optical plane. **g**) Same as (**f**), digitally masked to reveal only HSCs and bone. The positions of the *α-catulin*-GFP$^+$c-kit$^+$ HSCs are represented by yellow spheres to make them visible at this magnification. **h-j**) A higher magnification view

of the boxed region from panel g. Panel **i** digitally masks all hematopoietic cells other than HSCs (yellow spheres). Panel **j** digitally masks blood vessels and hematopoietic cells other than HSCs. **k-m**) A higher magnification view of the boxed area from panel j. Panel **l** digitally masks all hematopoietic cells other than HSCs (arrows). Panel **m** additionally masks blood vessels. Images are representative of three independent experiments. Supplementary video 1 shows a three dimensional digital reconstruction of bone and bone marrow. The relative positions of HSCs and other bone marrow structures can appear to change slightly in thick specimens when magnification is changed due to the rendering perspective for 3 dimensional display of volume data.

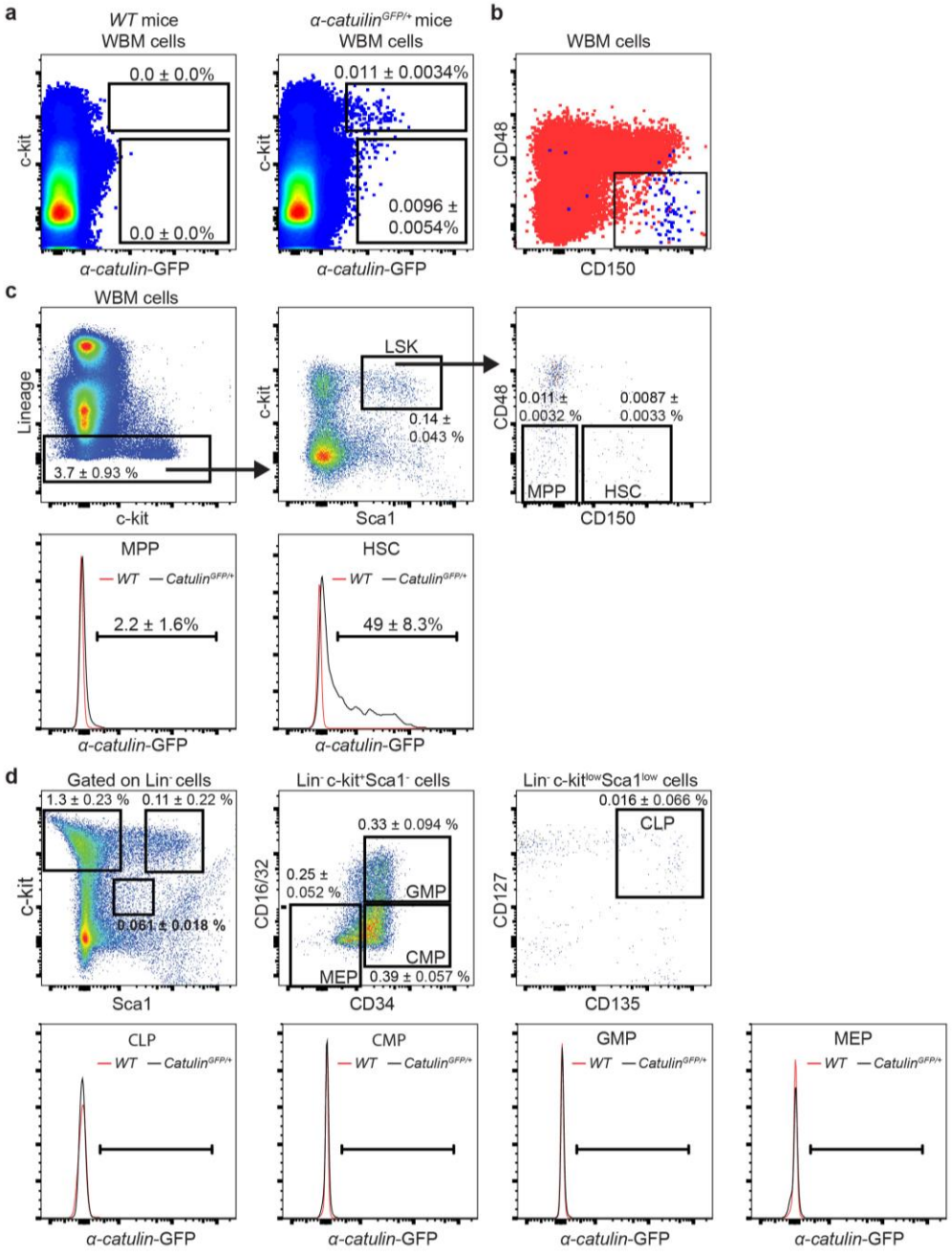
a
WT mice
WBM cells
0.0 ± 0.0%
0.0 ± 0.0%
c-kit
α-catulin-GFP
α-catuilinGFP/+ mice
WBM cells
0.011 ± 0.0034%
0.0096 ± 0.0054%
c-kit
α-catulin-GFP
b
WBM cells
CD48
CD150
c
WBM cells
Lineage
3.7 ± 0.93 %
c-kit
c-kit
LSK
0.14 ± 0.043 %
Sca1
CD48
0.011 ± 0.0032 %
0.0087 ± 0.0033 %
MPP
HSC
CD150
MPP
WT CatulinGFP/+
2.2 ± 1.6%
α-catulin-GFP
HSC
WT CatulinGFP/+
49 ± 8.3%
α-catulin-GFP
d
Gated on Lin- cells
1.3 ± 0.23 %
0.11 ± 0.22 %
0.061 ± 0.018 %
c-kit
Sca1
Lin- c-kit+Sca1- cells
0.33 ± 0.094 %
0.25 ± 0.052 %
GMP
CMP
MEP
0.39 ± 0.057 %
CD16/32
CD34
Lin- c-kitlowSca1low cells
0.016 ± 0.066 %
CLP
CD127
CD135
CLP
WT CatulinGFP/+
α-catulin-GFP
CMP
WT CatulinGFP/+
α-catulin-GFP
GMP
WT CatulinGFP/+
α-catulin-GFP
MEP
WT CatulinGFP/+
α-catulin-GFP

Figure 4. *α-catulin*-GFP expression among hematopoietic cells is highly restricted to HSCs. a, The frequency of *α-catulin*-GFP^{+} bone marrow cells in negative control *α-catulin*$^{+/+}$ (WT) mice and *α-catulin*$^{GFP/+}$ mice (n=14 mice per genotype in 11 independent experiments). In all cases in this figure percentages refer to the frequency of each population as a percentage of WBM cells. **b**, *α-catulin*-GFP^{+}ckit^{+} cells from Figure 1b are shown (blue dots) along with all other bone marrow cells in the same sample (red dots). **c,** CD150^{+}CD48^{-}LSK HSCs express *α-catulin*-GFP but CD150^{-}CD48^{-}LSK MPPs do not (n=17 mice in 12 independent experiments). A minority of the *α-catulin*-GFP^{+}ckit^{+} cells had high forward scatter, lacked reconstituting potential, and were gated out when flow cytometrically isolating HSCs and when identifying HSCs during imaging (see Figure 17 for further explanation). **d,** , Lin^{-}c-kit^{low}Sca1^{low}CD127^{+}CD135^{+} common lymphoid progenitors (CLPs), Lin^{-}c-kit^{+}Sca1^{-}CD34^{+}CD16/32^{-} cells common myeloid progenitors (CMPs), Lin^{-}c-kit^{+}Sca1^{-}CD34^{+}CD16/32^{+} granulocyte-macrophage progenitors (GMPs), and Lin^{-}c-kit^{+}Sca1^{-}CD34^{-}CD16/32^{-} megakaryocyte-erythroid progenitors (MEPs) did not express *α-catulin*-GFP. *α-catulin*$^{GFP/+}$ and control cell populations had similar levels of background GFP signals that accounted for fewer than 1% of the cells in each population (n=9 mice/genotype in 2 independent experiments).

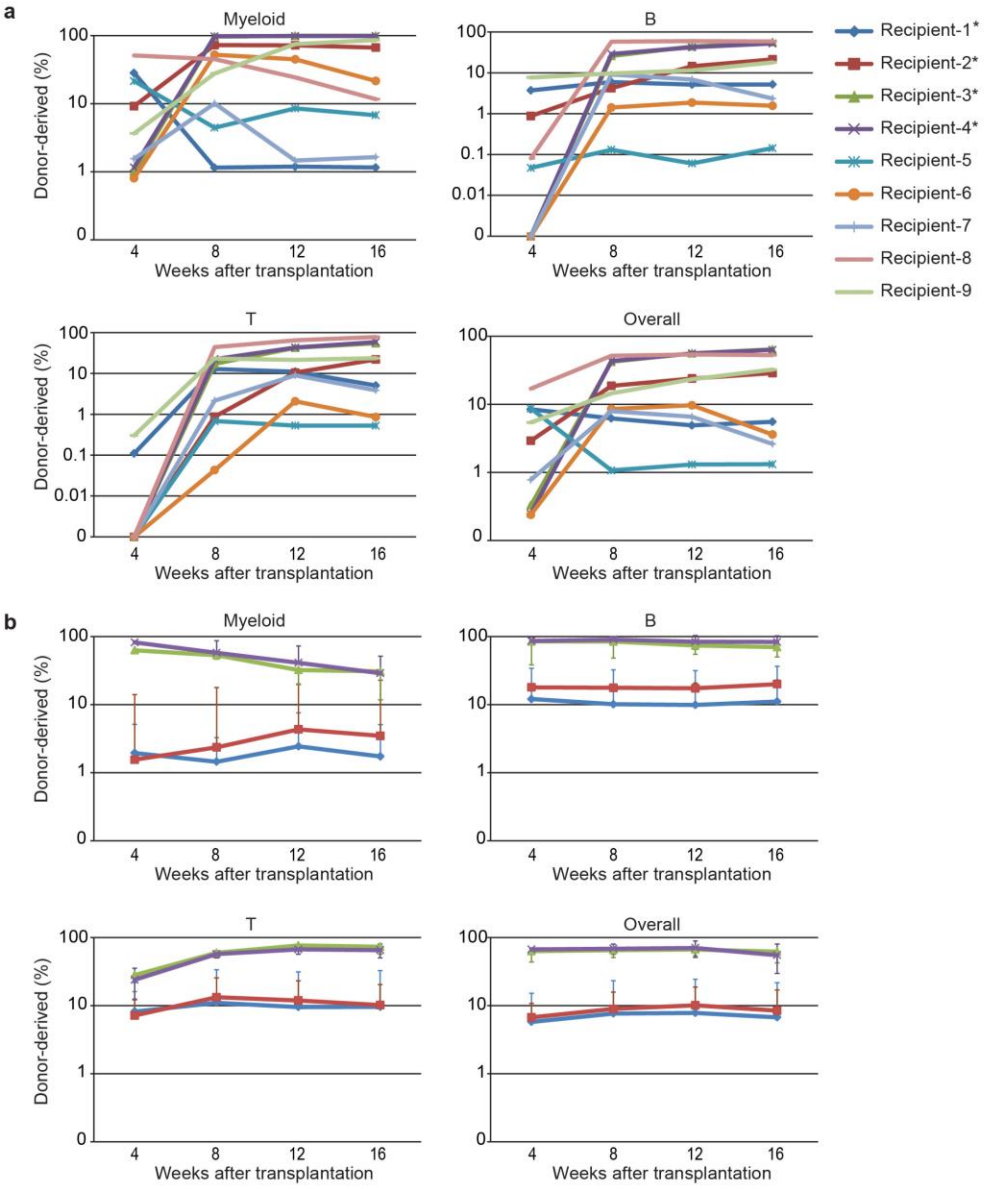
a
Myeloid
B
T
Overall
Donor-derived (%)
Weeks after transplantation
Recipient-1*
Recipient-2*
Recipient-3*
Recipient-4*
Recipient-5
Recipient-6
Recipient-7
Recipient-8
Recipient-9
b
Myeloid
B
T
Overall
Donor-derived (%)
Weeks after transplantation

Figure 5. *α-catulin*-GFP$^+$ckit$^+$ bone marrow cells are highly enriched for HSC activity. a, Competitive reconstitution assays in which one donor *α-catulin*-GFP$^+$ckit$^+$GFP$^+$ bone marrow cell was transplanted along with 300,000 recipient bone marrow cells into irradiated recipient mice. Each line represents one of the nine mice (out of 34 transplanted; see Figure 1c) that were long-term multilineage reconstituted by donor cells. **b**, Three million WBM cells from primary recipient mice 1-4 from panel a (indicated by an asterisk) were transplanted into secondary recipient mice (3-5 secondary recipients/primary recipient for a total of 17 secondary recipient). The average (±s.d.) levels of donor cell reconstitution in secondary recipient mice from each primary donor are shown.

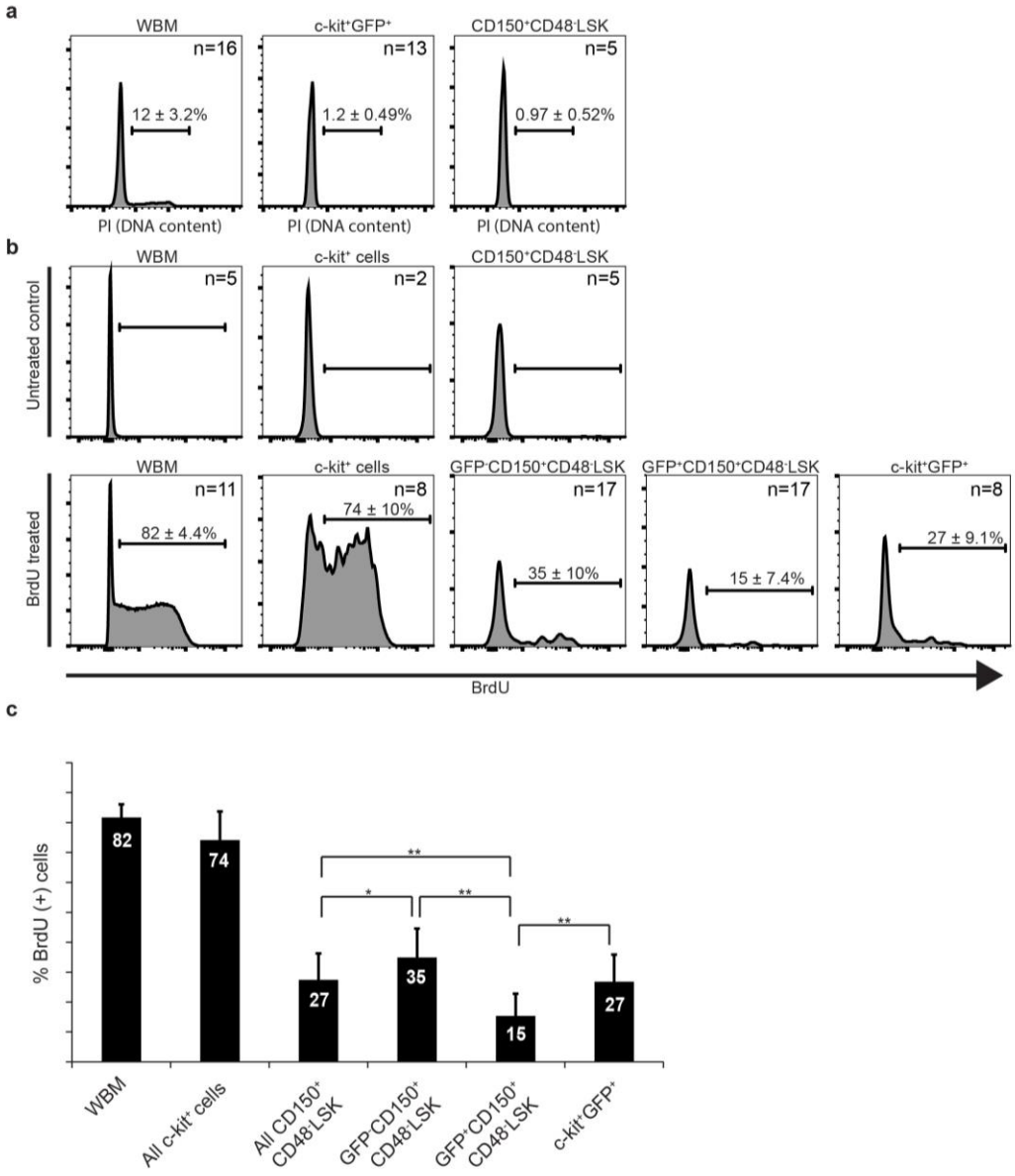
a
WBM
n=16
12 ± 3.2%
c-kit+GFP+
n=13
1.2 ± 0.49%
CD150+CD48-LSK
n=5
0.97 ± 0.52%
PI (DNA content)
PI (DNA content)
PI (DNA content)
b
WBM
c-kit+ cells
CD150+CD48-LSK
Untreated control
n=5
n=2
n=5
WBM
c-kit+ cells
GFP-CD150+CD48-LSK
GFP+CD150+CD48-LSK
c-kit+GFP+
BrdU treated
n=11
82 ± 4.4%
n=8
74 ± 10%
n=17
35 ± 10%
n=17
15 ± 7.4%
n=8
27 ± 9.1%
BrdU
c
% BrdU (+) cells
82
74
27
35
15
27
**
*
**
**
WBM
All c-kit+ cells
All CD150+ CD48-LSK
GFP-CD150+ CD48-LSK
GFP+CD150+ CD48-LSK
c-kit+GFP+

Figure 6. *α-catulin*-GFP$^+$ckit$^+$ HSCs are quiescent. a, DNA content of WBM cells, *α-catulin*-GFP$^+$ckit$^+$ HSCs, and CD150$^+$CD48$^-$LSK HSCs. While 11.5% of WBM cells had greater than 2N DNA content (in S/G2/M phases of the cell cycle), only around 1% of *α-catulin*-GFP$^+$ckit$^+$ HSCs or CD150$^+$CD48$^-$LSK HSCs had greater than 2N DNA content. **b**, BrdU incorporation into WBM cells, c-kit$^+$ cells, *α-catulin*-GFP$^-$ CD150$^+$CD48$^-$LSK cells, *α-catulin*-GFP$^+$CD150$^+$CD48$^-$LSK HSCs, and *α-catulin*-GFP$^+$ckit$^+$ HSCs after 3 days of continuous BrdU administration (BrdU treated). Untreated negative control mice are also shown. **c,** Percentage of BrdU$^+$ cells in each cell population. In each panel, the number of mice from which each cell population was isolated for analysis (without being pooled) is indicated. All data reflect mean±s.d. from 2 to 5 independent experiments. Statistical significance was assessed using Students t-tests (*, $P<0.05$; **, $P<0.01$).

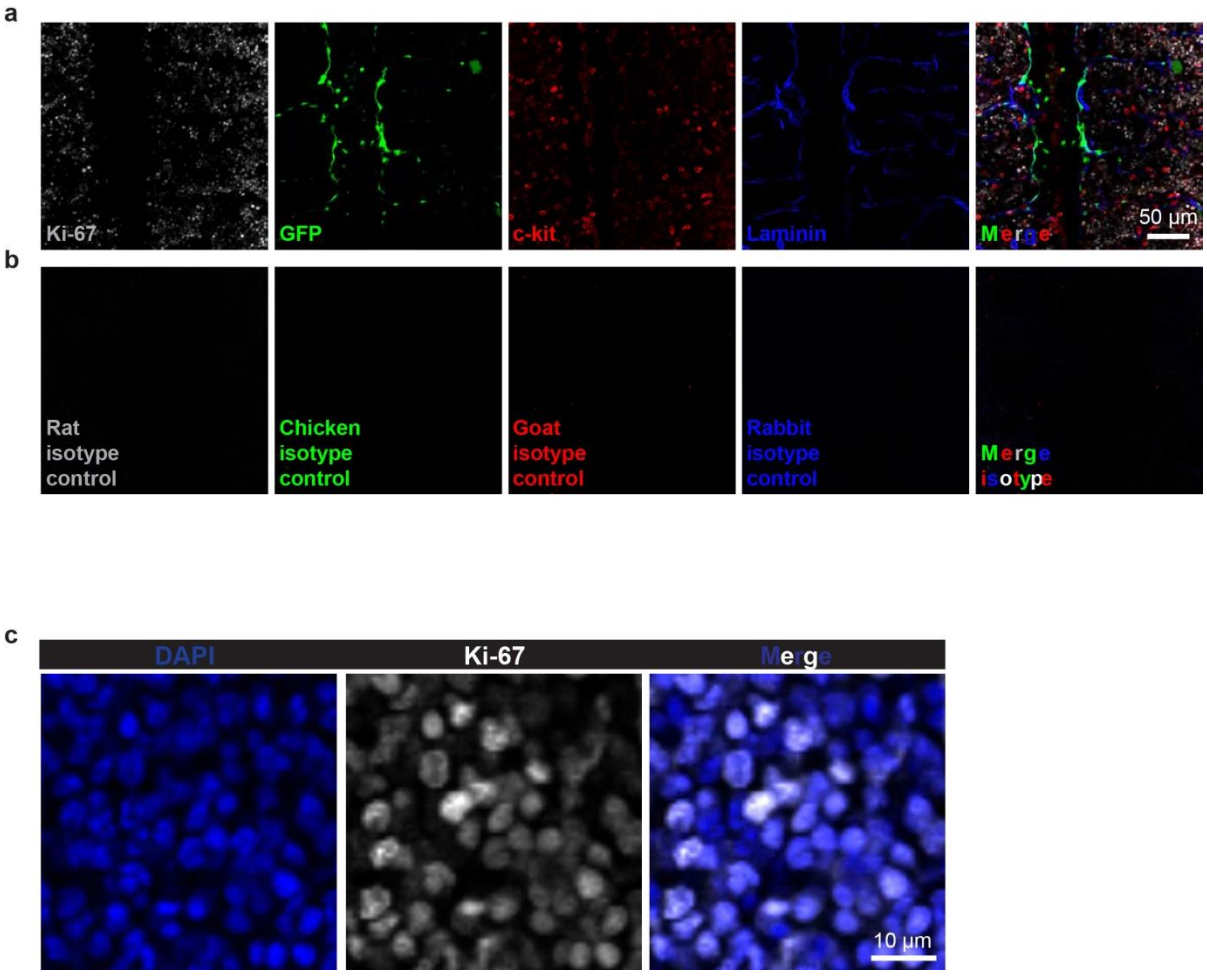

Figure 7. c-kit and *α-Catulin*-GFP staining do not reflect autofluorescence or background staining. **a,** 4-color confocal analysis of a bone marrow plug from a tibia diaphysis stained with primary and secondary antibodies against Ki-67, *α-catulin*-GFP, c-kit, and laminin. A 2 µm optical section is shown from a thick specimen to illustrate typical staining. **b**, Negative control in which a bone marrow plug from a tibia diaphysis was stained with isotype control and secondary antibodies then imaged under the same conditions as shown in panel a. c, Ki-67 staining was largely or exclusively nuclear, co-localizing with DAPI.

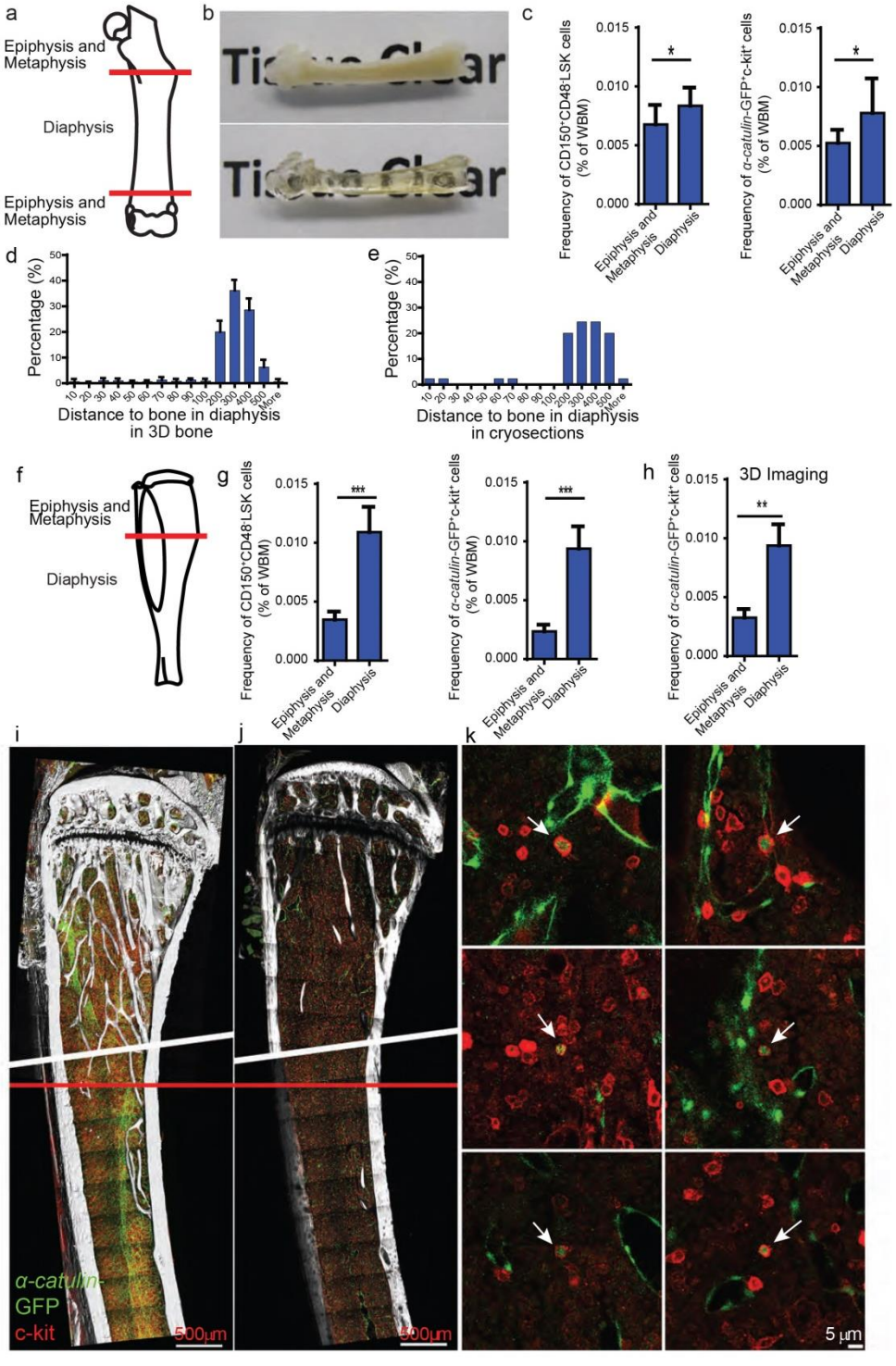
a
Epiphysis and Metaphysis
Diaphysis
Epiphysis and Metaphysis
b
c
Frequency of CD150+CD48-LSK cells (% of WBM)
Frequency of α-catulin-GFP+c-kit+ cells (% of WBM)
Epiphysis and Metaphysis
Diaphysis
d
Percentage (%)
Distance to bone in diaphysis in 3D bone
e
Percentage (%)
Distance to bone in diaphysis in cryosections
f
Epiphysis and Metaphysis
Diaphysis
g
h
3D Imaging
i
j
k
α-catulin-GFP
c-kit
500μm
500μm
5 μm

Figure 8. HSC density is higher in the diaphysis as compared to the metaphysis. a, Schematic of a femur showing the separation of epiphysis/metaphysis from diaphysis. We divided metaphysis from diaphysis at the point where the central sinus branched (see red line in panels a,f and i). This is also the point at which the density of trabecular bone declines moving into the diaphysis. **b,** A bisected femur before and after clearing. **c,** The frequency of $CD150^{+}CD48^{-}$ LSK cells and *α-catulin*-GFP^{+}c-kit^{+} cells by flow cytometry in the epiphysis/metaphysis versus diaphysis (n=9 mice in 2 independent experiments). Note that bone marrow cells were extracted from crushed bones. **d,** The distance from *α-catulin*-GFP^{+}c-kit^{+} cells to the nearest bone surface in the femur diaphysis based on deep imaging (n=368 cells in 3 bisected femurs). **e,** The distance from *α-catulin*-GFP^{+}c-kit^{+} cells to the nearest bone surface in the femur diaphysis based on analysis of thin (7 μm) sections (n=45 cells). **f,** Schematic of a tibia showing the separation of epiphysis/metaphysis from diaphysis (red line). **g,** The frequency of $CD150^{+}CD48^{-}$LSK cells and *α-catulin*-GFP^{+}c-kit^{+} cells by flow cytometry in the epiphysis/metaphysis versus diaphysis (n=9 mice in 2 independent experiments). **h,** The frequency of *α-catulin*-GFP^{+}c-kit^{+} cells in the tibia epiphysis/metaphysis versus diaphysis based on deep confocal imaging (n=3 bisected tibias in 3 independent experiments). **i,** Deep imaging of a bisected tibia showing the separation of metaphysis and diaphysis (red line) where the central sinus branches . Note that these tibias were digitally reconstructed from two different imaging sessions, above and below the diagonal white line. This image shows a 349 μm thick specimen

collapsed into 2 dimensions. Note that this causes *α-catulin*-GFP^{+} cells and c-kit+ cells to appear much more frequent than they actually were because all of the cells from the thick specimen were collapsed into a single 2 dimensional optical plane for presentation. **j**, For comparison purposes, a single 2 µm thick optical slice from the tibia in panel **i**. **k**, High magnification images of single *α-catulin*-GFP^{+}c-kit^{+} cells from the same tibia**.** Note that *α-Catulin*-GFP is also expressed by sinusoidal endothelial cells but these cells are easily distinguished from HSCs because the endothelial cells lack c-kit expression and have a very different morphology. Statistical significance was assessed using Students t-tests (*, $P<0.05$; ** $P<0.01$; ***, $P<0.001$).

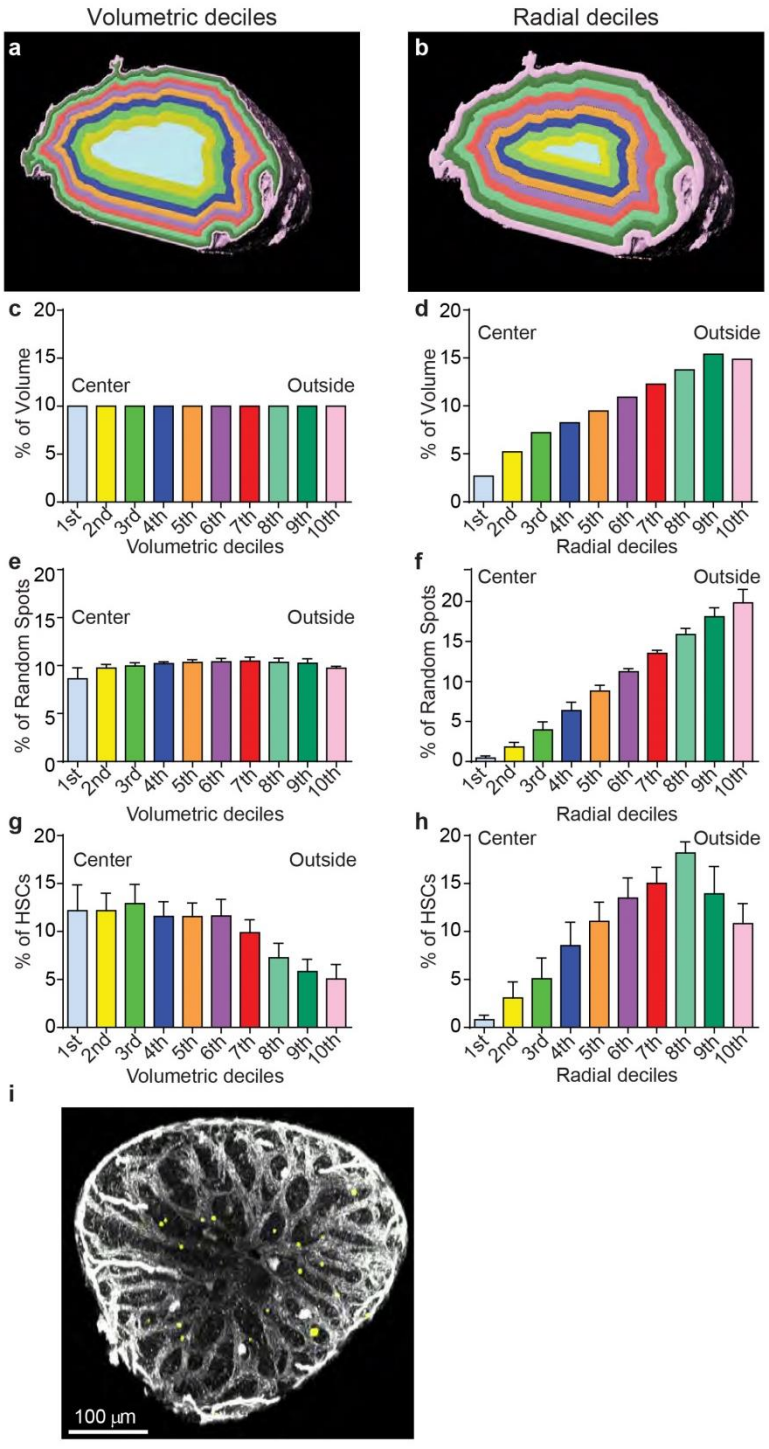
Volumetric deciles
Radial deciles
a
b
c
% of Volume
Center
Outside
Volumetric deciles
d
% of Volume
Center
Outside
Radial deciles
e
% of Random Spots
Center
Outside
Volumetric deciles
f
% of Random Spots
Center
Outside
Radial deciles
g
% of HSCs
Center
Outside
Volumetric deciles
h
% of HSCs
Center
Outside
Radial deciles
i
100 μm

Figure 9. HSCs are enriched in the central marrow and depleted near the endosteum. a,b, The distribution of HSCs from the central marrow to the endosteum can be determined by drawing concentric cylinders that correspond to equal volumetric deciles from the center of the marrow to the endosteum (a) or to equal radial deciles from the center to the endosteum (b) as in a recent study(Kunisaki et al., 2013). **c,d**, Each volumetric decile (as in a) contains 10% of the marrow volume (c). However, cylinders based on radial deciles (as in b), contain successively larger volumes of marrow as they approach the endosteum because the radius of the cylinders becomes larger (d). **e,f**, The distribution of random spots among volumetric deciles (a) is nearly equal because each cylinder contains an equal marrow volume (e). However, the number of random spots per cylinder based on radial deciles (b) increases from the center to the endosteum as cylinder volume increases (f). **g,** If we plotted our HSC localization data by volumetric deciles (as in Figure 10a), HSC were enriched toward the central marrow. **h,** If we plotted our HSC localization data by radial deciles, the number of HSCs per cylinder increased toward the endosteum as cylinder volume increased, similar to random spots and similar to the data recently published by another group based on radial deciles(Kunisaki et al., 2013). When we plotted the data from the other group based on volumetric deciles (by scaling radial decile data based on the known differences in volume between radial and volumetric deciles, as shown in panel d), then those data also appeared consistent with our conclusion that HSC density is higher in the center of the marrow. **i,** A representative cross sectional image of a tibia diaphysis

plug 49µm thick showing a typical distribution of *α-catulin*-GFP^{+}ckit^{+} cells (yellow). Note that although the *α-catulin*-GFP^{+}ckit^{+} cells are quite uniform in size, they appear to differ in size in this image because some are deeper in the z plane than others.

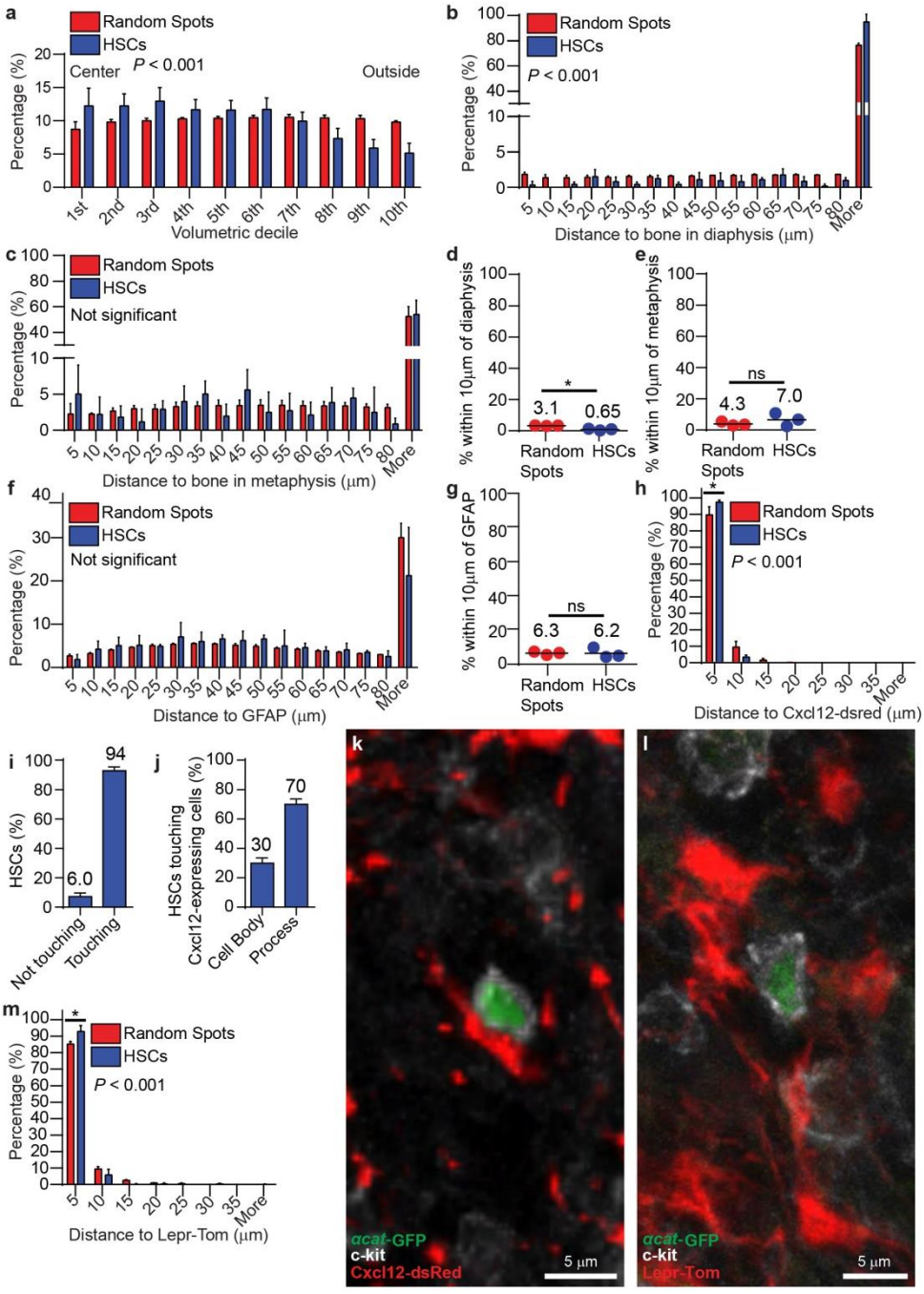
a
Random Spots
HSCs
Center
P < 0.001
Outside
Percentage (%)
Volumetric decile
b
Random Spots
HSCs
P < 0.001
Percentage (%)
Distance to bone in diaphysis (μm)
c
Random Spots
HSCs
Not significant
Percentage (%)
Distance to bone in metaphysis (μm)
d
% within 10μm of diaphysis
3.1
0.65
Random Spots
HSCs
e
% within 10μm of metaphysis
ns
4.3
7.0
Random Spots
HSCs
f
Random Spots
HSCs
Not significant
Percentage (%)
Distance to GFAP (μm)
g
% within 10μm of GFAP
ns
6.3
6.2
Random Spots
HSCs
h
Random Spots
HSCs
P < 0.001
Percentage (%)
Distance to Cxcl12-dsred (μm)
i
HSCs (%)
6.0
94
Not touching
Touching
j
HSCs touching Cxcl12-expressing cells (%)
30
70
Cell Body
Process
m
Random Spots
HSCs
P < 0.001
Percentage (%)
Distance to Lepr-Tom (μm)
k
αcat-GFP
c-kit
Cxcl12-dsRed
5 μm
l
αcat-GFP
c-kit
Lepr-Tom
5 μm

Figure 10. HSCs localize adjacent to Cxcl12^{high} and LepR^{+} niche cells but distant from bone surfaces. a, The distribution of *α-catulin*-GFP^{+}c-kit^{+} HSCs and random spots in concentric cylinders corresponding to equal volumetric deciles from central marrow to endosteal marrow (near the bone surface) from the tibia diaphysis (2977 HSCs in 6 bone marrow plugs (390-550 μm thick) in 6 independent experiments). See Figure 9 for further explanation. Relative to random spots, HSCs were significantly enriched in central marrow. **b,c**, The distance from HSCs or random spots to the nearest bone surface in the diaphysis (**b**) or metaphysis (**c**). HSCs were significantly less enriched than random spots near bone surfaces in the diaphysis (b). **d,e,** Percentages of all HSCs and random spots within 10μm of a bone surface in the diaphysis (**d**) or metaphysis (**e**; **b-e** show 817 HSCs in the diaphysis and 218 HSCs in the metaphysis of 3 bisected tibias that were 360-400 μm thick). **f,** The distance from HSCs or random spots to the nearest GFAP^{+} Schwann cell (n=608 HSCs in bone marrow plugs (430 to 530 μm thick) from the diaphysis of 3 tibias). **g,** Percentages of all HSCs and random spots within 10μm of a GFAP^{+} Schwann cell. **h,** The distance from HSCs or random spots to the nearest Cxcl12^{high} stromal cell (n=596 HSCs in bone marrow plugs (235-450 μm thick) from the diaphysis of 4 tibias). **i-k,** The percentage of HSCs that appear to have cell-cell contact with a Cxcl12^{high} stromal cell (i) and whether the contact is with the cell body or a cellular process (**j**). **k,** An *α-catulin*-GFP^{+}c-kit^{+} cell in apparent contact with a *Cxcl12*-expressing cell. **l,** An *α-catulin*-GFP^{+}c-kit^{+} cell in apparent contact with a *LepR*-expressing cell. **m**, The distance from HSCs or random spots to the nearest

LepR^{+} stromal cell in *LepR^{cre}; tdTomato* (ref (Ding et al., 2012; Zhou et al., 2014)) bone marrow (n=384 HSCs in bone marrow plugs (500 μm thick) from the diaphysis of 3 tibias). All data reflect mean±s.d. from at least three independent experiments. In panels a,b,c,f,h,m the significance of differences in the distribution of HSCs versus random spots was assessed by Kolmogorov–Smirnov analysis. The statistical significance of differences between HSCs and random spots within 5 or 10 microns of a particular stromal cell type (panels d, e, g, h, m) was assessed using Student's t tests (*, P<0.05).

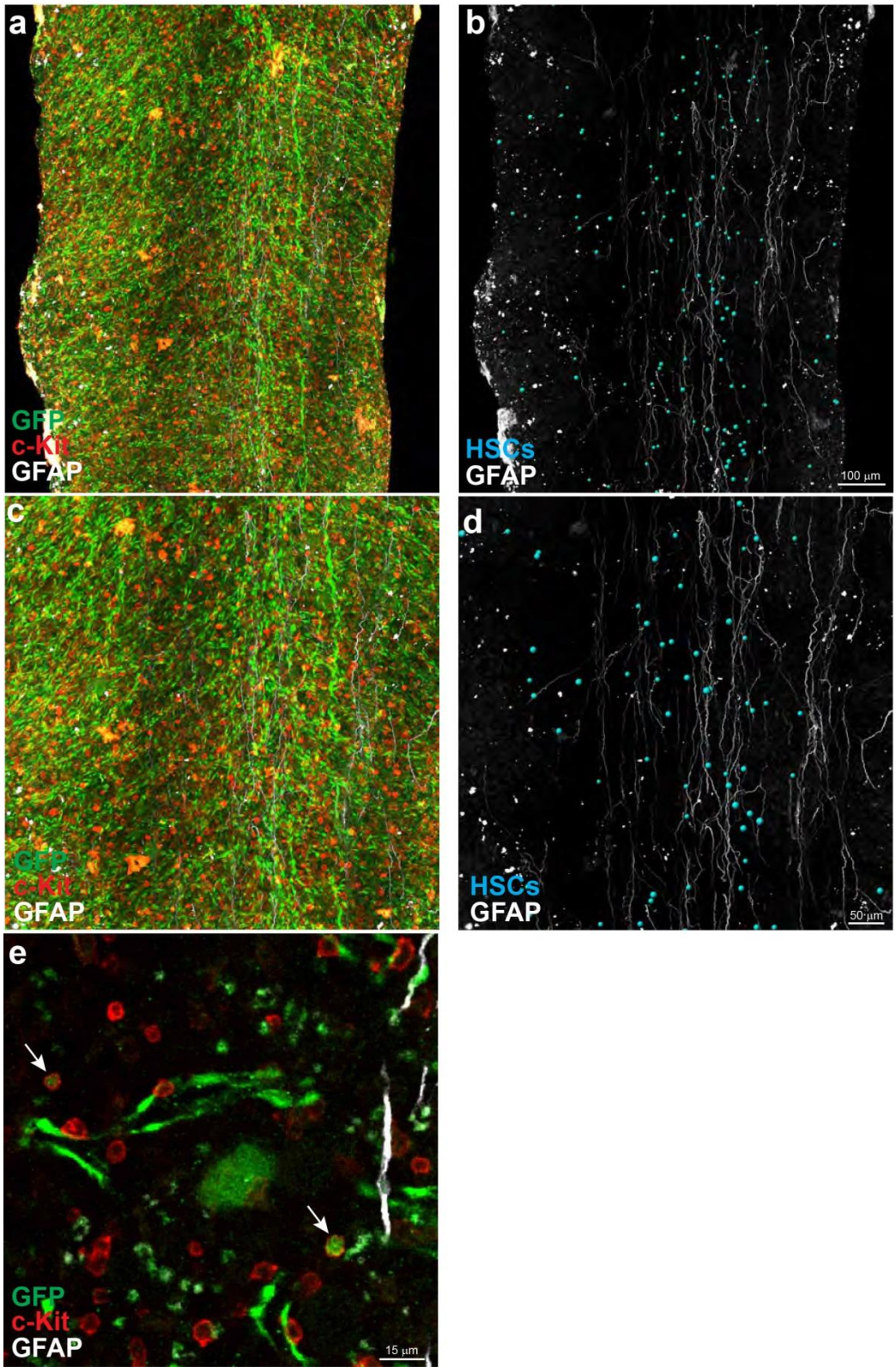
a
GFP
c-Kit
GFAP
b
HSCs
GFAP
100 µm
c
GFP
c-Kit
GFAP
d
HSCs
GFAP
50 µm
e
GFP
c-Kit
GFAP
15 µm

Figure 11. GFAP$^+$ non-myelinating Schwann cells are in the center of the marrow. Low (**a-d**) magnification images of bone marrow plugs from tibia diaphysis stained with antibodies against *α-catulin*-GFP, c-kit, and GFAP. GFAP$^+$ non-myelinating Schwann cells are associated with nerve fibers that run longitudinally along the central bone marrow, where innervated arterioles are located(Kunisaki et al., 2013). *α-catulin*-GFP$^+$c-kit$^+$ cells were identified and annotated with blue spheres using the Imaris spot function in panels **b** and **d**. For clarity, other hematopoietic cells and endothelial cells are not shown in panels **b** and **d**. **e,** A higher magnification image showing two *α-catulin*-GFP$^+$c-kit$^+$ cells (arrows) and their localization relative to GFAP positive glia (white) and *α-catulin*-GFP$^+$ endothelial cells (green). The images in panels a-d show a 505 μm thick specimen. This causes *α-catulin*-GFP$^+$ cells and c-kit+ cells to appear much more frequent than they actually were because all of the cells from the thick specimen were collapsed into a single 2 dimensional optical plane for presentation. Note as well that because these were thick specimens, there were cases in which an *α-catulin*-GFP$^+$ cell and a c-kit$^+$ cell were present in different optical planes such that they appeared to be a single *α-catulin*-GFP$^+$c-kit$^+$ cell when collapsed into a single 2 dimensional image. For this reason, *α-catulin*-GFP$^+$c-kit$^+$ cells cannot be reliably identified in low magnification 2 dimensional projected images. In all cases, cells that we identified as *α-catulin*-GFP$^+$c-kit$^+$ were manually examined at high magnification in 3 dimensions to confirm double labeling of single cells, as shown in panel e.

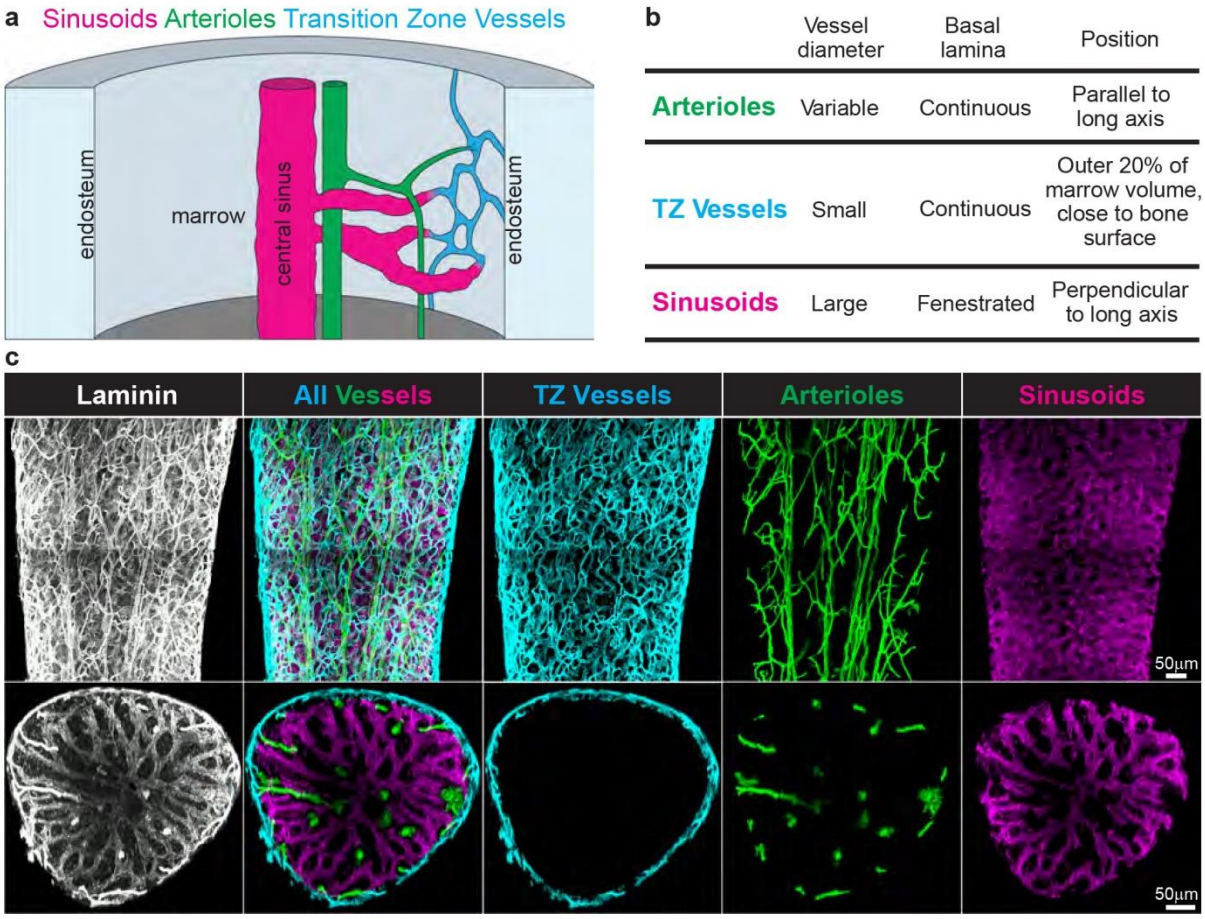

Figure 12. Bone marrow blood vessel types can be distinguished based upon vessel diameter, continuity of basal lamina, morphology, and position. a,b, Schematic (a) and properties (b) of blood vessels in the bone marrow. Blood enters the marrow through arterioles that branch as they become smaller in diameter and approach the endosteum, where they connect to smaller diameter transition zone capillaries near the bone surface. These transition zone capillaries connect to the large diameter sinusoids that feed blood into the central sinuous through which it leaves the bone marrow in venous circulation. **c**, Each type of blood vessel was distinguished based on vessel diameter, continuity of basal lamina, morphology, and

position then color coded using published criteria(Draenert and Draenert, 1980; Kopp et al., 2009; Li et al., 2009; Nombela-Arrieta et al., 2013). To create distinct digital surfaces associated with each type of blood vessel we first designated all laminin-stained blood vessels in the outer 20% of the marrow volume (adjacent to the endosteum) as transition zone vessels (blue). Arterioles were identified and manually traced in the remaining 80% of marrow volume based on high intensity laminin staining, continuous basal lamina, and morphology. Remaining blood vessels with low intensity laminin staining, fenestrated basal lamina, large diameter, and sinusoidal morphology were designated sinusoids. Note that this cross-sectional image is also shown in Figue 2.9i to illustrate a typical distribution of *α-catulin*-GFP^{+}c-kit^{+} cells. The longitudinal images (top) show bone marrow plugs that were 150 µm thick and the cross-sectional images (bottom) were 49 µm thick.

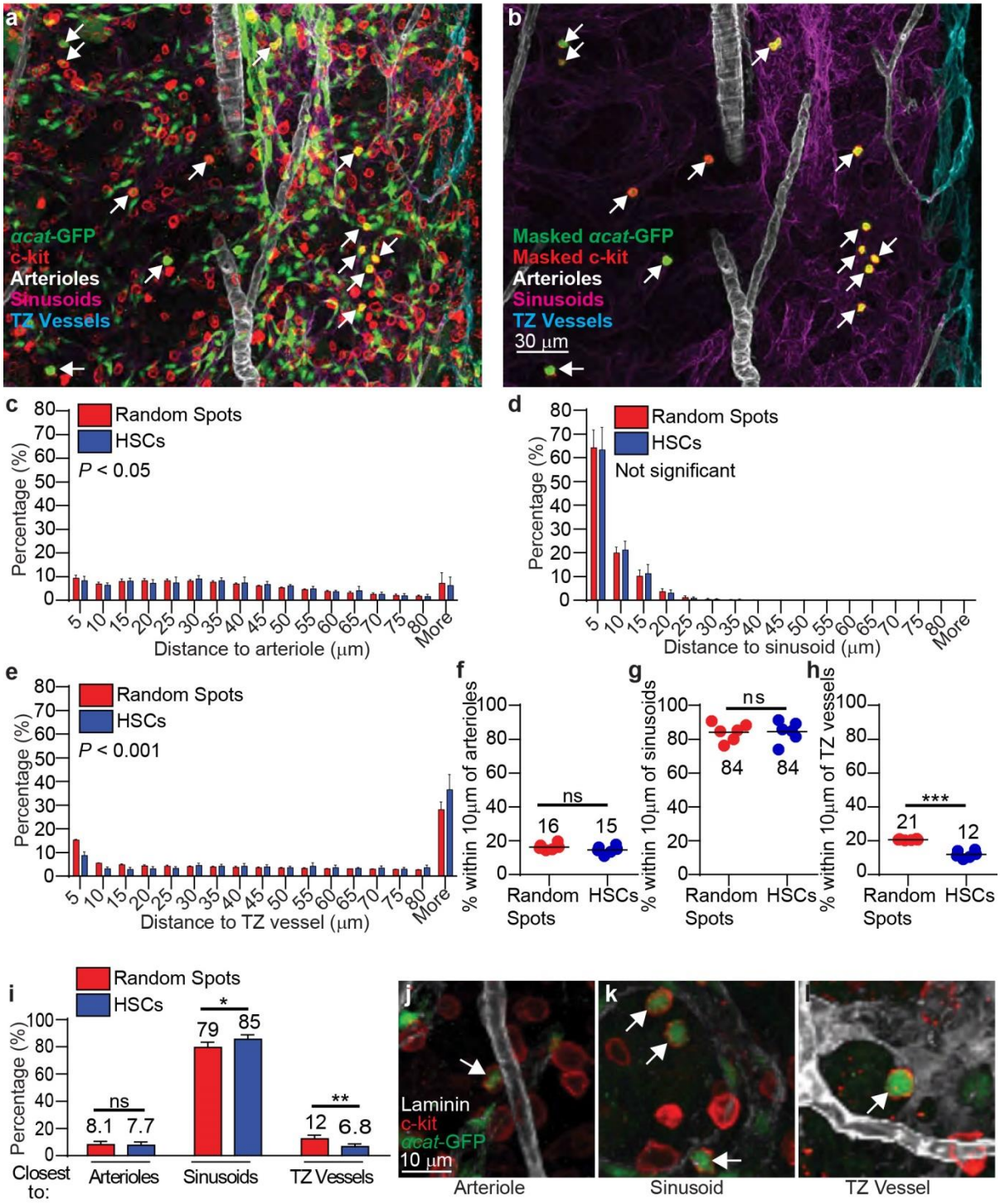
a
αcat-GFP
c-kit
Arterioles
Sinusoids
TZ Vessels
b
Masked αcat-GFP
Masked c-kit
Arterioles
Sinusoids
TZ Vessels
30 μm
c
Random Spots
HSCs
P < 0.05
Percentage (%)
Distance to arteriole (μm)
d
Random Spots
HSCs
Not significant
Percentage (%)
Distance to sinusoid (μm)
e
Random Spots
HSCs
P < 0.001
Percentage (%)
Distance to TZ vessel (μm)
f
% within 10μm of arterioles
ns
16
15
Random Spots
HSCs
g
% within 10μm of sinusoids
ns
84
84
Random Spots
HSCs
h
% within 10μm of TZ vessels
***
21
12
Random Spots
HSCs
i
Random Spots
HSCs
Percentage (%)
ns
8.1
7.7
*
79
85
**
12
6.8
Closest to:
Arterioles
Sinusoids
TZ Vessels
j
Laminin
c-kit
αcat-GFP
10 μm
Arteriole
k
Sinusoid
l
TZ Vessel

Figure 13. HSCs localize adjacent to sinusoids but distant from arterioles and transition zone vessels in tibias. a,b, The position of *α-catulin*-GFP^{+}c-kit^{+} HSCs (arrows) relative to sinusoids (purple), arterioles (white), and transition zone vessels (blue). Vessels were categorized and false colored based on morphology, position, and laminin staining as detailed in Figure 12. Hematopoietic cells other than HSCs were masked in panel b for clarity**. c-e,** The distance from HSCs or random spots to the nearest arteriole (**c**), sinusoid (**d**), or transition zone vessel (**e**). **f-i,** Percentages of all HSCs and random spots within 10μm of an arteriole (**f**), a sinusoid (**g**), or a transition zone vessel (**h**). **i,** Percentages of HSCs and random spots that were closest to arterioles, sinusoids, or transition zone vessels. **j-l**, Representative images of *α-catulin*-GFP^{+}c-kit^{+} HSCs (arrows) that localized immediately adjacent to an arteriole (**j**), a sinusoid (**k**), or a transition zone vessel (**l**). All data reflect mean±s.d. from bone marrow plugs (390-550 μm thick) from the diaphysis of 6 tibias in which a total of 2977 HSCs were analyzed in 6 independent experiments. In panels c-e the statistical significance of differences in the distribution of HSCs versus random spots was assessed by Kolmogorov–Smirnov analysis. Statistical significance in panels f-i was assessed by Student's t-tests (*, $P<0.05$; **, $P<0.01$; ***, $P<0.001$).

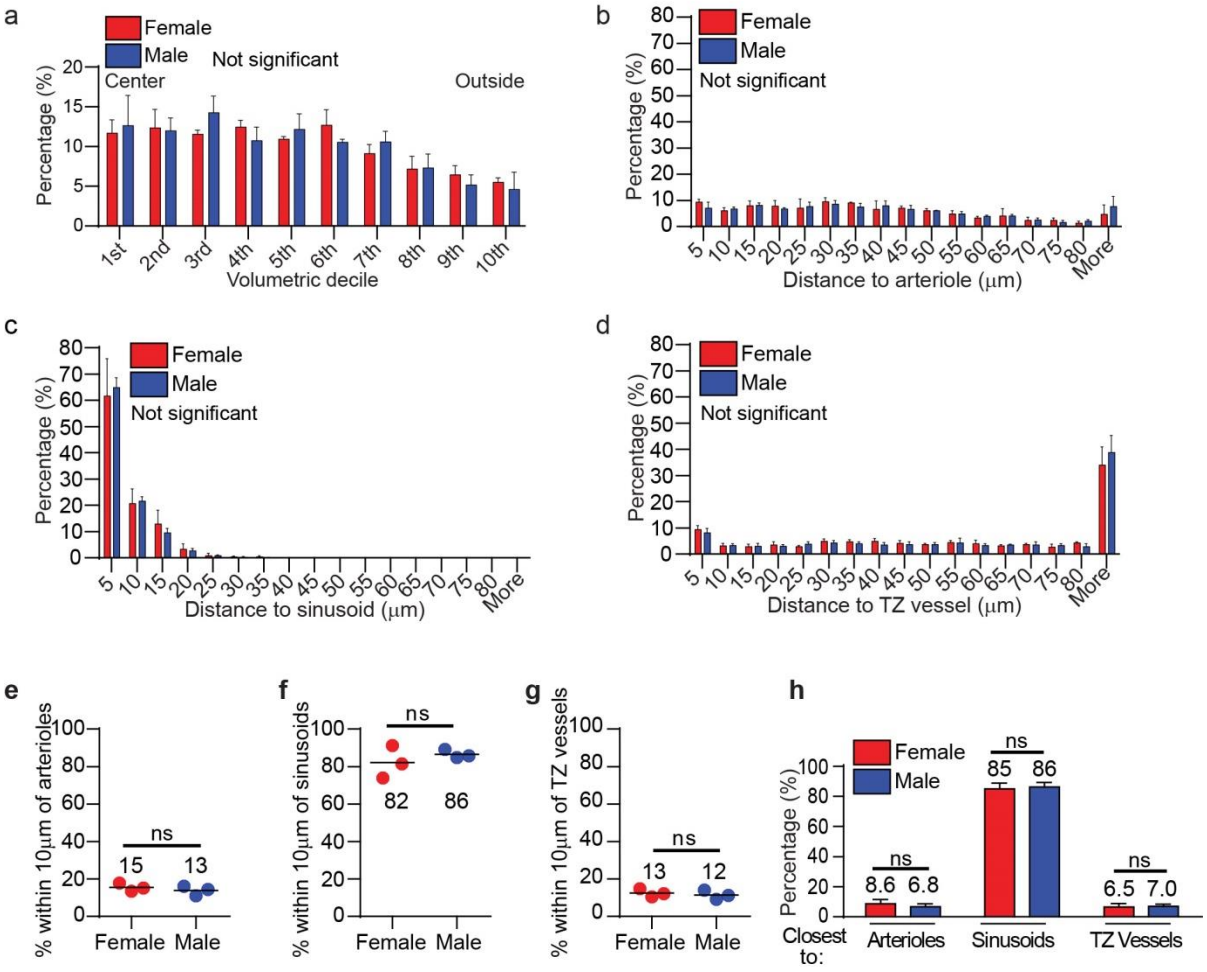

Figure 14. We could not detect any difference in the distribution of HSCs in the bone marrow of male and female mice. a, The distribution of *α-catulin*-GFP^{+}c-kit^{+} cells in concentric cylinders corresponding to equal volumetric deciles from central marrow to endosteal marrow (near the bone surface) in bone marrow plugs from the tibia diaphysis of male and female mice. **b,c,d,** The distance from *α-catulin*-GFP^{+}c-kit^{+} cells in male or female mice to the nearest arteriole (b), sinusoid (c), or transition zone vessel (d) in tibia based on deep imaging. **e,f,g,** The percentage of *α-catulin*-GFP^{+}c-kit^{+} cells within 10 μm of arterioles (e), sinusoids (f) and transition zone

vessels (g) in the tibias of male versus female mice. **h,** The percentage of *α-catulin*-GFP^{+}c-kit^{+} cells closest to arterioles, sinusoids, or transition zone vessels in the tibias of male versus female mice. These data show mean±s.d. for a total of 1345 *α-catulin*-GFP^{+}c-kit^{+} cells from 3 female tibias and 1632 *α-catulin*-GFP^{+}c-kit^{+} cells from 3 male tibias. The statistical significance of differences were assessed using Kolmogorov–Smirnov tests in panels **a-d** and Student's t tests in panels **e-h**. None of the differences were statistically significant.

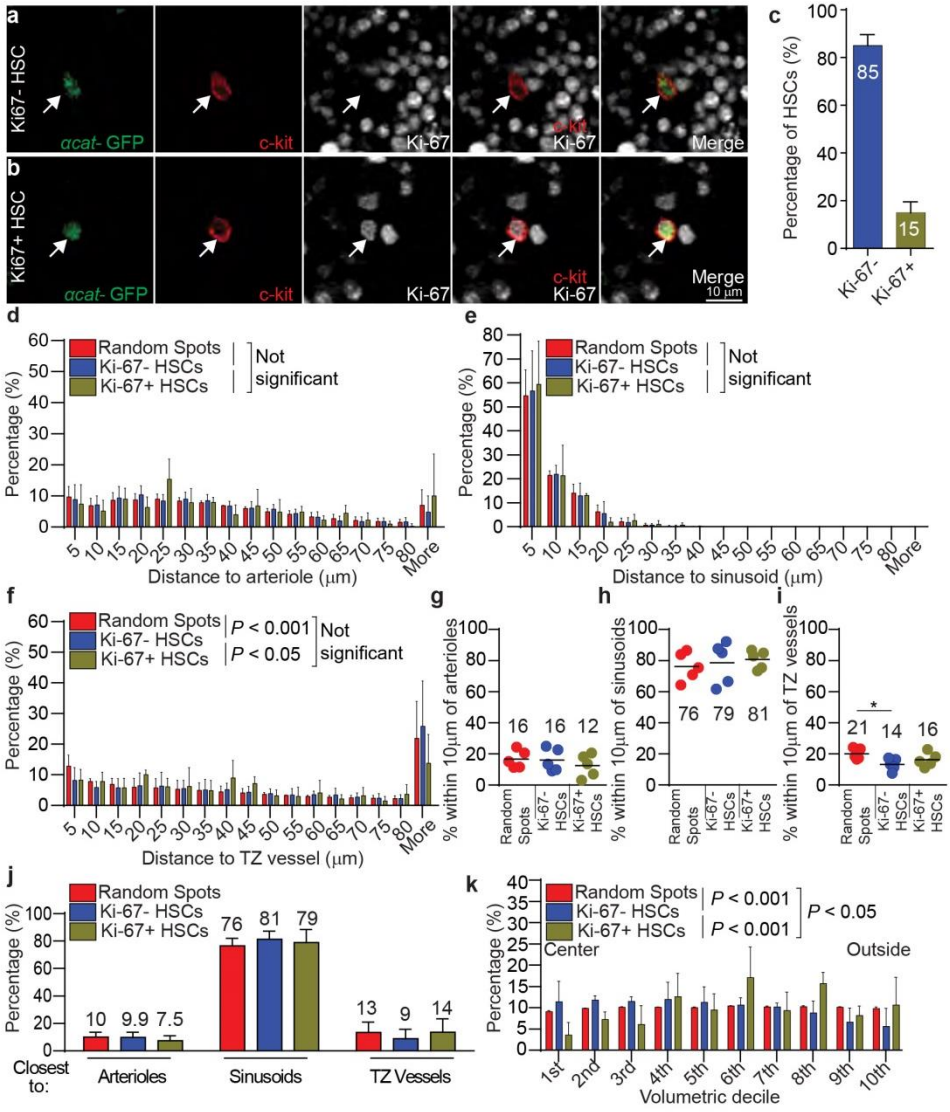
a
Ki67- HSC
αcat- GFP
c-kit
Ki-67
c-kit
Ki-67
Merge
b
Ki67+ HSC
αcat- GFP
c-kit
Ki-67
c-kit
Ki-67
Merge
10 μm
c
Percentage of HSCs (%)
85
15
Ki-67-
Ki-67+
d
Random Spots
Ki-67- HSCs
Ki-67+ HSCs
Not significant
Percentage (%)
Distance to arteriole (μm)
e
Random Spots
Ki-67- HSCs
Ki-67+ HSCs
Not significant
Percentage (%)
Distance to sinusoid (μm)
f
Random Spots
Ki-67- HSCs
Ki-67+ HSCs
P < 0.001
P < 0.05
Not significant
Percentage (%)
Distance to TZ vessel (μm)
g
% within 10μm of arterioles
16
16
12
Random Spots
Ki-67- HSCs
Ki-67+ HSCs
h
% within 10μm of sinusoids
76
79
81
Random Spots
Ki-67- HSCs
Ki-67+ HSCs
i
% within 10μm of TZ vessels
*
21
14
16
Random Spots
Ki-67- HSCs
Ki-67+ HSCs
j
Random Spots
Ki-67- HSCs
Ki-67+ HSCs
Percentage (%)
10
9.9
7.5
76
81
79
13
9
14
Closest to:
Arterioles
Sinusoids
TZ Vessels
k
Random Spots
Ki-67- HSCs
Ki-67+ HSCs
P < 0.001
P < 0.001
P < 0.05
Center
Outside
Percentage (%)
1st
2nd
3rd
4th
5th
6th
7th
8th
9th
10th
Volumetric decile

Figure 15. Both dividing and non-dividing HSCs are most closely associated with sinusoids. a,b, Representative images of a Ki-67$^-$*α-catulin*-GFP$^+$c-kit$^+$ non-dividing HSC (**a,** arrow) and a Ki-67$^+$*α-catulin*-GFP$^+$c-kit$^+$ dividing HSC (**b**, arrow). **c,** 14.9±2.0% of HSCs were Ki-67$^+$. All data reflect mean±s.d. from bone marrow plugs (410-440 μm thick) from the diaphysis of 5 tibias in which a total of 2132 HSCs were analyzed in 5 independent experiments. **d-f**, The distance from Ki-67$^-$ non-dividing HSCs, Ki-67$^+$ dividing HSCs, or random spots to the nearest arteriole (**d**), sinusoid (**e**), or transition zone vessel (**f**). **g-i,** The percentages of all Ki-67$^-$ non-dividing HSCs, Ki-67$^+$ dividing HSCs, or random spots within 10μm of an arteriole (**g**), a sinusoid (**h**), or a transition zone vessel (**i**). **j,** Most Ki-67$^-$ non-dividing HSCs and Ki-67$^+$ dividing HSCs were most closely associated with sinusoids. **k,** The distributions of Ki-67$^-$ non-dividing HSCs, Ki-67$^+$ dividing HSCs, and random spots in concentric cylinders corresponding to equal volumetric deciles from central marrow to endosteal (outside) marrow. Non-dividing HSCs were significantly enriched in central marrow while dividing HSCs were significantly enriched toward the endosteum (**d-k** reflect mean±s.d. from bone marrow plugs from the diaphysis of 5 tibias in which a total of 1840 Ki-67$^-$ HSCs and 292 Ki-67$^+$ HSCs were analyzed in 5 independent experiments). In panels **d-f** and **k** the statistical significance of distribution differences was assessed by Kolmogorov–Smirnov analysis. In panels **g-j**, the statistical significance of differences between Ki-67$^-$ HSCs, Ki-67$^+$ HSCs, and random spots was assessed by Student's t-tests (*, P<0.05) and none were significant.

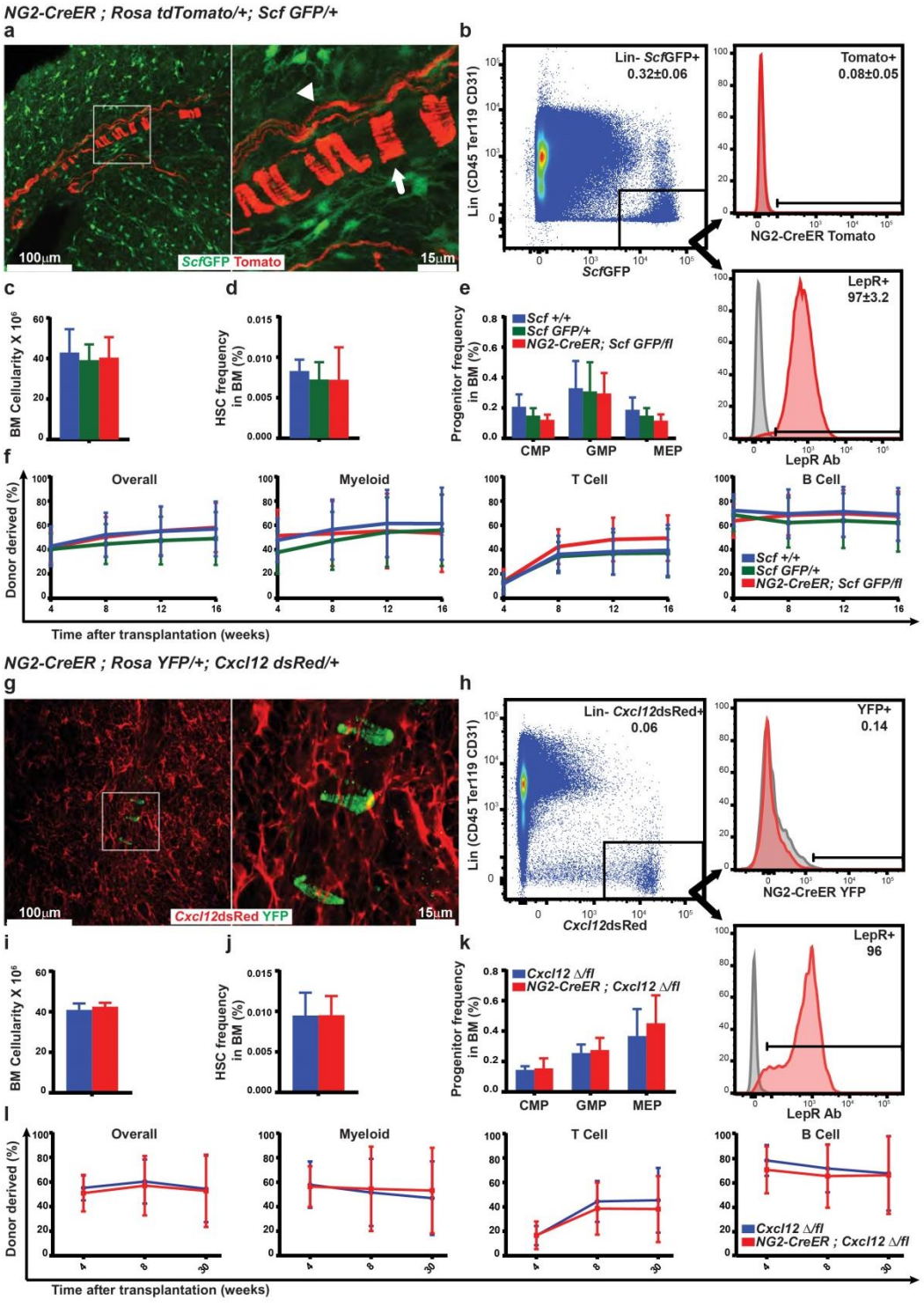
NG2-CreER ; Rosa tdTomato/+; Scf GFP/+
a
b
100μm
ScfGFP Tomato
15μm
Lin- ScfGFP+
0.32±0.06
Lin (CD45 Ter119 CD31)
ScfGFP
Tomato+
0.08±0.05
NG2-CreER Tomato
LepR+
97±3.2
LepR Ab
c
BM Cellularity X 10⁶
d
HSC frequency in BM (%)
e
Progenitor frequency in BM (%)
Scf +/+
Scf GFP/+
NG2-CreER; Scf GFP/fl
CMP
GMP
MEP
f
Donor derived (%)
Overall
Myeloid
T Cell
B Cell
Scf +/+
Scf GFP/+
NG2-CreER; Scf GFP/fl
Time after transplantation (weeks)
NG2-CreER ; Rosa YFP/+; Cxcl12 dsRed/+
g
h
100μm
Cxcl12dsRed YFP
15μm
Lin- Cxcl12dsRed+
0.06
Lin (CD45 Ter119 CD31)
Cxcl12dsRed
YFP+
0.14
NG2-CreER YFP
LepR+
96
LepR Ab
i
BM Cellularity X 10⁶
j
HSC frequency in BM (%)
k
Progenitor frequency in BM (%)
Cxcl12 Δ/fl
NG2-CreER ; Cxcl12 Δ/fl
CMP
GMP
MEP
l
Donor derived (%)
Overall
Myeloid
T Cell
B Cell
Cxcl12 Δ/fl
NG2-CreER ; Cxcl12 Δ/fl
Time after transplantation (weeks)

Figure 16. We were not able to detect any expression of *NG2*-CreER in *Scf* or *Cxcl12* expressing cells and conditional deletion of *Scf* or *Cxcl12* using *NG2*-CreER did not affect HSC frequency or bone marrow reconstituting capacity. **a,** Confocal image of a 20 μm optical section from a 390 μm thick cleared bone marrow plug from the tibia diaphysis of an $NG2^{CreER}$; $Rosa^{tdTomato/+}$; $Scf^{GFP/+}$ mouse (image is representative of bones from 4 mice). The image shows rare Tomato+ periartieriolar smooth muscle cells (arrow) as well as glial associated with nerve fibers (arrow head); however, we were unable to detect *Scf* expression by any of these cells. **b,** Representative flow cytometry plots showing the percentage of *Scf*-GFP+ stromal cells that were positive for Tomato expression (reflecting recombination by *NG2*-CreER) or LepR antibody staining (mean±SD from 4 mice in 3 independent experiments). *Scf*-GFP+ stromal cells were uniformly positive for LepR expression but negative for *NG2*-CreER. **c,d,e,f,** Conditional deletion of *Scf* in $NG2^{CreER}$; $Scf^{GFP/fl}$ mice had no effect on bone marrow cellularity (c), HSC frequency (d), CMP, GMP, or MEP frequency (e) or bone marrow reconstituting capacity upon transplantation into irradiated mice (f) (n=5 mice/genotype in 5 independent experiments with 4-5 recipient mice/donor in each experiment). **g,** Confocal image of a 20 μm optical section from the diaphysis of a 130 μm thick cleared bisected tibia from a $NG2^{CreER}$; $Rosa^{YFP/+}$; $Cxcl12^{dsRed/+}$ mouse. The image shows rare YFP+ periartieriolar smooth muscle cells; however, we were unable to detect *Cxcl12* expression by these cells. **h,** Representative flow cytometry plots showing the percentage of *Cxcl12*-DsRed+ stromal cells that were positive for YFP expression

(reflecting recombination by *NG2*-CreER) or LepR antibody staining. *Cxcl12*-DsRed+ stromal cells were uniformly positive for LepR expression but negative for *NG2*-CreER. **i,j,k,l,** Conditional deletion of *Cxcl12* in $NG2^{CreER}$; $Cxcl12^{-/fl}$ mice had no effect on bone marrow cellularity (i), HSC frequency (j), CMP, GMP, or MEP frequency (k) or bone marrow reconstituting capacity upon transplantation into irradiated mice (l) (n=4 mice/genotype in 4 independent experiments with 4-5 recipient mice/donor in each experiment).

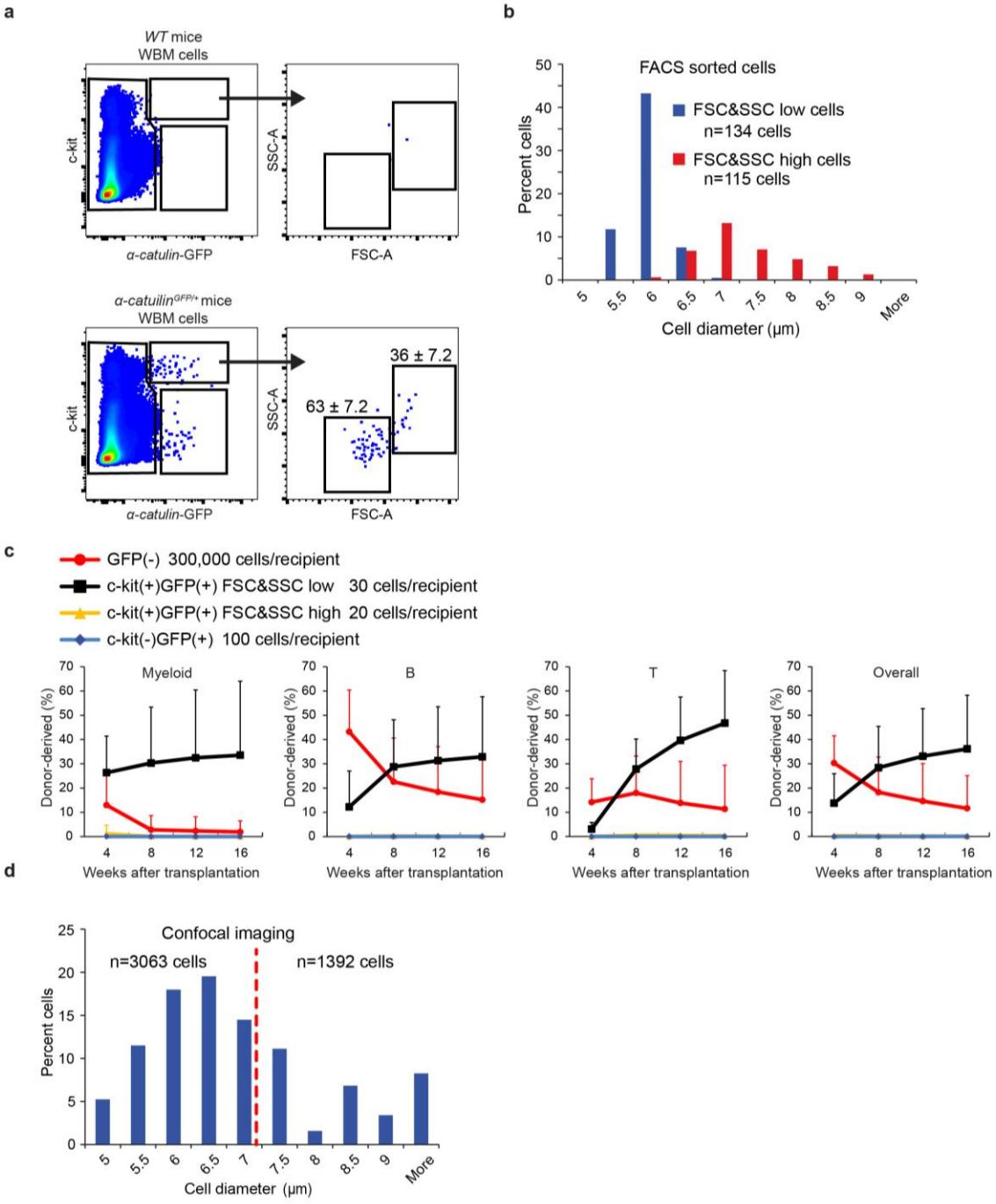
a
WT mice
WBM cells
c-kit
α-catulin-GFP
SSC-A
FSC-A
α-catulin GFP/+ mice
WBM cells
36 ± 7.2
63 ± 7.2
b
FACS sorted cells
FSC&SSC low cells
n=134 cells
FSC&SSC high cells
n=115 cells
Percent cells
Cell diameter (μm)
c
GFP(-) 300,000 cells/recipient
c-kit(+)GFP(+) FSC&SSC low 30 cells/recipient
c-kit(+)GFP(+) FSC&SSC high 20 cells/recipient
c-kit(-)GFP(+) 100 cells/recipient
Myeloid
B
T
Overall
Donor-derived (%)
Weeks after transplantation
d
Confocal imaging
n=3063 cells
n=1392 cells
Percent cells
Cell diameter (μm)

Figure 17. All HSC activity resides among *α-catulin*-GFP$^+$ckit$^+$ cells with low forward and side scatter. a, Most *α-catulin*-GFP$^+$ckit$^+$ cells (63±7.2%) had low forward and side scatter but a distinct minority population (36±7.2%) had higher forward and side scatters that were not typical of HSCs. **b,** We sorted the low scatter and the high scatter *α-catulin*-GFP$^+$ckit$^+$ cell populations gated in panel a and measured their diameters (3 independent experiments). **c,** Competitive reconstitution assays in irradiated mice revealed that all HSC activity resided in the low scatter cell fraction. For each recipient mouse, the indicated donor cells (based on the number of cells from each population contained within 300,000 bone marrow cells) were transplanted into irradiated mice along with 300,000 recipient bone marrow cells (mean±s.d. from 2 independent experiments with 4-10 recipient mice per group). **d,** The size distribution of all *α-catulin*-GFP$^+$ckit$^+$ cells identified by confocal microscopy in bone marrow plugs from the tibia diaphysis (6 bones analyzed in 6 independent experiments). In keeping with the flow cytometry data, the largest 40% of cells were not considered HSCs, excluding all cells with diameter larger than 7 μm.

2.7 Supplementary videos

Supplementary video 2.1. HSCs in the metaphysis of a tibia. A segment of tibia was fixed, stained with antibodies against c-kit (red), *α-Catulin*-GFP (white), and laminin (green), then cleared and imaged. Bone was imaged as second harmonic generation (gray). Endothelial cells were *α-Catulin*-GFP^{+} and HSCs were *α-Catulin*-GFP^{+}c-kit^{+}. To show the spatial relationship between HSCs and bone, blood vessels and other hematopoietic cells were masked, then laminin staining was unmasked to show the relationship between HSCs and blood vessels.

Supplementary video 2.2. HSCs are closely associated with Cxcl12^{high} stromal cells throughout the bone marrow. A bone marrow plug from the tibia of a *Cxcl12$^{DsRed/+}$; α-Catulin$^{GFP/+}$* mouse was stained with antibodies against GFP (green) and c-kit (white). Hematopoietic progenitors are c-kit^{+} (white), HSCs are *α-Catulin*-GFP^{+}c-kit^{+} (green and white), and Cxcl12^{high} stromal cells are DsRed^{+} (red). To make it possible to see examples of interactions between HSCs and Cxcl12^{high} stromal cells, all channels 20-30µm beyond the spot of interest were occasionally masked.

Supplementary video 2.3. HSCs localize mainly around sinusoids. A bone marrow plug from the tibia of a *α-Catulin$^{GFP/+}$* mouse was stained with antibodies against GFP (green), c-kit (red), and laminin (white). Hematopoietic progenitors are c-kit^{+} (red), HSCs are *α-Catulin*-GFP^{+}c-kit^{+} (green and red), and blood vessels are

marked by laminin (white). Hematopoietic cells other than HSCs are masked throughout most of the video to make it possible to see HSCs throughout the marrow. Note that HSCs tend to localize in the central marrow around sinusoids that are dimly stained for laminin. The *α-Catulin*-GFP signal from c-kit negative endothelial cells was also masked for clarity.

2.8 Acknowledgements

S.J.M. is a Howard Hughes Medical Institute (HHMI) Investigator, the Mary McDermott Cook Chair in Pediatric Genetics, the director of the Hamon Laboratory for Stem Cells and Cancer, and a Cancer Prevention and Research Institute of Texas Scholar. J.G.P is a National Science Foundation Graduate Research Fellow. This work was supported by the NIH NHLBI (HL097760) and NIH Shared Instrumentation grant NIH S10RR029731. We thank K. Correll and M. Gross for mouse colony management; N. Loof and the Moody Foundation Flow Cytometry Facility; and Abhijit Bugde of the UT Southwestern Live Cell Imaging Facility; and Ying Liu from the Baylor College of Dentistry microCT facility. We also gratefully acknowledge Bitplane customer support, especially Daniel Miranda and Arvonn Tully, Zeiss customer support, especially Sven Terclavers, and Leica application specialists Larry Smith and Haridas Pudavar.

2.9 Author statement

M.A., K.K., M.M., J.G.P., and S.J.M. conceived various aspects of the project, designed, and interpreted experiments. M.A. found *α-catulin* is highly restricted in expression to HSCs, made, and characterized the *α-catulin*$^{GFP/+}$ mice. Experiments were performed by M.A., K.K., M.M.M., J.G.P., C.N.I., and H.O. with technical assistance from C.J.. The confocal imaging and three dimensional rendering protocols were developed by M.A., K.K., M.M.M., and K.L.P.. Z.Z. and J.G.P. performed computational image analysis. The manuscript was written by M.A., K.K., M.M.M, J.G.P., Z.Z. and S.J.M.

CHAPTER THREE
Bone marrow sympathetic nerves are required for hematopoietic regeneration after injury

3.1 Abstract

Sympathetic nerves innervating the bone marrow have been implicated in the regulation of hematopoiesis. However, these studies relied on model systems that induced a loss of sympathetic nerves in both the bone marrow and other tissues. We discovered that nerve growth factor (*Ngf*) is the primary neurotrophin expressed in the bone marrow. It is produced by leptin receptor-expressing perivascular stromal cells. By conditionally deleting *Ngf* from perivascular stromal cells we generated mice that lack innervation of the bone marrow, but are not generally sypathectomized. We then used these mice to assess the role of bone marrow nerves in regulating hematopoiesis. Mice which lacked bone marrow innervation had normal hematopoiesis, but exhibited defects in circadian mobilization of progenitors. *Ngf* conditional mutant mice failed to recover bone marrow hematopoiesis after irradiation and bone marrow transplantation, and this defect was rescued by treating irradiated mice with the β2 adrenergic receptor agonist salbutamol. Previous studies suggested that perivascular stromal cells and endothelial cells are induced to proliferate in mice lacking sympathetic nerves. However, we found that perivascular stromal cells and endothelial cells of mice without bone

marrow nerves did not exhibit defects in frequency or proliferative status, either in steady state or during regeneration.

3.2 Introduction

The autonomic nervous system has been implicated in regulating hematopoiesis and hematopoietic stem cells (HSCs), but the contexts in which nerves regulate hematopoiesis and the mechanisms through which they influence the bone marrow remain controversial. Reports using different models of peripheral neuropathy suggest that nerves are required for hematopoietic homeostasis and HSC maintenance (Afan et al., 1997; Yamazaki et al., 2011), mobilization of progenitors to the blood (Katayama et al., 2006; Lucas et al., 2008; Méndez-Ferrer et al., 2008, 2010a), homeostasis of HSC niche cells (Lucas et al., 2013), recovery from bone marrow injury (Lucas et al., 2013), and also play a role in antagonizing tumorigenesis (Arranz et al., 2014; Hanoun et al., 2014). These studies have used three different approaches for removing sympathetic nerves, (1) surgically resecting the lumbar sympathetic trunk (Afan et al., 1997; Yamazaki et al., 2011), (2) chemical sympathectomy with 6-hydroxydopamine or chemotherapy (Lucas et al., 2013), and (3) deleting genes essential for peripheral nerve function from neurons or from the germline (Katayama et al., 2006; Lucas et al., 2013). A shortcoming of all these approaches is that the sympathetic nerves are absent from both the bone marrow and other tissues, making it impossible to distinguish between the direct effects of bone marrow nerves on hematopoiesis and indirect effects of SNS dysfunction.

To avoid these shortcomings, we sought to develop a model of peripheral denervation in which only the bone marrow nerves, but not other peripheral nerves, are disrupted. Sympathetic nerves rely on signaling from the neurotrophin family of proteins for their survival, which act through p75 and the Trk family of receptors to maintain healthy axons. Sympathetic neurons grown *in vitro* retract in the absence of neurotrophins, and genetic deletion or antibody-mediated inactivation of neurotrophins *in vivo* leads to the retraction of peripheral nerves (Aloe et al., 2012; Gómez-Casati et al., 2010; Lindsay, 1988; Ma et al., 2009). Neurotrophins are expressed within the target tissues of the peripheral nerves (Terenghi, 1999). Conditional deletion of brain-derived neurotrophic factor (*Bdnf*) in the tongue or neurotrophin 3 (*Ntf3*) in the inner ear from non-neural cells leads to defects in synapse formation and innervation (Gómez-Casati et al., 2010; Ma et al., 2009; Wan et al., 2014). Therefore, we hypothesized that by conditionally deleting the neurotrophins crucial for bone marrow innervation from marrow cells but not other tissues, we could generate mice lacking bone marrow nerves but not other nerves. These mice would then allow us to address whether the previously reported roles for innervation in the regulation of hematopoiesis were due to the action of bone marrow nerves or an indirect consequence of general sympathectomy.

3.3 Results

Ngf is the only neurotrophin expressed at high levels in the bone marrow

Sympathetic nerves require continuous signaling from neurotrophin family members for their survival (reviewed by Patapoutian and Reichardt 2001). To identify the source of neurotrophin expression in the adult bone marrow, we analyzed the expression of neurotrophins from various bone marrow populations. Nerves enter the bone marrow along the nutrient artery through the foramen in diaphyseal bone (Figure 18a), and nerves and arterioles co-localize throughout the bone marrow (Travlos, 2006). We measured neurotrophin expression in perivascular stromal cells expressing *Scf*, osteoblasts, endothelial cells, and whole bone marrow cells. Only one neurotrophin, *Ngf*, was expressed in the marrow, and almost all *Ngf* expression was restricted to *Scf*-expressing perivascular cells (Figure 18c). *Scf*-expressing cells can also be identified using *LepR^{cre}; tdTomato* lineage tracing (Zhou et al., 2014), which marks primarily perisinusoidal cells, but also some periarteriolar smooth muscle cells (Ding et al., 2012; Zhou et al., 2014) (Figure 18b). *Ngf* was expressed by both smooth muscle cells expressing express smooth muscle actin (*Sma*) or *Ng2* (Zhou et al., 2014) and in populations composed of primarily perisinusoidal cells, marked by *Scf*-GFP or *LepR^{cre}; tdTomato* (Figure 18d). We directly tested the abundance of neurotrophin transcripts in the bone marrow using RNA-seq analysis, and found that no neurotrophins besides *Ngf* were expressed at a level above background (Figure 19a).

Ngf produced by leptin receptor-expressing perivascular stromal cells is required to maintain bone marrow innervation

We next wanted to test whether *Ngf* was required to maintain innervation of the bone marrow. To do this, we generated mice with a conditional knockout allele for *Ngf* (*Ngf* $^{fl/-}$ mice, Figure 20a-d) and crossed them to mice expressing *Cre* under the control of promoters specifically active in bone marrow perivascular stromal cells. We previously showed that *LepR* expression marks bone marrow stromal cells responsible for producing SCF and CXCL12 to maintain HSCs (Ding and Morrison, 2013; Ding et al., 2012). Since *Ngf* production in the bone marrow is restricted to these cells, we tested whether leptin receptor-expressing cells also play a role in maintaining bone marrow innervation. In mice younger than eight weeks old, when the recombination efficiency of *LepR-Cre* is below 80% (Ding et al., 2012), *LepR*^{cre}*; Ngf* $^{fl/-}$ mice have peripheral nerves in their bone marrow (Table 1). However, after sixteen weeks of age, when the deletion efficiency of *LepR-Cre* is above 95% (Zhou et al., 2014), *LepR*^{cre}*; Ngf* $^{fl/-}$ mice exhibit a lack of bone marrow nerves in all marrow compartments analyzed, including the vertebrae (Figure 21a, b), long bones (Figure 21c, d, Table 1), and sternum (data not shown). *LepR*^{cre}*; Ngf* $^{fl/-}$ mice only lack nerves in the marrow, as tyrosine hydroxylase-positive (TH^+) or neurofilament H-positive (NFH^+) neurons can be seen in the sciatic nerves (Figure 21e, f) and within the nutrient foramen of the bone (Figure 21d, arrowhead).

LepR^{cre}*; Ngf* $^{fl/-}$ mice have normal hematopoiesis but lack circadian progenitor mobilization

Nerves have been reported to regulate hematopoiesis in the steady state to maintain HSCs (Afan et al., 1997; Yamazaki et al., 2011) or induce circadian mobilization of progenitors to the peripheral blood (Katayama et al., 2006; Lucas et al., 2013; Méndez-Ferrer et al., 2008). To test whether the bone marrow nerves play a role in these processes, we analyzed the hematopoietic systems of *LepR^{cre}; Ngf $^{fl/-}$* mice. Bone marrow cellularity and the number of circulating white blood cells, lymphocytes, and red blood cells were unchanged between *LepR^{cre}; Ngf $^{fl/-}$* mice and littermate controls (Figure 22a-c). The frequency of hematopoietic stem and progenitor cells was also not significantly different when assessed either by flow cytometry, transplantation, or CFU-C (Figure 22d-g). In agreement with earlier studies (Lucas et al., 2008; Méndez-Ferrer et al., 2008), we observed a defect in the circadian mobilization of Lin$^-$Sca1$^+$c-kit$^+$ (LSK) progenitor cells into the blood during midmorning (Zeitgeiber Time 5) (Figure 22h, i). However, we did not observe a defect in G-CSF-induced mobilization of hematopoietic progenitors, as the frequency of colony-forming progenitors present in the spleen or peripheral blood was equally enhanced by four days of G-CSF administration in both *LepR^{cre}; Ngf $^{fl/-}$* mice and littermate controls (Figure 22j, k).

Prx1^{cre}; Ngf $^{fl/-}$ mice lack innervation in long bones but not vertebrae

Our group and others (Ding and Morrison, 2013; Greenbaum et al., 2013) have previously shown that LepR-expressing stromal cells can also be targeted in the bone marrow by *Prx1-Cre*, which deletes with high efficiency during early

development in the limb bud mesoderm (Logan et al., 2002). *Prx1-Cre* deletes with high efficiency in the perivascular stromal cells of limb bones, but does not recombine at all in vertebral bone marrow (Figure 23a, b, Figure 24a, b). We found that young *Prx1^{cre}; Ngf $^{fl/-}$* mice have TH^{+} neruons in their vertebrae (Figure 23c) and sciatic nerve (Figure 24c) but not in their long bones (Figure 4D, Table 1). Like *LepR^{cre}; Ngf $^{fl/-}$* mice, young *Prx1^{cre}; Ngf $^{fl/-}$* mice had no gross defects in hematopoiesis in their long bones, as measured by marrow cellularity, frequency of progenitors, competitive transplantation, and CFU-C (Figure 23e-j). *Prx1^{cre}; Ngf $^{fl/-}$* mice did have a small but significant increase in the frequency of HSCs in their long bones (Figure 23g) but not their vertebrae (Figure 24d); however, this difference was very small and did not reflect any change in the frequency of HSCs actively in cycle, as measured by BrdU incorporation (Figure 23i).

Previous work has implicated nerves in the regulation of endothelial and perivascular cell proliferation (Lucas et al., 2013). *Prx1^{cre}; Ngf $^{fl/-}$* mice have equal numbers of both endothelial (VE-Cadherin^{+}CD45/Ter119^{-}) and perivascular cells (PDGFRα^{+}VE-Cadherin^{-}CD45/Ter119^{-}) (Figure 23k), and equal numbers of CFU-F (Figure 23l), compared to littermate controls, suggesting that there is no defect in the maintenance of these cells in mice lacking bone marrow nerves. In healthy bone marrow, endothelial cells (Li et al., 2008) and perivascular cells (Zhou et al., 2014) are both highly quiescent, an observation we confirmed (Figure 23m, n). We did not observe an increase in the frequency of either endothelial or perivascular cells that enter cell cycle in *Prx1^{cre}; Ngf $^{fl/-}$* mice (Figure 23m, n). Furthermore, when we give

Prx1^{cre}; Ngf $^{fl/-}$ mice the β2 adrenergic receptor agonist salbutamol, a memetic for catecholiminergic nerve signaling (Cullum et al., 1969), there is no reduction in the frequency of stromal cells entering cell cycle (Figure 23m, n). This suggests that bone marrow nerves do not function by regulating the proliferation of endothelial and perivascular cells.

Prx1^{cre}; Ngf $^{fl/-}$ mice fail to recover from severe bone marrow injury

Previous data suggest that sympathetic nerves are required for successful recovery after bone marrow injury (Lucas et al., 2013). To test whether these defects in marrow recovery were due to the lack of bone marrow nerves or were an indirect consequence of general sympathectomy, we gave bone marrow transplants to *Prx1^{cre}; Ngf $^{fl/-}$* mice and control mice treated with either 6-hydroxydopamine (6OHDA) or saline. We observed that some 6OHDA-treated mice (5/20 mice, 25%) (Figure 25a) and a similar frequency of *Prx1^{cre}; Ngf $^{fl/-}$* mice (3/14, 21%) (Figure 25a) died following transplantation, suggesting that indeed the marrow nerves do play a role in recovery after transplantation. Surviving *Prx1^{cre}; Ngf $^{fl/-}$* mice exhibited marrow aplasia in their leg bones (Figure 25b, c) accompanied by an overgrowth of adipocytes (Figure 25d, e, Figure 26c). Compared to wild-type controls, *Prx1^{cre}; Ngf $^{fl/-}$* mice displayed a severe reduction in the frequency of LSK cells and HSCs in their denervated leg bones, but not vertebral bones thirty days after transplantation (Figure 25f, g). The restoration of hematopoiesis in the innervated vertebral bones of

Prx1^{cre}; Ngf $^{fl/-}$ mice is especially useful as an internal control, showing that only innervated marrow compartments are capable of normal regeneration after injury.

Marrow nerves do not control sensitivity of stromal cells to genotoxic insult

One proposed mechanism by which nerves regulate marrow regeneration is by increasing the frequency of perivascular stromal cells and endothelial cells in cycle in the steady state, which make them more susceptible to genotoxic stressors such as irradiation, which preferentially kills cells in cycle (Lucas et al., 2013). Although we showed that the frequency and proliferation of endothelial and perivascular stromal cells is not changed by the absence of bone marrow nerves, we wanted to test directly whether these cell populations are more susceptible to genotoxic insult in the absence of nerves. We observed no significant differences in the number or proliferative status of perivascular or endothelial cells one, two, or four weeks following irradiation and transplantation into 6OHDA or saline treated mice, even though 6OHDA-treaded mice exhibited aplasia (Figure 26a, Figure 27a-d). Perivascular cells were also no more likely to be undergoing apoptosis in aplastic, nerveless mice than normally regenerating mice a four weeks after transplant (Figure 27e). These data challenge the hypothesis that nerve-mediated marrow regeneration is caused by increased susceptibility of endothelial and perivascular cells to irradiation.

Since we could detect no hematopoietic defects in bone marrow homeostasis in *Prx1^{cre}; Ngf $^{fl/-}$* or 6OHDA-treated mice, we hypothesized that signaling from the

nerves during regeneration, not before injury, was critical to successful recovery. Sympathetic nerves act through the secretion of norepinephrine from their axon terminals, which signals through adrenergic receptors (ARs) on target cells (Molinoff, 1984). Both β2 and β3 ARs are expressed in the bone marrow (Figure 28a) and have been reported to regulate the behavior of hematopoietic (β2) and stromal cells (β2 and β3) in the bone marrow (Lucas et al., 2013; Méndez-Ferrer et al., 2010a). To test whether post-injury signaling through βARs was sufficient to induce marrow recovery, we administered daily intravenous injections of the β2 AR agonist salbutamol to nerveless *Prx1^{cre}; Ngf $^{fl/-}$* or 6OHDA-treated mice for two weeks after irradiation and bone marrow transplantation. Salbutamol rescued the defects in the numbers of hematopoietic cells, progenitors, and stem cells in the bone marrow of mice that lacked bone marrow nerves (Figure 25h-j). Those mice also exhibited no marrow aplasia (Figure 26b) and reduced adiposity (Figure 26c) compared with untreated nerveless mice. These data suggest that adrenergic signals after catastrophic bone marrow injury are necessary to successfully regenerate the marrow and restore hematopoiesis.

3.4 Discussion

Here we present the first model of bone marrow specific denervation, which allows us to distinguish between the specific influences of marrow nerves and the effects on hematopoiesis of the SNS as a whole. Our data support the conclusion that disruption of bone marrow nerves has no dramatic effects on steady-state

hematopoiesis, except to inhibit the circadian cycling of hematopoietic progenitors, in agreement with the conclusions from previous studies using models of complete sympathectomy (Katayama et al., 2006; Lucas et al., 2013; Méndez-Ferrer et al., 2008) but in contrast to studies that used invasive surgical denervation (Afan et al., 1997; Yamazaki et al., 2011). Our data indicate that mice lacking bone marrow nerves have no defect in endothelial or perivascular cells. This is consistent with data showing that nerves do not alter steady-state hematopoiesis, as changes in homeostasis of HSC niche components would likely alter HSC frequency or proliferation. This observation addresses some inconsistencies in a previous report, which suggested that the HSC niche was expanded in the absence of nerves, but showed no increase in HSCs in nerveless mice (Lucas et al., 2013).

A previous study came to the conclusion that the role of bone marrow nerves is to negatively regulate the proliferation of perivascular and endothelial cells, and thereby protect them from genotoxic insult by preventing radiation-induced cell death (Hanoun et al., 2015; Lucas et al., 2013). This conclusion is not consistent with our data. Our data suggest that the absolute number and proliferative status of HSC niche components is not different between mice with and without nerves both in steady state and throughout the first month after marrow injury. By rescuing nerveless, injured mice with agonists to β adrenergic receptors, our data demonstrates that nerve signaling after injury is responsible for successful regeneration, an observation consistent with but not directly tested in previous studies.

The mechanism by which nerves promote marrow regeneration remains unclear. Previous studies have implicated TGF-β signaling activated by non-myelinating Schwann cells in regulating hematopoiesis (Yamazaki et al., 2011), but other signaling pathways have been associated with both nerve action and regeneration after injury, especially in the modulation of inflammatory responses (Pongratz and Straub, 2014; Straub et al., 2006). To understand the mechanism of neural regulation of bone marrow regeneration, it will be critical to examine the cell-intrinsic and cell-extrinsic pathways active during normal regeneration but absent during regeneration in nerveless mice.

Yamazaki and Allen used electron microscopy to describe the periarteriolar cell types on which efferent nerves form terminals (Yamazaki and Allen, 1990); however, whether these cells are *SMA*-expressing smooth muscle cells, *LepR*-expressing reticular cells, or another type of cell not identified by existing markers is unknown. Future studies will have to identify the target cells of marrow nerves and evaluate how they change in response to signaling from the SNS.

Since SNS denervation is a relatively common consequence of both chemotherapy (Kelly and Karcher, 2005) and diabetes mellitus (Tesfaye and Selvarajah, 2012), understanding the precise role of marrow nerves is critical to protecting denervated patients from unforeseen complications as a consequence of marrow injury, such as bone marrow transplantation or additional rounds of chemotherapy. Additionally, our data suggest that activation of bone marrow adrenergic receptors may provide a clinically applicable route to help patients in

need of chemotherapy or a bone marrow transplant recover their hematopoietic function, even patients that already lack nerves, such as those with advanced diabetes mellitus, for whom neuroprotective therapies would have no effect.

3.5 Methods

Mice. The targeting vector was obtained from The European Conditional Mouse Mutagenesis Program (EUCOMM), linearized, and electroporated into C57BL-derived Bruce4 ES cells. Successfully targeted clones were expanded and injected into C57BL/6-Tyr$^{c\text{-}2J}$ blastocysts. Chimeric mice were bred with C57BL/6-Tyr$^{c\text{-}2J}$ mice to obtain germline transmission. The *Frt*-flanked *LacZ* and *neo* cassette was removed by mating with *Flpe* mice (Rodríguez et al., 2000) and backcrossed for at least two generations onto a C57BL/Ka background. Mice used in this study included *LepR-Cre* (DeFalco et al., 2001), *Prx1-Cre* (Logan et al., 2002), t*dTomato*, which we obtained from Jackson Laboratories, *Scf*-GFP, which was generated in our lab and we reported previously, and the germline null allele of *Ngf* (Crowley et al., 1994), which was a gift from David Ginty*. Ngf* mice were maintained as *flox* over *null*, since this breeding strategy sensitizes mice to changes in gene expression in the context of incomplete deletion by *Cre* alleles.

All mice were housed in the Animal Resource Center at the University of Texas Southwestern Medical Center. All protocols used in this study were approved by the University of Texas Southwestern Institutional Animal Care and Use Committee.

Quantitative RT-PCR analysis. Cell populations were sorted directly into Trizol (Life Technologies). Total RNA was extracted according to manufacturer's instructions. Total RNA was subjected to reverse transcription using the Superscript III system (Life Technologies). Quantitative real-time PCR was run using SYBR green on a LightCycler 480 (Roche). β-Actin was used to normalize the RNA content of samples. Primers used in this study were: *Ngf*: OJP011F, 5'-CCAAGGACGCAGCTTTCTATAC-3' and OJP011R 5'-CTGCCTGTACGCCGATCAAAA-3'; β-actin: ActF, GCTCTTTTCCAGCCTTCCTT-3′ and ActR, 5′-CTTCTGCATCCTGTCAGCAA-3′.

Microarray and RNA-seq analysis. We performed microarray analysis of bone marrow populations as reported previously (Ding et al., 2012). 5,000 *Scf*-GFP+ cells, osteoblasts, endothelial cells, or whole bone marrow cells were sorted into Trizol. Total RNA was extracted and amplified using the WT-Ovation Pico RNA Amplification system (Nugen) following manufacturer's instructions. Sense strand cDNA was generated using the WT-Ovation Exon Module (Nugen). Then, cDNA was fragmented and labelled using FL-Ovation DNA Biotin Module V2 (Nugen). The labelled cDNA was hybridized to Affymetrix Mouse Gene ST 1.0 chips following the manufacturer's instructions. Expression values for all probes were normalized and determined using the robust multi-array average (RMA) method (Irizarry et al., 2003). cDNAs from *LepR*^{cre}*; tdTomato*+ cells, endothelial cells, and whole bone

marrow cells were similarly isolated for RNA-seq analysis, which was performed on an Illumina sequencer in accordance with manufacturer's instructions.

PCR genotyping. The following primers were used to identify the successful insertion of the *Ngf* ^{flox} construct into ES cells: 5' Primer F.GF4, 5'-GAGGCGGCTGTCGCTCCGGAGTTGTG-3'; 5' Primer R.LAR3, 5'-CACAACGGGTTCTTCTGTTAGTCC-3'; 3' Primer F.R2R, 5'-TCTATAGTCGCAGTAGGCGG-3'; 3' Primer R.GR3, 5'-CACAAGGCCTTCTCATCCGCATTCAACCAG-3'; dLoxP R, 5'-GTATGCTATACGAAGTTATCATTAATTGC-3'. The following primers were used for genotyping. *Ngf* ^{flox} allele: OJP.Ngf.geno.F, 5'-CTTGTTTTCCATCATAGAGTTGGCTTGTT-3'; OJP.Ngf.alt.geno.R, 5'-TATACTGGCCGCAGTGAGGTAAG-3'. *Ngf* ^{null} allele: oIMR5367, 5'-CAGGCAGAACCGTACACAGA-3'; oIMR5368, 5'-CTGTCACTCGGGCAGCTATT-3'; oIMR6218, 5'-CCTTCTATCGCCTTCTTGACG-3'. *Cre* allele: CreF2, 5'-CGCCGCATAACCAGTGAAAC-3'; CreR3, 5'-GGACATGTTCAGGGATCGCC-3'. *Scf*-GFP allele: OJP_SCF-GFP_1, 5'-CCCGCAGCTCTGGTATATTTGC-3'; OJP_SCF-GFP_2, 5'-CGGACACGCTGAACTTGTGG-3'; OJP_SCF-GFP_3, 5'-AAGCACTTCAGATTCTAGGG-3'. *TdTomato* allele: OJP_Tdtomato1, 5'-AAGGGAGCTGCAGTGGAGTA-3'; OJP_Tdtomato2, 5'-CCGAAAATCTGTGGGAAGTC-3'; OJP_Tdtomato3, 5'-

GGCATTAAAGCAGCGTATCC-3'; OJP_Tdtomato4, 5'-CTGTTCCTGTACGGCATGG-3'.

Immunofluorescence, clearing, microscopy, and analysis.

Confocal images were obtained using a method we previously described (Açar et al., 2015). Briefly, bones were fixed in cold 4% paraformaldehyde (PFA) in PBS (Affymetrix) for 7-8 hours at 4°C. The bones were washed with PBS and cryoprotected in 30% sucrose PBS solution overnight at 4°C and embedded in OCT (Fisher) and flash frozen in liquid nitrogen. A Leica cryostat was used to longitudinally bisect the bones. Intact half bone was washed in PBS to remove OCT then processed for staining. The staining solution contained 10% DMSO, 0.5% IgePal630 (Sigma), and 5% donkey serum (Jackson ImmunoResearch) in PBS. Half bones were blocked in staining solution overnight at room temperature. After blocking, half bones were stained for 3 days at room temperature with primary antibodies in staining solution. Then the tissues were washed multiple times in PBS at room temperature for one day and put into staining solution containing secondary antibodies for 3 days followed by a one day wash. Antibodies used for whole mount staining included chicken anti-GFP (GFP-1020, Aves Labs) rabbit anti-Laminin (ab7463, abcam), rabbit anti-Tyrosine Hydroxylase (AB152, Millipore), chicken anti-Neurofilament H (NFH, Aves Labs), goat anti-CD105 (AF1320, Fisher), chicken anti-GFP (GFP-1020, Aves Labs), rabbit anti-DsRed (632496, Clontech), Alexa Fluor 647-AffiniPure F(ab')2 Fragment Donkey Anti-Chicken IgY, Alexa Fluor 488-

AffiniPure F(ab')2 Fragment Donkey Anti-Rabbit IgG, AMCA-AffiniPure F(ab')2 Fragment Donkey Anti-Rabbit Ig, Alexa Fluor 488-AffiniPure F(ab')2 Fragment Donkey Anti-Rat IgG (all from Jackson ImmunoResearch), and 555 or 488 conjugated donkey anti-goat (A-11055 and A-21432 from Life Technologies). The stained half bones were dehydrated in a methanol dehydration series then incubated for 3 hours in 100% methanol with several changes. The methanol was then exchanged with benzyl alcohol:benzyl benzoate 1:2 mix (BABB clearing[39]). The tissues were incubated in BABB for 3 hours to overnight with several exchanges of fresh BABB. Half bones were mounted in BABB between two cover slips and sealed with silicone (Premium waterproof silicone II clear, General Electric). . Images were acquired using a Zeiss LSM780 confocal microscope with a Zeiss LD LCI Plan-Apo 25x/0.8 multi-immersion objective lens, which has a 570 µm working distance. Images were taken at 512x512 pixel resolution with 2 µm Z-steps, pinhole for the internal detector at 47.7 µm.

Image annotation and analysis. Confocal tiled Z-stack images were rendered in 3 dimensions and analyzed using Bitplane Imaris v7.7.1 software installed on a Dell Precision T7610 64-bit workstation with Dual Intel Xeon Processor E5-2687W v2 (Eight Core HT, 3.4GHz Turbo, 25 MB),128GB RAM, and 16 GB AMD FirePro W9100 graphics card. Nerve staining with tyrosine hydroxylase antibodies was identified manually and nerve surfaces were generated procedurally in innervated regions identifying high, continuous, tyrosine hydroxylase staining. The nerve

surfaces generated this way have been superimposed over the images of vasculature to aid in the visualization of bone marrow innervation in three dimensions.

Hematopoietic and stromal cell isolation and flow cytometry. Bone marrow cells were isolated by either flushing the long bones (tibias and femurs), or by crushing vertebrae or long bones using a mortar and pestle in Ca^{2+} and Mg^{2+} free Hank's buffered salt solution (HBSS, Gibco) supplemented with 2% heat inactivated bovine serum (Gibco). Spleen cells were prepared by crushing the spleen between two glass slides. The cells were gently passed through a 25G needle then filtered using a 100 μm mesh to generate a single cell suspension. Viable cell number was calculated using a Vi-Cell cell counter (Beckman Coulter). For flow cytometry involving stromal cells, bone marrow plugs were flushed into Eppendorf tubes containing Liberase TM (Roche Biosciences) and DNAse (Sigma), agitated using a rotary shaker for 15 minutes two times, collecting the cells in the supernatant and filtering into tubes containing HBSS with 2% serum after each cycle before counting and flow cytometric analysis. For HSC identification by flow cytometry, the cells were stained with antibodies against CD150 (TC15-12F12.2), CD48 (HM48-1), Sca1 (E13-161-7), and c-kit (2B8), as well as the following lineage markers: CD42d (1C2), CD2 (RM2-5), CD3 (17A2), CD5 (53-7.3), CD8 (53-6.7), B220 (6B2), Ter119 (TER-119), and Gr1 (8C5). For stromal cell identification, cells were stained with antibodies to PDGFRα (APA5), CD105 (MJ7/18), VE-Cadherin (BV13), CD45 (30-

F11), and Ter119. Antibody staining of cell suspensions was always performed at 4°C for 30 minutes. After antibody staining, the cells were stained with the viability dyes 4′,6-diamidino-2-phenylindole (DAPI; 1μg/ml in PBS) or 7-Aminoactinomycin D (7-AAD; 5μg/ml) to exclude dead cells during flow cytometry. To identify other hematopoietic progenitors (CMPs, GMPs and MEPs) we stained cell suspensions with antibodies against CD34 (RAM34), CD16/32 (FcγR, 93), Sca1 (E13-161-7), c-kit (2B8) and the lineage markers listed above. Stains that involved anti-CD34 antibody were conducted for 90 minutes on ice.

Colony formation in methylcellulose. 10,000 bone marrow or 100,000 spleen or blood cells were sorted into methylcellulose culture medium (M3434, Stemcell Technologies) in 6 well plates. After sorting the plates were kept at 37°C in a cell culture incubator with 6.5% CO_2 and constant humidity for 14 days. Then colonies were counted and identified based on size and morphology using an Olympus IX81 inverted microscope.

Bone marrow transplantation assays. Adult recipient mice were administered a minimum lethal dose of radiation using an XRAD 320 X-ray irradiator (Precision X-Ray) to deliver two doses of 540 rads at least 3 hours apart. Cells were transplanted by injection into the retro-orbital venous sinus of anesthetized recipient mice. 200,000 recipient whole bone marrow (WBM) cells were transplanted along with the donor cells in competitive transplants. Blood was collected from the submandibular

veins of recipient mice 16 weeks after transplantation. For analysis of the levels of donor cells in peripheral blood, red blood cells were lysed with ammonium potassium buffer then the remaining cells were stained with antibodies against CD45.1 (A20), CD45.2 (104), CD11b (Mac1, M1-70), Gr-1 (8C5), B220 (6B2), and CD3 (17A2).

For experiments involving the transplant of bone marrow into nerve-impaired recipient mice, only 200,000 wild-type donor cells were used with no competitor cells, and mice were sacrificed for analysis 7, 14, or 30 days after irradiation and transplantation.

Mobilization of progenitors with G-CSF. Mice received G-CSF (250 mg per kg body weight per day) subcutaneously every day for four consecutive days. The final dose of G-CSF was given 2 hours before the mice were analyzed at the lowest point of circadian-induced mobilization, ZT13.

Adrenergic receptor β2 stimulation. Either 6 hours before analysis is steady state mice or daily for 14 days starting the day after bone marrow transplantation, mice were given intravenous injections of 2.5 mg/kg/day salbutamol to inhibit adrenergic receptor β2 signaling.

Cell Cycle Analysis. To assess 5-bromo-2'-deoxyuridine (BrdU) incorporation in vivo mice were intraperitoneally injected with a single dose of BrdU (1mg BrdU/10g

body mass) twenty-four hours before analysis. For analysis of HSCs, perivascular cells, or endothelial cells, after antibody staining, the target cell populations were double sorted to ensure purity, then fixed and stained with an anti-BrdU antibody using the BrdU APC Flow Kit (BD Biosciences) according to the manufacturer's instructions.

Chemical sympathectomy with 6-hydroxydopamine. Mice were given intraperitoneal injections of 6OHDA-hydrobromide (Sigma) 3 days (100 mg/kg body weight) and 1 day (250 mg/kg body weight) before irradiation and transplantation. Mice were sacrificed 48 hours after the last dose of 6OHDA for steady state analyses.

Histological analysis of bone marrow sections. Bones from irradiated mice were handed over to the UT Southwestern histology core, where they were fixed and decalcified before being embedded in paraffin. Thin sections were then taken and stained briefly with hematoxylin and eosin and then imaged using an Olympus IX81 microscope.

Quantification of marrow adiposity. The proportion of bone marrow area within single optical sections 2μm thick occupied by adipocytes was calculated using the area measurement function in ImageJ. To do this, fields of view in an imaged tibia were randomly selected using a random number generator to select X, Y, and Z start

coordinates within the bone marrow image in Imaris. Then, a snapshot was taken of a single optical section and exported to ImageJ. There, adipocytes were manually identified by their characteristic round shape, and a circular selection tool was used to highlight the area occupied by that adipocyte in the optical section. This process was repeated for each adipocyte visible in an optical section, and then the total adipocyte area was summed and compared to the total bone marrow area present in the field of view that had been chosen.

Quantification of perivascular cell apoptosis. Levels of apoptosis in perivascular cells was detected by flow cytometry using the CellEvent Caspase-3/7 Green Flow Cytometry Assay Kit (Life Technologies). Cells were simultaneously stained with the Caspase-3/7 detection reagent according to the manufacturer's instructions and antibodies to the cell surface markers we used to identify perivascular cells above before being analyzed by flow cytometry.

3.6 Figures and table

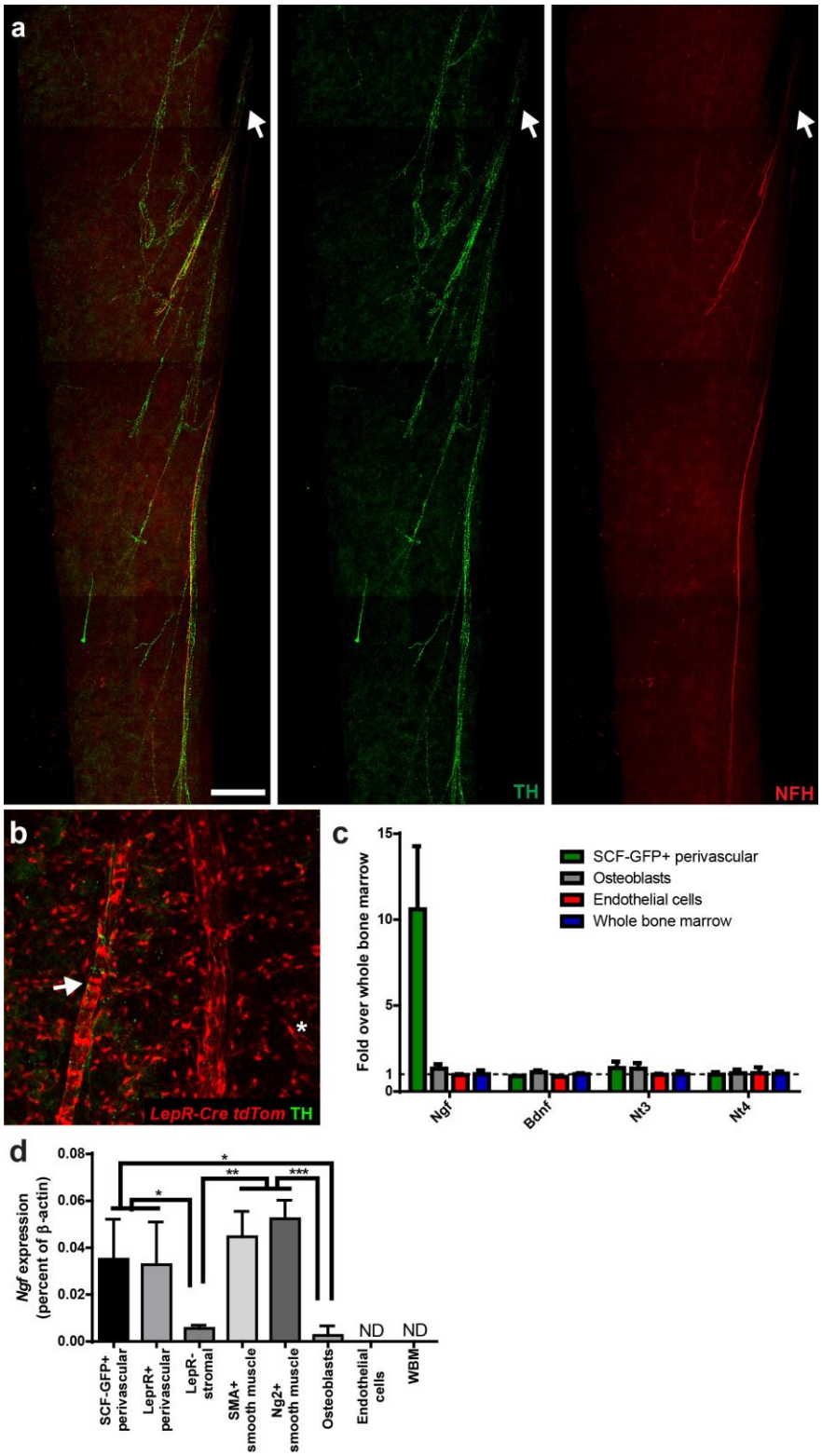

Figure 18: Nerve growth factor produced by perivascular stromal and smooth muscle cells is the primary bone marrow neurotrophin. a, Tyrosine hydroxylase (TH) and Neurofilament H (NFH) staining in longitudinally bisected tibia from wild-type mice. Nerves enter the marrow through a nutrient foramen in the bone (arrow). Image is a maximum projection of a 168μm thick image, scale bar represents 200μm. **b,** Leptin receptor expression (*LepR^{cre}; tdTomato*) marks both periarteriolar cells in close proximity to TH+ nerves (arrow) and perisinusoidal reticular cells (asterisk). **c,** Expression of neurotrophins in various bone marrow populations by microarray. n=3 replicates per population. **d,** Expression of *Ngf* in different marrow populations by quantitative RT-PCR. Expression levels are presented as a percent of actin levels in each cell population. n=3-6 replicates per population. Statistical significance was assessed using one way ANOVA with Tukey's correction for multiple comparisons (*, $P<0.05$; ** $P<0.01$; ***, $P<0.001$).

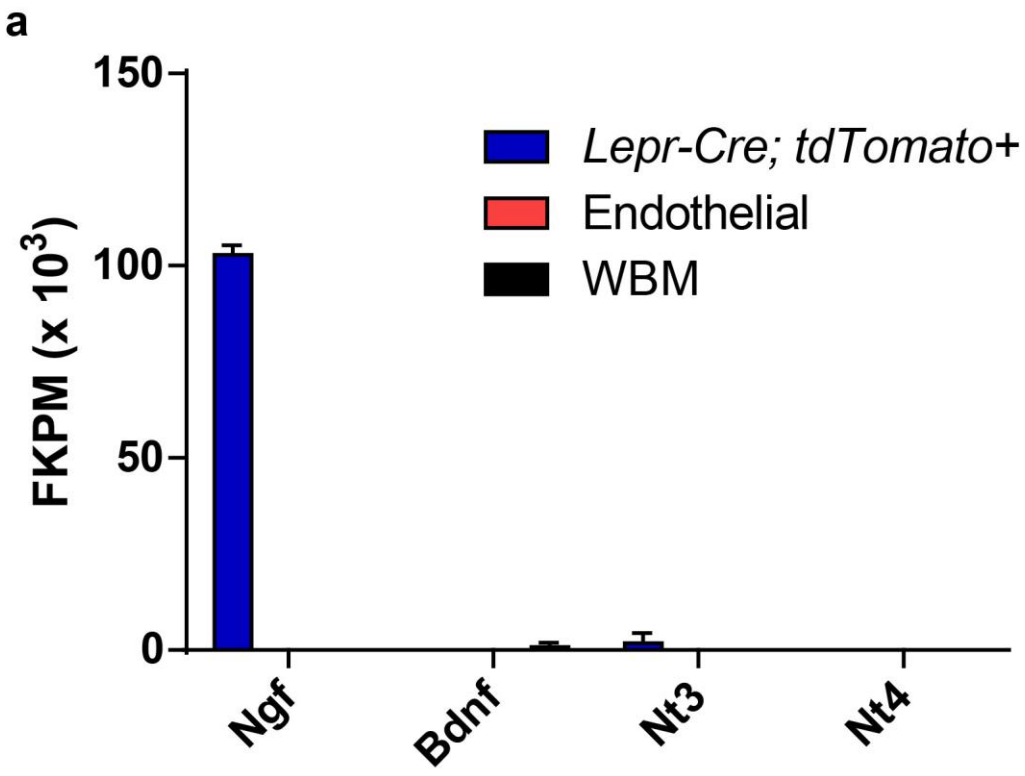

Figure 19: *Ngf* is the only neurotrophin family member expressed in the bone marrow. a, RNA-seq analysis of *LepR^{cre}; tdTomato^{+}* bone marrow cells, endothelial cells, and whole bone marrow showing the expression of the four neurotrophin family members in the bone marrow by FKPM. n=2 samples for each population.

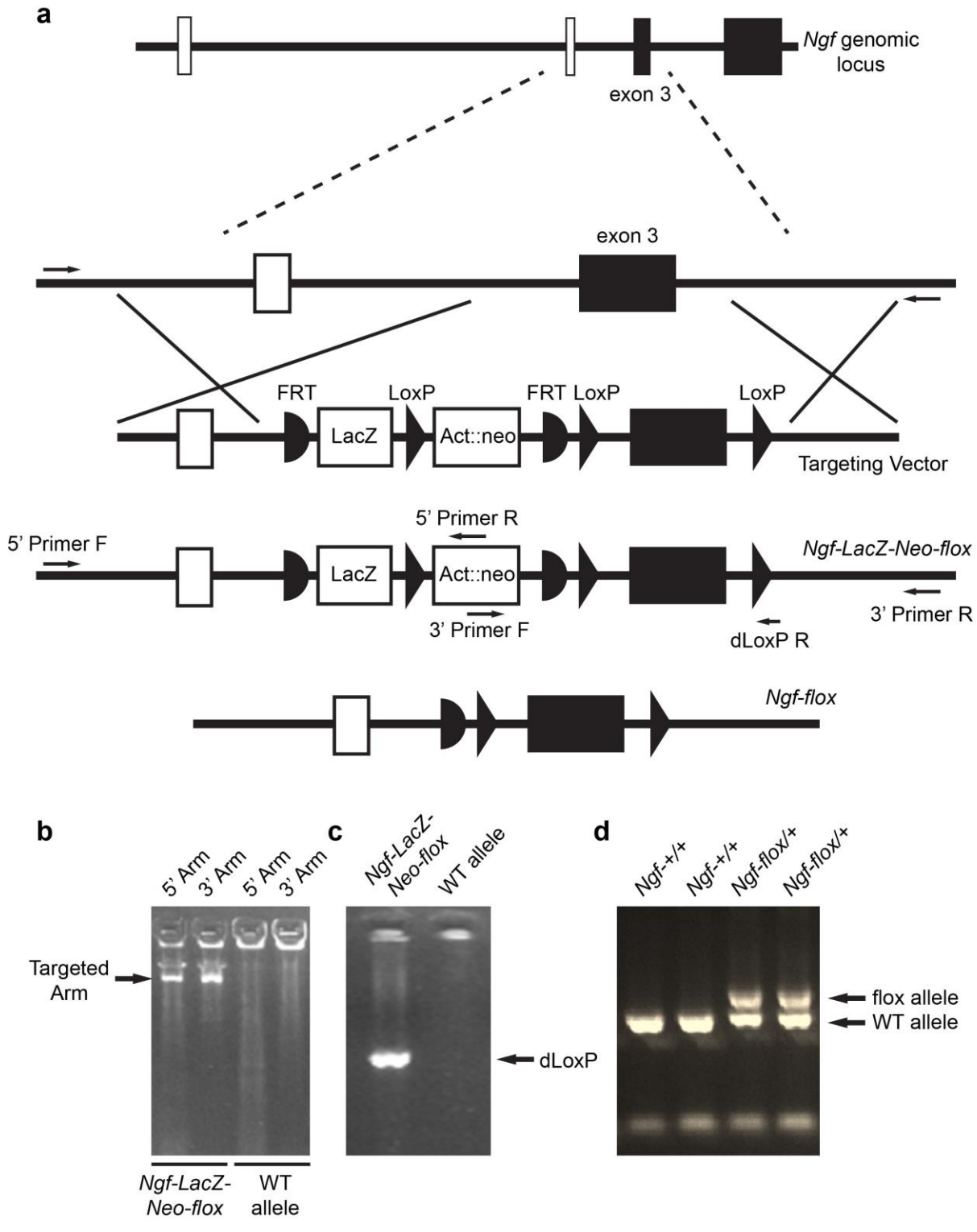
a
Ngf genomic locus
exon 3
exon 3
FRT
LoxP
FRT LoxP
LoxP
LacZ
Act::neo
Targeting Vector
5' Primer R
5' Primer F
LacZ
Act::neo
Ngf-LacZ-Neo-flox
3' Primer R
3' Primer F
dLoxP R
Ngf-flox
b
5' Arm
3' Arm
5' Arm
3' Arm
Targeted Arm
Ngf-LacZ-Neo-flox
WT allele
c
Ngf-LacZ-Neo-flox
WT allele
dLoxP
d
Ngf-+/+
Ngf-+/+
Ngf-flox/+
Ngf-flox/+
flox allele
WT allele

Figure 20: Generation of *Ngf* ^{flox} mice. a, The targeting strategy for generating the *Ngf* ^{flox} allele is shown. The targeting vector was obtained from The European Conditional Mouse Mutagenesis Program (EUCOMM), linearized, and electroporated into C57BL-derived Bruce4 ES cells. **b,** PCRs using primers within the neomycin gene (*neo*) and outside the homology arms were used to verify that the construct was successfully incorporated into the correct location in the genome of ES cells. **c,** The presence of the distal LoxP site (dLoxP) in successfully targeted ES cells was confirmed by PCR using primer sets in *neo* and overlapping with the distal LoxP site. Successfully targeted ES cell clones that retained their distal LoxP site were chosen for chimera generation. Upon confirmation of germ-line transmission by PCR, the *Ngf-LacZ-neo-flox* mice were crossed with *Flpe* mice (Rodríguez et al., 2000) to remove the neomycin resistance and *LacZ* casettes. **d,** PCR genotyping of wild type and heterozygous mice carrying the *Ngf* ^{flox} allele.

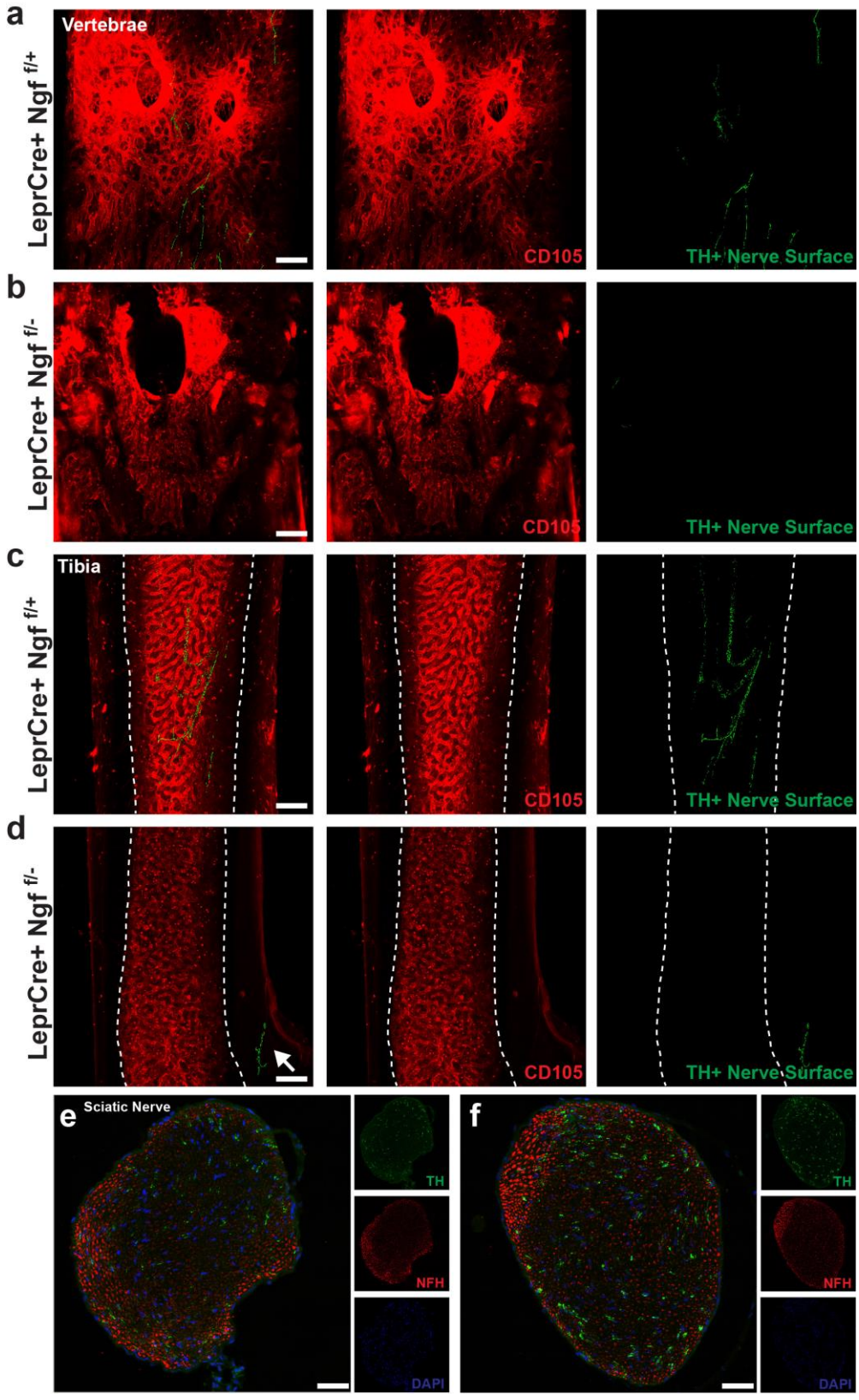
a
Vertebrae
LeprCre+ Ngf fl/+
CD105
TH+ Nerve Surface
b
LeprCre+ Ngf fl/-
CD105
TH+ Nerve Surface
c
Tibia
LeprCre+ Ngf fl/+
CD105
TH+ Nerve Surface
d
LeprCre+ Ngf fl/-
CD105
TH+ Nerve Surface
e
Sciatic Nerve
TH
NFH
DAPI
f
TH
NFH
DAPI

Figure 21: *LepR^{cre};Ngf $^{fl/-}$* conditional knockout mice lack bone marrow innervation. a, Image of TH+ peripheral nerves in vertebral bone marrow. Vasculature is marked by CD105 staining (red) and procedurally identified TH+ sympathetic nerves are digitalized as a 3D surface (green) and shown in an overlay. **b,** Vertebral bone marrow of *LepR^{cre};Ngf $^{fl/-}$* conditional knockout mice show no innervation of vertebral marrow, although small fragments of TH+ nerves can be seen vertebral bone (left side of image). Representative image of n=3 mice analyzed. **c,** Vasculature and innervation of tibial bone marrow. **d,** Tibial bone marrow of adult *LepR^{cre};Ngf $^{fl/-}$* mice with no nerves in the marrow. A nerve can be seen in the nutrient foramen of cortical bone but does not enter the marrow cavity (arrow). Representative image of n=11 mice analyzed. Scale bar in (a-d) represents 200μm. Images are a maximum projection of images (a), 352μm; (b), 136μm; (c), 398μm; and (d), 186μm thick. We also confirmed that mutant mice lacked nerves in their femur as well as tibia (n=3, data not shown). For more information on the penetrance of marrow denervation see Table 1. **e-f,** Both (e) control *LepR^{cre};Ngf $^{fl/+}$* and (f) mutant *LepR^{cre};Ngf $^{fl/-}$* mice have TH and NFH-expressing neurons in their sciatic nerves. Images were taken of thin sections (12μm thick). Scale bar represents 50μm.

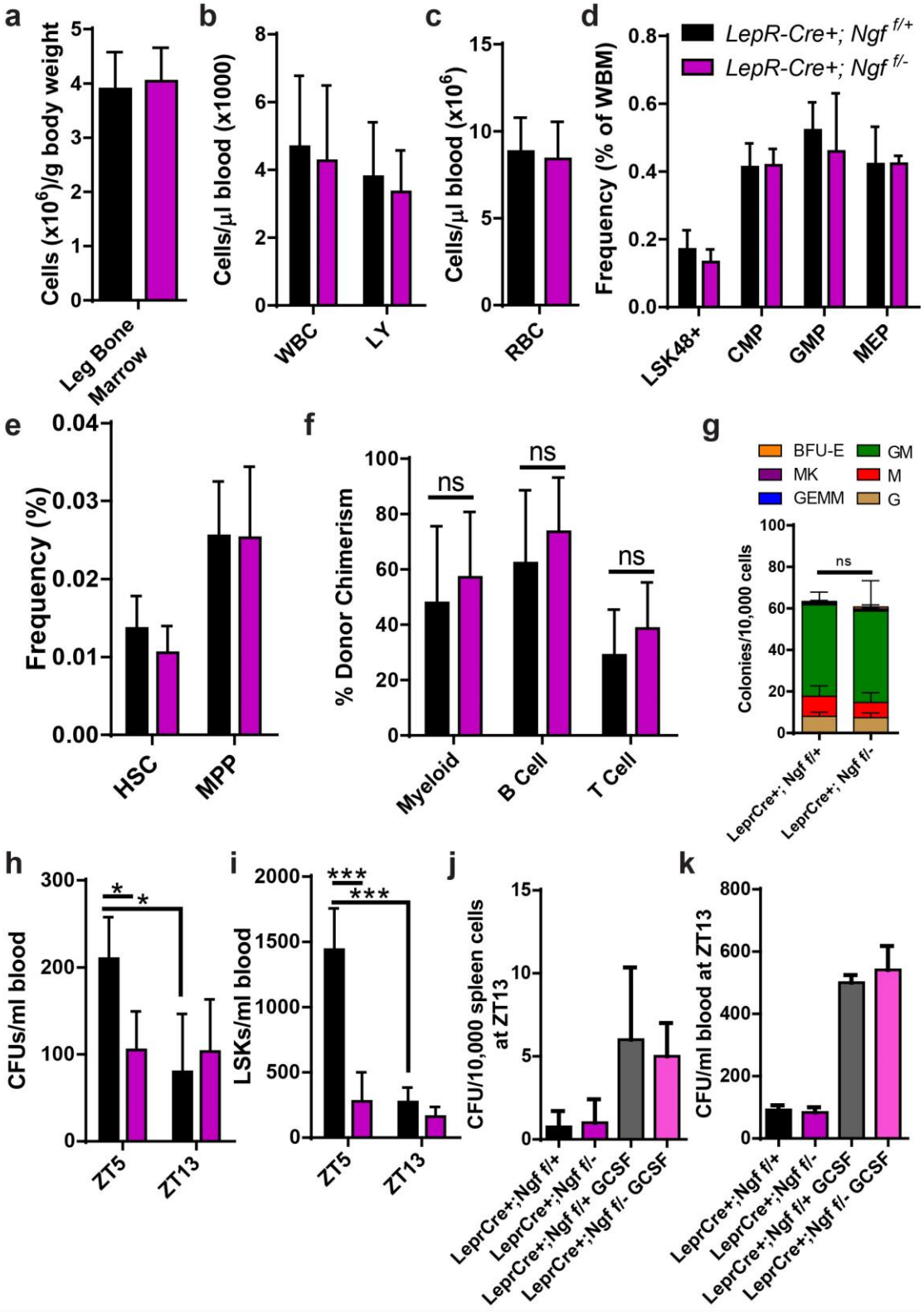
a
Cells (x10^6)/g body weight
Leg Bone Marrow
b
Cells/µl blood (x1000)
WBC
LY
c
Cells/µl blood (x10^6)
RBC
d
LepR-Cre+; Ngf f/+
LepR-Cre+; Ngf f/-
Frequency (% of WBM)
LSK48+
CMP
GMP
MEP
e
Frequency (%)
HSC
MPP
f
% Donor Chimerism
ns
Myeloid
B Cell
T Cell
g
BFU-E
MK
GEMM
GM
M
G
Colonies/10,000 cells
LeprCre+; Ngf f/+
LeprCre+; Ngf f/-
h
CFUs/ml blood
ZT5
ZT13
i
LSKs/ml blood
j
CFU/10,000 spleen cells at ZT13
LeprCre+;Ngf f/+
LeprCre+;Ngf f/-
LeprCre+;Ngf f/+ GCSF
LeprCre+;Ngf f/- GCSF
k
CFU/ml blood at ZT13

Figure 22: *LepR^{cre};Ngf $^{fl/-}$ mice* have no defects in HSC homeostasis, but lack circadian mobilization of progenitors. a, Cellularity of two femurs and two tibiae of *LepR^{cre};Ngf $^{fl/+}$* control mice (black) or *LepR^{cre};Ngf $^{fl/-}$* mutant mice (purple). Data are normalized to body weight to allow males and females to be pooled. Control and mutant mice sharing a gender showed no differences in body weight (data not shown). **b, c,** (b) White blood cell (WBC), lymphocyte (LY), and (c) red blood cell (RBC) counts in the peripheral blood of control and *LepR^{cre};Ngf $^{fl/-}$* mice. Data were gathered at ZT 5-8. n=9 (control) and 4 (mutant). **d,** Frequency of hematopoietic progenitors in the femur and tibia of *LepR^{cre};Ngf $^{fl/+}$* control and *LepR^{cre};Ngf $^{fl/-}$* mutant mice. CMP, Lin-c-kit+CD34+CD16/32-; GMP, Lin-c-kit+CD34+CD16/32-; MEP, Lin-c-kit+CD34-CD16/32-. n=4 mice per group from 3 independent experiments. **e,** Frequency of HSC (LSK, CD48-CD150+) and multipotent progenitors (MPPs, LSK, CD48-CD150-). **f,** Percent donor chimerism of different hematopoietic lineages in the peripheral blood 4 months after transplantation. 200,000 CD45.2+ whole marrow cells from femurs and tibiae of control (black) or *LepR^{cre};Ngf $^{fl/-}$* mutant mice (purple) was mixed with 200,000 whole marrow cells from congenic CD45.1+ donors and transplanted into five CD45.1+/CD45.2+ F1 recipients per donor. n=15 mice per group from 3 independent experiments. **g,** CFU-C from femoral and tibial bone marrow. BFU-E, blast-forming unit, erythrocyte; GM, granulocyte and monocyte; MK, megakaryocyte colony; M, monocyte only; GEMM, granulocyte, erythroid, megakaryocyte, and monocyte; G, granulocyte only. n=3 mice per genotype. Significance assessed both among colony types and total number of colonies. **h,**

Mice lacking marrow nerves do not mobilize progenitors to the blood. CFU-C per milliliter of blood at different Zeitgeber times (ZT5, late morning; ZT13, just after nightfall). All observed colonies were GM. **i,** Abundance of hematopoietic progenitor cells per milliliter of blood at different Zeitgeber times. n=4 mice per group. **j, k,** CFU-C in the (j) spleen and (k) blood of GCSF-treated mice. Mice were treated with saline or G-CSF subcutaneously daily for four days and sacrificed and analyzed on the fifth day at ZT13. All colonies observed in the spleen were GM. n=4-5 mice per group. Statistical significance was assessed using student's t-tests when comparing only two populations and by one way ANOVA with Tukey's correction for multiple comparisons (*, $P<0.05$; **, $P<0.01$; ***, $P<0.001$).

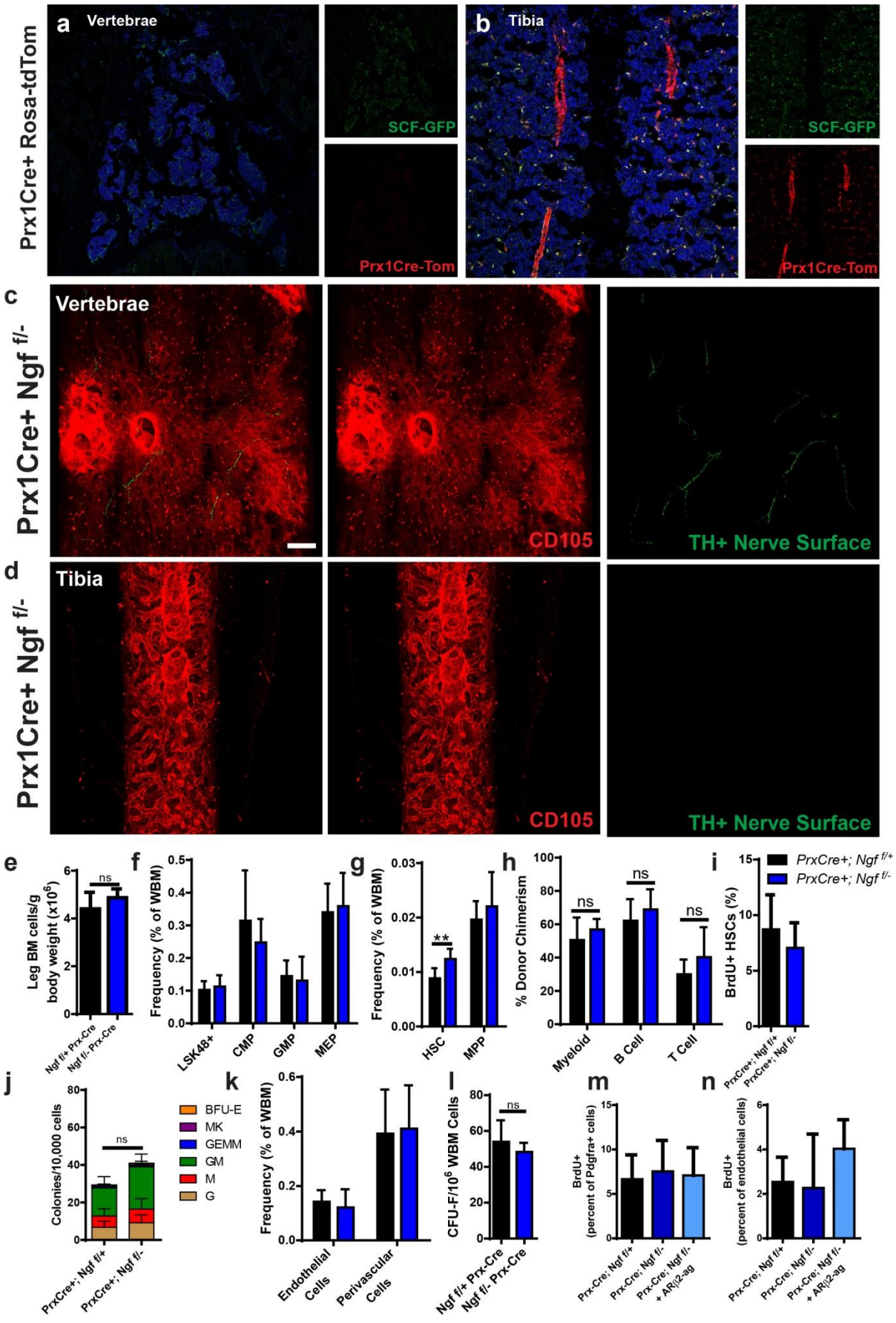
a
Vertebrae
SCF-GFP
Prx1Cre-Tom
Prx1Cre+ Rosa-tdTom
b
Tibia
SCF-GFP
Prx1Cre-Tom
c
Vertebrae
Prx1Cre+ Ngf f/-
CD105
TH+ Nerve Surface
d
Tibia
Prx1Cre+ Ngf f/-
CD105
TH+ Nerve Surface
e
Leg BM cells/g body weight (x10^6)
ns
Ngf f/+ Prx-Cre
Ngf f/- Prx-Cre
f
Frequency (% of WBM)
LSK48+
CMP
GMP
MEP
g
Frequency (% of WBM)
**
HSC
MPP
h
% Donor Chimerism
ns
Myeloid
B Cell
T Cell
i
PrxCre+; Ngf f/+
PrxCre+; Ngf f/-
BrdU+ HSCs (%)
PrxCre+; Ngf f/+
PrxCre+; Ngf f/-
j
Colonies/10,000 cells
ns
PrxCre+; Ngf f/+
PrxCre+; Ngf f/-
k
BFU-E
MK
GEMM
GM
M
G
Frequency (% of WBM)
Endothelial Cells
Perivascular Cells
l
CFU-F/10^6 WBM Cells
ns
Ngf f/+ Prx-Cre
Ngf f/- Prx-Cre
m
BrdU+ (percent of Pdgfra+ cells)
Prx-Cre; Ngf f/+
Prx-Cre; Ngf f/-
Prx-Cre; Ngf f/- + ARβ2-ag
n
BrdU+ (percent of endothelial cells)
Prx-Cre; Ngf f/+
Prx-Cre; Ngf f/-
Prx-Cre; Ngf f/- + ARβ2-ag

Figure 23: *Prx1^{cre}; Ngf $^{fl/-}$* mice lack innervation in long bones but not vertebrae and show no defects in HSC niche components. a, b, Deletion pattern of *Prx1^{cre}; tdTomato* in (a) vertebrae and (b) tibia. SCF-GFP positive cells but not tdTomato positive cells can be observed in the vertebral marrow, while nearly all SCF-GFP+ cells in tibial marrow are tdTomato positive. **c, d,** SNS innervation of (c) vertebral bone marrow but not (d) tibial bone marrow in *Prx1^{cre}; Ngf $^{fl/-}$* mice. Scale bars represent 150μm. Images are maximum projections of (c) 374μm, and (d) 370μm thick images. **e,** Cellularity of tibial and femoral bone marrow in *Prx1^{cre}; Ngf $^{fl/+}$* control (black) or *Prx1^{cre}; Ngf $^{fl/-}$* mutant (blue) mice. n=5 mice. **f,** No changes in the frequency of progenitors in *Prx1^{cre}; Ngf $^{fl/-}$* mice. n=5-7 mice from at least 3 independent experiments. **g,** Slight increase in the frequency of HSCs, but not MPPs in *Prx1^{cre}; Ngf $^{fl/-}$* mice. n=6-14 mice from at least 3 independent experiments. **h,** Relative contribution of *Prx1^{cre}; Ngf $^{fl/+}$* control (black) or *Prx1^{cre}; Ngf $^{fl/-}$* mutant (blue) to peripheral blood lineages of transplanted mice 4 months after transplantation. n=25 mice per group from 5 independent experiments. **i,** Frequency of HSCs that incorporated BrdU during a 24 hour pulse. n=3 mice per group. **j,** CFU-C of 10,000 femur and tibia whole bone marrow cells. n=7-9 mice per group. **k,** Frequency of VE-Cadherin+ endothelial and PDGFRα^+ perivascular cells in leg bones. n=4 mice per group. **l,** CFU-F colonies formed from one million whole bone marrow cells. n=3-4 mice per group. **m, n,** Proportions of (m) VE-Cadherin+ endothelial and (n) PDGFRα^+ perivascular cells in leg bones that incorporate BrdU during a 24 hour pulse. n=3 mice per group. Statistical significance was assessed using student's t-

tests when comparing only two populations and by one way ANOVA with Tukey's correction for multiple comparisons (**, $P<0.01$).

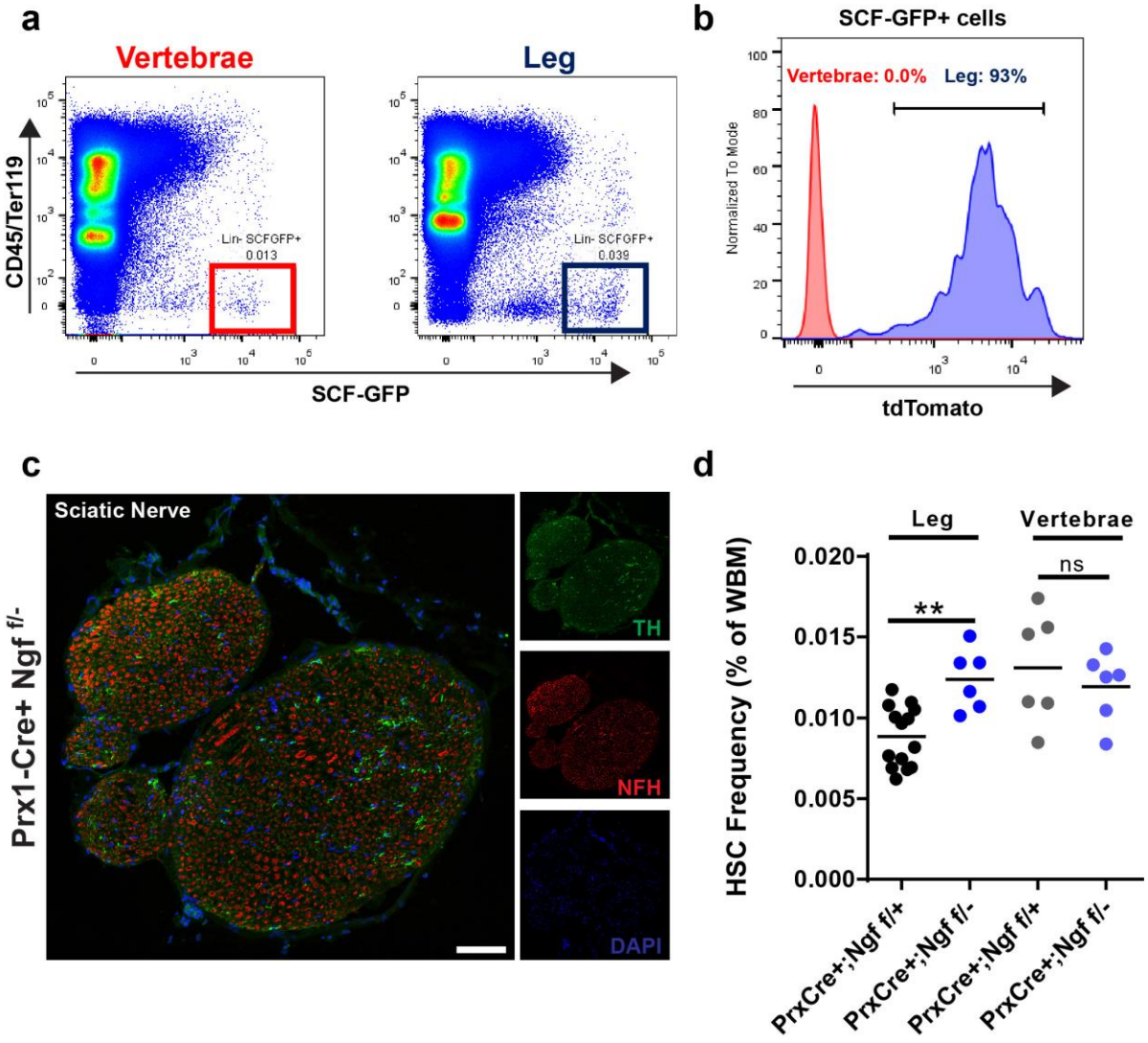
a
Vertebrae
Leg
CD45/Ter119
Lin- SCFGFP+
0.013
Lin- SCFGFP+
0.039
SCF-GFP
b
SCF-GFP+ cells
Vertebrae: 0.0%
Leg: 93%
Normalized To Mode
tdTomato
c
Prx1-Cre+ Ngf f/-
Sciatic Nerve
TH
NFH
DAPI
d
Leg
Vertebrae
ns
**
HSC Frequency (% of WBM)
0.020
0.015
0.010
0.005
0.000
PrxCre+;Ngf f/+
PrxCre+;Ngf f/-
PrxCre+;Ngf f/+
PrxCre+;Ngf f/-

Figure 24: *Prx1-Cre* deletes in leg bones but not vertebrae and *Prx1^{cre}; Ngf $^{fl/-}$* mice have peripheral neurons in their sciatic nerves. a, b, Flow cytometric analysis of digested bone marrow from the vertebrae or leg bones of *Prx1^{cre}; tdTomato; SCF-GFP* mice. (a) SCF-GFP+ CD45/Ter119- perivascular stromal cells can be identified from both vertebrae and leg, (b) but only SCF-GFP+ cells from the leg bones are recombined by *Prx1-Cre* and express tdTomato. **c,** Thin cross section of a sciatic nerve from a *Prx1^{cre}; Ngf $^{fl/-}$* mouse, showing the presence of peripheral neurons (NFH) and sympathetic neurons (TH). **d,** Frequency of HSCs in the leg bones and vertebrae of *Prx1^{cre}; Ngf $^{fl/-}$* mutant mice and littermate controls.

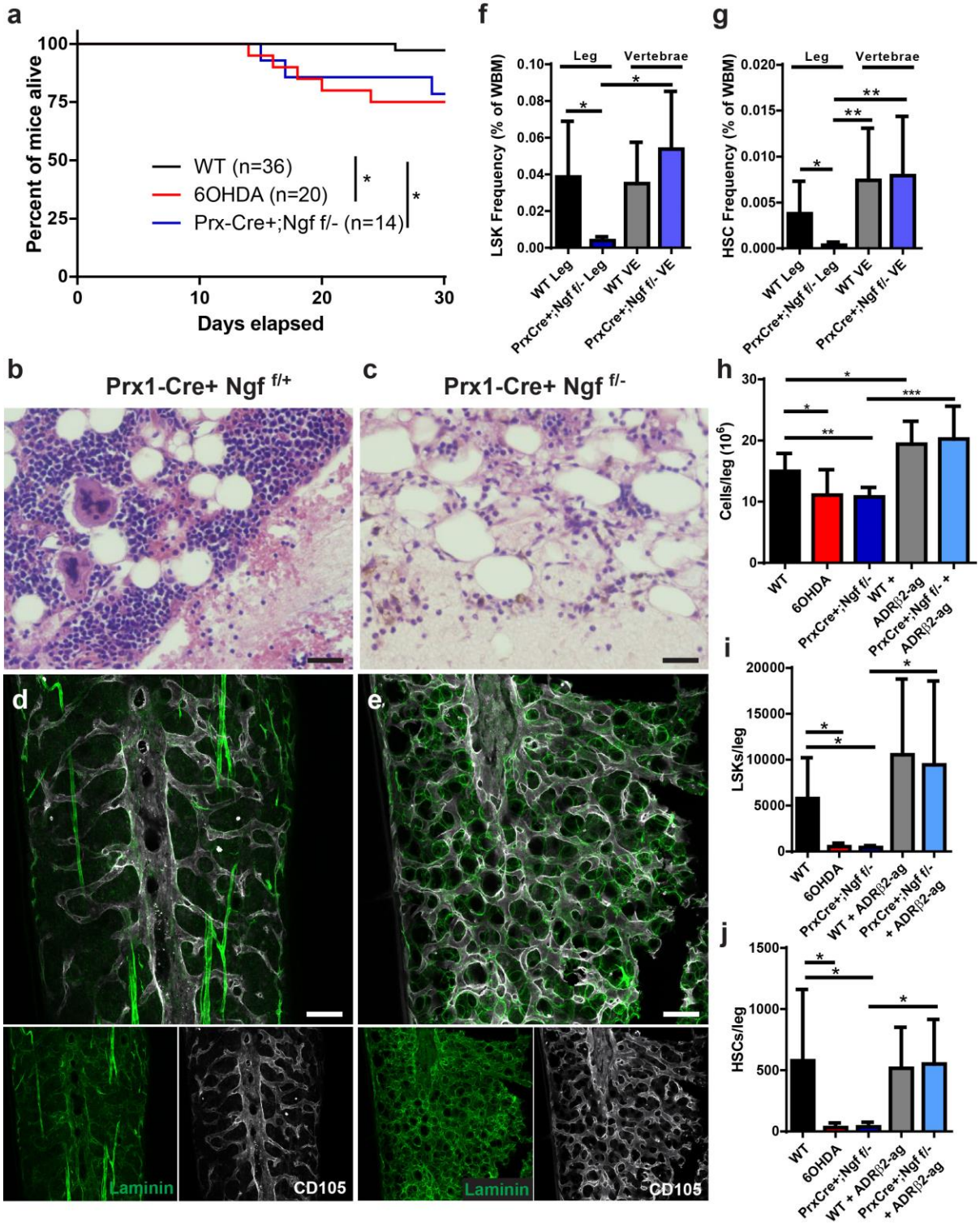
a
Percent of mice alive
Days elapsed
WT (n=36)
6OHDA (n=20)
Prx-Cre+;Ngf f/- (n=14)
f
LSK Frequency (% of WBM)
Leg
Vertebrae
WT Leg
PrxCre+;Ngf f/- Leg
WT VE
PrxCre+;Ngf f/- VE
g
HSC Frequency (% of WBM)
b
Prx1-Cre+ Ngf f/+
c
Prx1-Cre+ Ngf f/-
h
Cells/leg (10^6)
WT
6OHDA
PrxCre+;Ngf f/-
WT + ADRβ2-ag
PrxCre+;Ngf f/- + ADRβ2-ag
i
LSKs/leg
j
HSCs/leg
d
e
Laminin
CD105

Figure 25: *Prx1^{cre}; Ngf $^{fl/-}$* mice require nerve signaling to recover after irradiation and marrow transplantation. a, Survival of wild type (black), 6OHDA-treated (red), and *Prx1^{cre}; Ngf $^{fl/-}$* (blue) recipient mice after receiving 11Gy of X-Ray irradiation and 200,000 whole bone marrow cells from a CD45.1 donor. n=36 control, 20 6OHDA-treated, and 14 *Prx1^{cre}; Ngf $^{fl/-}$* mice. **b, c,** Representative H&E staining of tibial bone marrow of (b) wild-type or (c) *Prx1^{cre}; Ngf $^{fl/-}$* mice 30 days after transplantation. Scale bar represents 50μm. **d, e,** Representative immunofluorescence images of bisected tibiae from (d) *Prx1^{cre}; Ngf $^{fl/+}$* control or (e) *Prx1^{cre}; Ngf $^{fl/-}$* mice 30 days after irradiation stained with antibodies CD105 (white) to mark vasculature and Laminin (green) to mark basement membranes and adipocytes. Scale bars represent 80μm. Images are maximum projections of 22μm thick optical sections. **f, g,** Frequency of (f) LSKs and (g) HSCs in leg or vertebral bone marrow 30 days after transplantation. n=8 control and 5 mutant mice for leg bones, n=3 and 3 mice for vertebrae. **h-j,** Analysis of hematopoiesis 30 days after bone marrow transplantation. (h) Total cellularity, (i) absolute numbers of LSKs, and (j) absolute numbers of HSCs per one femur and one tibia in wild-type control (n=21), 6OHDA-treated (n=13), *Prx1^{cre}; Ngf $^{fl/-}$* mutant mice (n=8), and wild-type (n=5) or mutant (n=4) mice that received the β2AR agonist salbutamol. Statistical significance was assessed using a Mantel-Cox test for differences in survival after injury and one way ANOVA with Tukey's correction for multiple comparisons (*, $P<0.05$; **, $P<0.01$; ***, $P<0.001$).

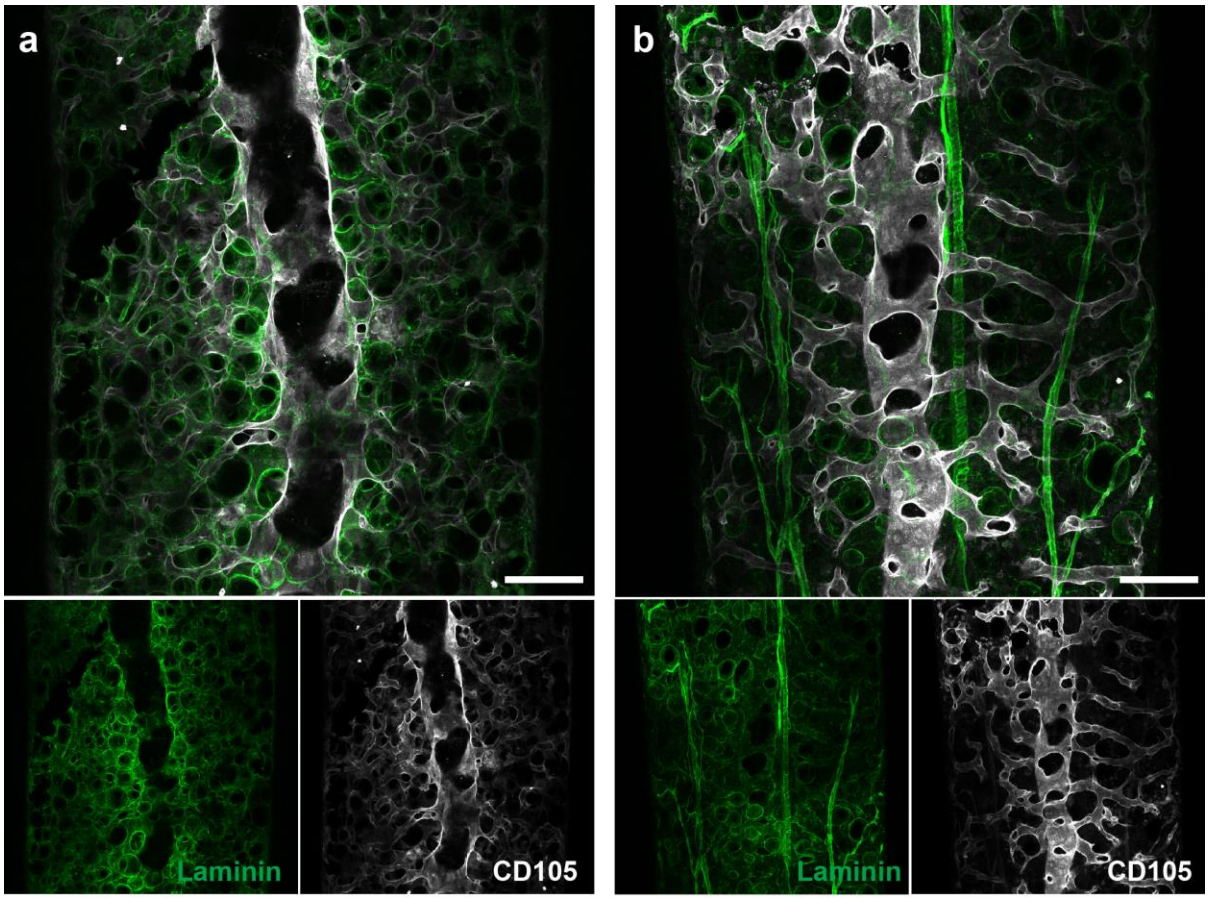
a
b
Laminin
CD105
Laminin
CD105

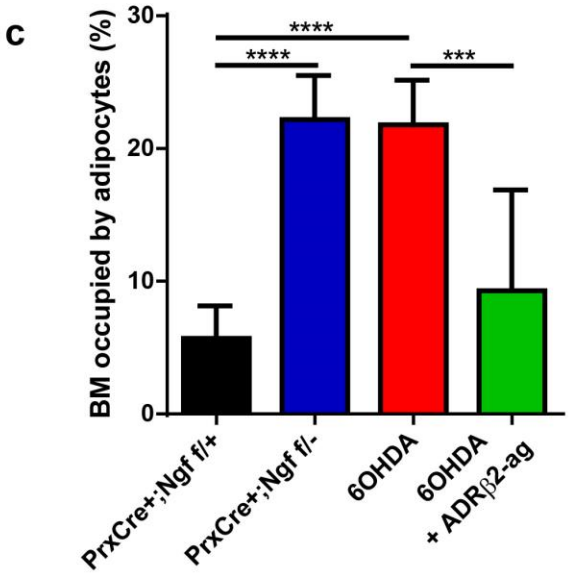
c
BM occupied by adipocytes (%)
30
20
10
0
****
****
***
PrxCre+;Ngf f/+
PrxCre+;Ngf f/-
6OHDA
6OHDA
+ ADRβ2-ag

Figure 26: β adrenergic receptor agonist salbutamol rescues marrow adiposity after injury. a, b, Representative immunofluorescence images of bisected tibiae from (a) 6OHDA-treated or (b) 6OHDA-treated mice that received 14 days of salbutamol injections after irradiation analyzed 30 days after irradiation and stained with antibodies CD105 (white) to mark vasculature and Laminin (green) to mark basement membranes and adipocytes. Scale bars represent 80μm. Images are maximum projections of 22μm thick optical sections. **c,** Quantification of bone marrow adiposity. The proportion of bone marrow area within single optical sections 2μm thick occupied by adipocytes was calculated using the area measurement function in ImageJ. At least 5 optical sections per mouse and two mice were analyzed for each population. Statistical significance was assessed using one way ANOVA with Tukey's correction for multiple comparisons (***, $P<0.001$; ****, $P<0.0001$).

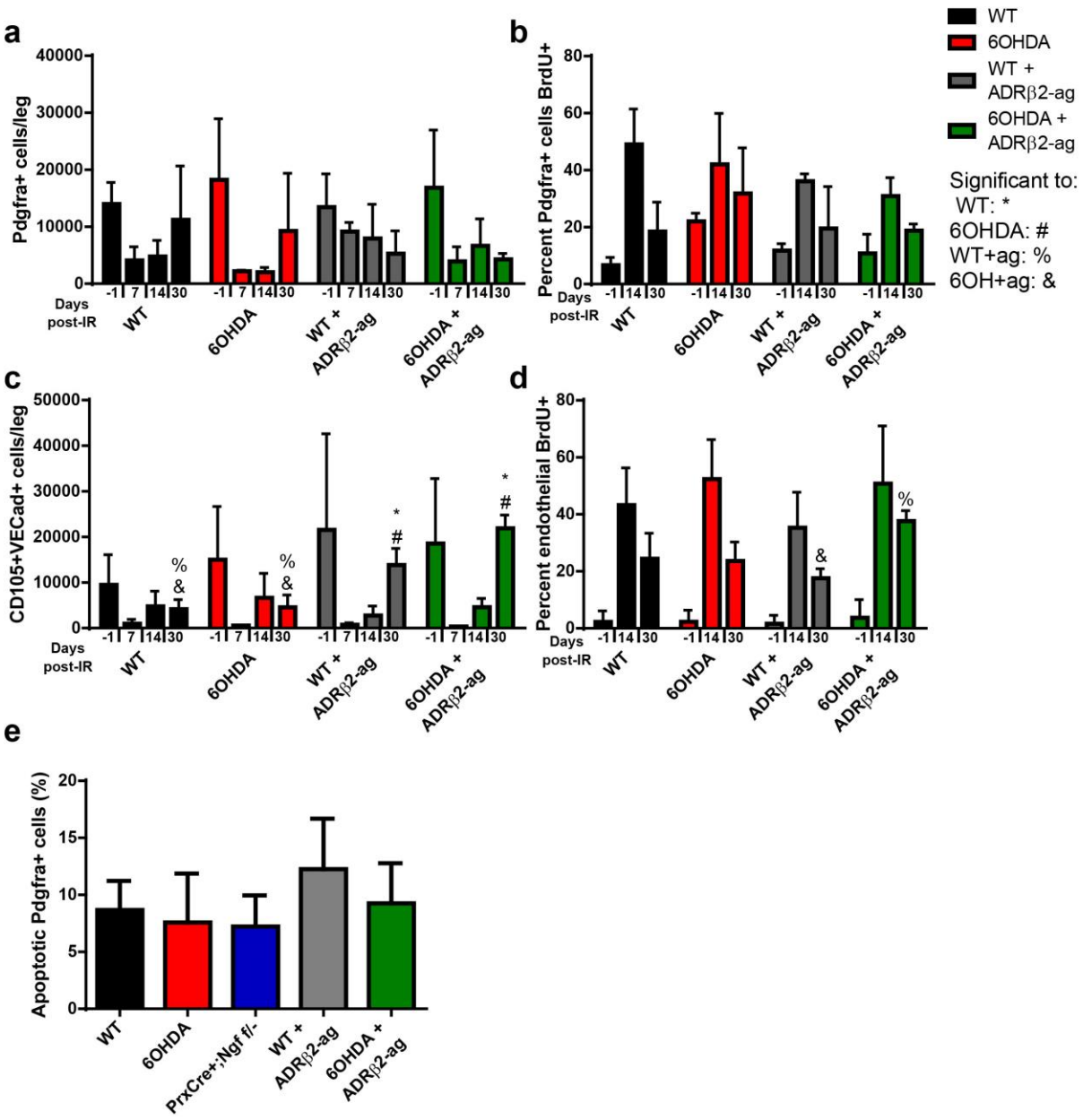
a
Pdgfra+ cells/leg
40000
30000
20000
10000
0
Days post-IR
-1 7 14 30
WT
6OHDA
WT + ADRβ2-ag
6OHDA + ADRβ2-ag
b
Percent Pdgfra+ cells BrdU+
80
60
40
20
0
-1 14 30
WT
6OHDA
WT + ADRβ2-ag
6OHDA + ADRβ2-ag
WT
6OHDA
WT + ADRβ2-ag
6OHDA + ADRβ2-ag
Significant to:
WT: *
6OHDA: #
WT+ag: %
6OH+ag: &
c
CD105+VECad+ cells/leg
50000
40000
30000
20000
10000
0
%
&
*
#
d
Percent endothelial BrdU+
80
60
40
20
0
%
&
e
Apoptotic Pdgfra+ cells (%)
20
15
10
5
0
WT
6OHDA
PrxCre+;Ngf f/-
WT + ADRβ2-ag
6OHDA + ADRβ2-ag

Figure 27: Peripheral nerve loss does not induce changes in HSC niche cell frequency, proliferation, or apoptosis after irradiation. a, c, Absolute numbers of (a) PDGFRα^+ perivascular stromal cells and (c) CD105$^+$;VE-Cadherin$^+$ endothelial cells in one femur and one tibia of untreated (WT) or 6OHDA-treated mice that received either saline or salbutamol (ADRβ2-ag) daily for 14 days following irradiation and transplantation. Mice were analyzed in steady state 6h after a saline or salbutamol injection (-1), and also 7, 14, or 30 days after irradiation. **b, d,** Proportions of (b) perivascular and (d) endothelial cells that incorporate BrdU after a 24 hour pulse at different time points after irradiation. (a-d) n=4-8 mice per group in at least 3 independent experiments. For statistical analysis, each population was compared to the other three populations at the same time point using ANOVA. Statistical significance to each other population was marked as follows: *, significant to WT; #, significant to 6OHDA; %, significant to WT+ADRβ2-ag; &, significant to 6OHDA+ADRβ2-ag. These data indicate that while there are no significant changes between WT and 6OHDA-treated mice, treating mice with ADRβ2-ag after irradiation does enhance the speed of endothelial cell recovery. **e,** Frequency of live PDGFRα^+ cells that stain positive for a fluorescent marker of activated caspase-3 by flow cytometry. All mice were analyzed at 30 days after irradiation. n=3 mice per group. Statistical significance was assessed using one way ANOVA with Tukey's correction for multiple comparisons (one symbol, $P<0.05$).

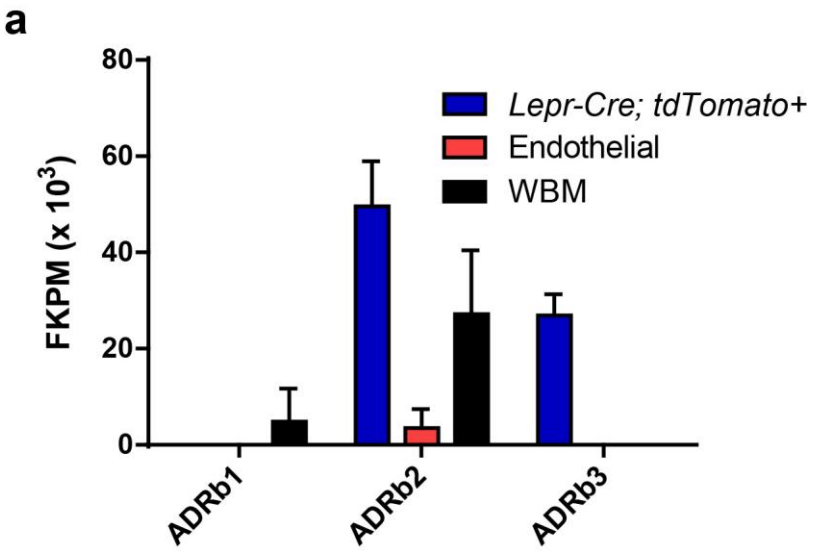

Figure 28: β adrenergic receptor expression in the bone marrow. a, Expression level of the three β adrenergic receptors in perivascular leptin receptor-expressing cells, endothelial cells, and whole bone marrow cells by RNA-seq (as in Figure 1). ADRβ2 is expressed by both hematopoietic and perivascular cells, whereas ADRβ3 is expressed exclusively by perivascular cells in the bone marrow.

Genotype	Age Range	Mice with Tibia Nerves
LepR-Cre; Ngf f/-	6-12 wks	4/4
LepR-Cre; Ngf f/-	16-50 wks	2/11
Prx-Cre; Ngf f/-	6-12 wks	0/14
Prx-Cre; Ngf f/-	20-30 wks	4/5

Table 1: Penetrance of nerve loss in long bones of *Ngf* conditional mutant mice. The genotypes, ages, and frequency of nerve loss in *Ngf* conditional mutants is reported. Young *LepR-Cre* mutants have nerves, but lose them when the deletion of *LepR-Cre* becomes high. Young *Prx1-Cre* mutants have no nerves, since *Prx1-Cre* deletes during early development, but the nerves regenerate in most older *Prx1-Cre* mutant mice.

CHAPTER FOUR
Conclusions and future directions

4.1 Identification of the HSC niche

HSCs function in dynamic microenvironments, capable of entering the blood, moving to the spleen, and visiting other bones during hematopoietic homeostasis. Because HSCs can occupy distinct tissues with only some features in common (abundant *Scf* and *Cxcl12* expression in both the marrow and spleen, for example), it seems unlikely that there is a single unique microenvironment designed to maintain HSCs but not occupied by other types of cells. While the work that I present in this dissertation shows that HSCs have biases in their distributions towards the central marrow, and are nearly all located in close proximity to *LepR*-expressing perivascular cells as well as sinusoidal endothelial cells, for every HSC in these locations there are ten thousand non-HSCs. While future work identifying the spatial distributions of extracellular matrix proteins, cytokines, or previously unknown sub-populations of *LepR*-expressing cells may help us further define the optimal microenvironment for HSCs, our data suggest that HSCs do not reside in the same sort of niche that Schofield hypothesized in 1978. Schofield's niche was a unique environment for HSCs that determined whether a cell was an HSC or a progenitor cell. Only a cell within its niche could be an HSC, and once it left it would become a multipotent progenitor (MPP).

Abandoning parts of Schofield's niche hypothesis leaves us with a number of unresolved questioned which must be answered to understand the biology of the hematopoietic system.

What signals do HSCs respond to that progenitors do not? This could be through the accessibility of those signals (i.e. only a cell in the niche receives the signal, as Schofield hypothesized) or through the sensing of those signals, such as distinct receptors on HSCs versus MPPs. Identification of HSC-specific receptors is a very active field, and HSC-specific sensing mechanisms identified in the future should be mapped to ligand distributions within the bone marrow to see if specific receptor-ligand pairs can define rare bone marrow microenvironments.

How do HSCs regulate their cell number in the absence of a defined, rare niche? One of the most appealing notions of Schofield's niche is that it explains why we have so few stem cells. There can only be as many stem cells as there are niches, so when niches shrink or expand, stem cells differentiate or self-renew, respectively. If HSCs only rely on abundant or widely diffusing signals in the bone marrow for their maintenance, however, how are their numbers maintained? Why do almost all mice have similar frequencies of HSCs in their marrow, and why do those numbers return to their original values after BMT? One interesting observation from our work is that HSCs tend to be quite spatially distinct. With the exception of HSCs that have recently divided, most stem cells in the bone marrow are located quite distant from one another. This raises the possibility that HSCs could regulate their own frequency by negatively regulating other HSCs. A secreted protein or metabolite

produced by HSCs could induce chemorepulsion or the differentiation of HSCs in its immediate environment. This would allow HSCs to remain rare among bone marrow cells, despite the signals required for their maintenance and self-renewal being abundant.

4.2 Role of Nerves in hematopoiesis

The data I have presented in this dissertation are the first definitive experiments examining the role of bone marrow nerves in regulating hematopoiesis, and showing that bone marrow nerves are critical for the recovery of hematopoiesis after irradiation. However, how the nerves regulate hematopoiesis is not clear. My work raises a number of questions about the function of bone marrow nerves.

4.2.1 What cells cause innervation of the bone marrow?

Previous work implicated arteriolar Nestin transgene-expressing cells as the target cells of nerve signaling. We show that *Ngf* is expressed by both perivascular stromal and periarteriolar smooth muscle cells (the cells that express high levels of the *Nestin*-GFP transgene), and use *Cre* lines that delete in both of these populations. Thus, we cannot determine from our experiments whether only one or both of these populations are required to maintain innervation. Yamazaki and Allen describe efferent nerve terminals on both reticular and smooth muscle cells in their early studies of bone marrow innervation, but future work will have to be done to determine whether both of these cell types are functionally important for maintaining

nerves. We are currently crossing our *Ngf* conditional mutant mice to *SMA-CreER* mice, so that we can conditionally delete *Ngf* from smooth muscle cells but not perisinusoidal cells. If these mice lack peripheral innervation, then the periarteriolar smooth muscle cells are necessary for maintaining nerves in the bone marrow.

4.2.2 What cells marrow cells receive signals from the nerves?

Yamazaki and Allen performed the first landmark study in 1990 of what they dubbed the "neuro-reticular complex." They observed that the majority of bone marrow neurons formed efferent terminals on smooth muscle cells close to the artery, but a substantial minority also formed efferent terminals on reticular cells. Now that we and others have defined multiple populations of bone marrow stromal cells using fluorescent markers, we need to determine what fraction of nerve terminals are on *LepR*-, *NG2*-, or *SMA*-expressing cells, as well as other populations of bone marrow cells. To accomplish this, we plan on performing correlative fluorescence and electron microscopy, where we will embed bone marrow from a fluorescent reporter mouse in low melting point agarose, image the nerves and stromal cells in the mouse, and then take scanning electron microscopy images of serial sections of that bone marrow. We will then find innervated cells in the electron microscopy images, and map them to the fluorescent images (as done by Tamplin and colleagues to identify zebrafish HSCs (Tamplin et al., 2015)) to determine the frequency of nerve terminals on different stromal cell populations.

4.2.3 How are signals from the nerves transmitted throughout the marrow?

Nestin-GFP-expressing periarteriolar cells are not important sources of HSC maintenance factors (Ding and Morrison, 2013; Ding et al., 2012), nor are HSCs closely associated with nerve fibers or arterioles (Açar et al., 2015). Therefore, the connection between nerves and HSCs (especially in the context of regeneration, where nerves are required for successful healing) is not clear. Norepinephrine signaling from catecholiminergic neurons is very short range, believed to act only in the vicinity of the efferent nerve terminal (Esler et al., 1990; Schroeder and Jordan, 2012); therefore, a number of hypotheses can be constructed about the relationship between nerves and hematopoietic regeneration.

4.2.3.1 HSCs are regulated by nerve-induced signals in stromal cells that diffuse through the marrow.

To begin testing this hypothesis, we plan to perform RNA-seq analysis of regenerating bone marrow in wild-type and nerve-compromised mice after administering BMTs. By finding factors produced during normal regeneration, absent in mice lacking nerves, and rescued by salbutamol administration, we hope to identify signaling pathways that rely on peripheral innervation and are responsible for regeneration of the bone marrow after injury.

4.2.3.2 Nerve signals are transmitted throughout the bone marrow by a reticular cell network.

An interesting hypothesis regarding the transmission of nerve signals is that signals from the nerves reach the HSCs through a network of reticular cells that span the whole marrow. MSCs derived from adipose tissue respond to norepinephrine with an increase in calcium ion (Ca^{2+}) flux (Kotova et al., 2014). In this study, MSCs exhibited a positive feedback loop for calcium signaling: transmission of the signal through the cells happened much faster than predicted by diffusion. It is possible that MSCs can relay signals through the bone marrow using a positive feedback loop of calcium signaling. To investigate this hypothesis, we plan to study the nerve-induced regulation of calcium signaling in bone marrow stromal cells. To begin with, we will test whether perivascular cells initiate calcium signaling in response to β adrenergic receptor stimulation by placing beads coated in adrenergic receptor agonist in live bone marrow preparations of mice transgenic for a fluorescent reporter of calcium signaling. We can then see in real time whether cells close to the bead have more active Ca^{2+} signaling than those further away. Secondly, we can test whether nerve signaling propagates a calcium signal. Using a calcium signaling detector and a channel rhodopsin transgenic mouse, in which peripheral nerve signaling can be turned on by exposure to blue light, we can force the nerves of live bone marrow preparations to fire, and then record the calcium fluctuations in responding cells near the peripheral nerve. These studies will help us determine whether the nerve can directly induce a coordinated signal in a large number of connected perivascular cells.

4.2.3.3 HSCs are indirectly regulated through altered cell fates of stromal cells.

One striking observation of our studies is that nerveless mice have large numbers of adipocytes in their bone marrow after injury. Leptin receptor-expressing cells are mesenchymal stem cells, so one possible mechanism for the role of nerves in regeneration is that in the absence of nerves, MSCs into adipocytes after injury. However, we did not observe a difference in the frequency or the proliferative status of MSCs in nerveless mice after injury, suggesting that these cells are neither lost nor more proliferative. However, a possibility remains that a progenitor for adipocytes downstream of MSCs rapidly proliferates and produces large numbers of adipocytes in the context of injury and sympathectomy. This hypothesis cannot be directly tested at this time, however, since markers for bone marrow adipocyte progenitors have not been identified.

4.2.3.4 HSCs are regulated indirectly by other nerve-influenced cells.

Existing data supports the idea that nervous system regulation of HSCs may be indirect. Neutrophils enter the bone marrow to be recycled in accordance with a circadian pattern, which may be a cause of circadian HSC mobilization (Casanova-Acebes et al., 2013), and G-CSF-mediated mobilization is known not to act through HSCs directly, but by influencing other hematopoietic populations in the bone marrow (Molineux et al., 2012). Therefore it is possible that the failure of hematopoietic recovery is not due to any deficiency in signaling to the HSCs, but to another cell population regulated by nerves that plays a role in either regulating

HSCs or recovering after marrow injury. The most promising cell population to test this hypothesis is megakaryocytes. Megakaryocytes produce platelets, which are crucial for early stage regeneration during bone marrow transplantation. Release of platelets by megakaryocytes is regulated by sympathetic nerve signaling in a circadian pattern (Ozdemir et al., 2004), and megakaryocytes have recently been suggested to directly regulate HSC maintenance (Bruns et al., 2014).

4.2.3.5 HSCs localize close to arterioles during regeneration, so are especially susceptible to nerve signaling during this time.

The possibility that HSC localization changes after injury is remarkably difficult to test, because the markers we use to identify HSCs in bone marrow images, c-kit and α-catulin, change after injury. This makes it impossible to rule out the possibility that HSCs reside close to arterioles and nerve fibers in the regenerating marrow. However, some evidence of *ex vivo*-labeled HSCs transplanted into mice and visualized shortly afterwards suggests that HSCs tend to localize near the endosteum in the first few days after injury (Lo Celso et al., 2009; Sipkins et al., 2005), not arterioles.

4.3 Final remarks

We began to study the niche based on the promise of being able to indefinitely culture HSCs, but the more we learn about the niche, the further from that goal we seem to be. HSC maintenance is a multifaceted process. They cannot

divide too quickly or they lose stem cell potential; they require some specific signals to survive, but the signals we know of are not sufficient to maintain HSCs in culture; they require the bone marrow environment to prosper, but we have been unable to identify clear landmarks in the bone marrow that give us further clues to the regulation of HSC maintenance. The next breakthrough in this field would be the identification of a protein, ECM structure, metabolite, or cell population that is both rare and highly co-localized with HSCs. It is my hope that the lasting value of my work will be that fewer groups will expend effort looking for these structures in the wrong places, around nerves, arterioles, or osteoblasts, and concentrate their efforts on identifying heterogeneity in perisinusoidal regions that distinguish HSC microenvironments from others. Regardless of the degree to which Schofield's niche hypothesis is true for HSCs, there is still much for us to learn about the HSC's microenvironment so that we might recreate it for the benefit of patients.

APPENDIX A
Quantitative analysis of three dimensional tissue images

A.1 Introduction

My primary contribution to the work presented in Chapter 2 of this dissertation was figuring out how to learn something from three dimensional reconstructions of bone marrow that we could not from lots of discontinuous two dimensional sections. A number of incredible technical innovations over the past five or so years, such as CLARITY and 3DISCO have allowed researchers to create amazing three dimensional images, but there is almost no follow-up work that has generated novel insights from these images: they are just (incredibly) pretty pictures. I became interested in the spatial distribution of stem cells in images after presenting a paper about the topic from Paul Frenette's group to the rest of the laboratory. While analyzing the paper, I realized that Frenette made a serious error in mapping the distribution of HSCs away from the bone surface. He reported only absolute distances of HSCs from the bone, which led him to the conclusion that HSCs are enriched at the bone surface despite the fact that there is much more marrow volume five microns from the bone (in the outermost marrow) than fifty microns from the bone (in the middle of the bone marrow).

A.2 Volumes as distributions

This observation started me thinking about the bone marrow as a series of distributions from various landmarks. For any given cell type or structure in the bone marrow, we wanted to know if stem cells were closer to or further from that landmark than would be predicted by a random distribution. Measuring this required two technical innovations apart from simply identifying and digitalizing bone marrow landmarks (a task undertaken by Malea Murphy and me).

A.2.1 Defining marrow boundaries

Before I could do any sort of mathematics involving the distribution of volumes within the marrow, I had to define the marrow space. The simplest unit of a confocal image is the voxel, which is simply a series of numbers at a specific location in a three dimensional grid, representing the intensity of fluorescence in various channels at that point. I needed to teach a computer program to differentiate between voxels that contained bone marrow and voxels that did not. To accomplish this I developed a method to generate a new channel that did not represent fluorescent intensities, but instead was a signifier of whether that voxel was a part of the bone marrow (given a value 1) or lay outside of it (given the value 0). This was accomplished by generating a digital volume that occupied the entire image except for locations that had any fluorescent signal, then setting the voxels within the surface to 0 and voxels outside that surface to 1 in an artificially generated new channel.

A.2.2 Creating a percentile distribution of volumes

For voxels within the bone marrow, I now added another artificial channel on top of the image. In this channel, each voxel was given an intensity value that corresponded to the distance that voxel was from a defined bone marrow landmark, a process called a Distance Transformation (DT) in Imaris. I wrote a program to read the DT distances from every voxel within the bone marrow and assemble them into a list tens of millions of entries long. I ranked this list according to the distances, then binned it into 100 different bins, each one representing $1/100^{th}$ of the voxels in the bone marrow, or one percentile of the marrow volume. I output the maximum values in each of the 100 bins to a spreadsheet file. The values in this file represent the percent of bone marrow volume within a given distance from a landmark (this code and an example of this output file is included in Appendix B).

A.3 Utility of percentile distributions for analyzing three dimensional images

There are two major reasons to use this tool to evaluate three dimensional images. Firstly, it is a tool to generate accurate three dimensional distributions within a tissue. Randomly distributed cells would fall along this distribution in the bone marrow. We used these distributions to confirm that the set of random spots we generated to compare to our HSC distributions did in fact represent a random distribution. Secondly, it allows for the identification of zones of enrichment within three dimensional spaces, a concept which has the potential to untangle the complexity of multifaceted microenvironmental interactions. The most substantial

difference in the localization of HSCs that we discovered in our work was between the inner marrow, where HSCs are comparatively abundant, and outer marrow, where HSCs are comparatively scarce. As we identify new landmarks in the bone marrow that have distributional biases for HSCs, this tool can be used as part of a combinatorial approach to identify zones that are enriched for HSCs in respect to multiple different landmarks, identify the overlap between these zones, and thereby narrow down the location in which HSCs are highly enriched in order to study what it is about that zone in the bone marrow that makes it a suitable niche for HSCs.

APPENDIX B
COMPUTER PROGRAMS USED FOR ANALYSIS OF STEM CELL DISTRIBUTION IN THREE DIMENSIONAL IMAGES

B.1 Binning voxels into percentiles of bone marrow volume according to their distance from a landmark.

```
%
%
%  Peyer_binVoxels for Imaris 7.7.1
%
%  Copyright James Peyer 2015
%
%  Installation:
%
%  - Copy this file into the XT\matlab folder in the Imaris
installation directory.
%  - Set the value of aXls in this file to specify the
location you want to save the table this program generates
%  - You will find this function in the Image Processing menu
%
%    <CustomTools>
%      <Menu>
%        <Item name="Peyer_binVoxels" icon="Matlab"
tooltip="Bins voxel intensity into equal parts.">
%          <Command>MatlabXT::Peyer_binVoxels(%i)</Command>
%        </Item>
%      </Menu>
%    </CustomTools>
%
%
%  Description:
%
%   Returns the percentile intensities of voxels in a specific
channel.
%
%

function Peyer_binVoxels(aImarisApplicationID, aExcludeZero)
```

```
% connect to Imaris interface
if ~isa(aImarisApplicationID, 'Imaris.IApplicationPrxHelper')
    javaaddpath ImarisLib.jar
    vImarisLib = ImarisLib;
    if ischar(aImarisApplicationID)
        aImarisApplicationID =
round(str2double(aImarisApplicationID));
    end
    vImarisApplication =
vImarisLib.GetApplication(aImarisApplicationID);
else
    vImarisApplication = aImarisApplicationID;
end

%
% Set the lower bound.
% A value of 0 here means that all voxels >=0 will be counted.
% A value greater than 0 means that voxels less than the
entered value will be ignored.
% This is useful because you only want break the parts of the
image that represent tissue into percentiles.
%

vThreshold = 0;
if nargin == 1
   vAnswer = inputdlg({'Exclude Voxels less than'}, 'Peyer
binVoxels', 1, {'1'});
   if ~isempty(vAnswer)
       vThreshold = str2double(vAnswer(1));
   else
       return;
   end
elseif nargin == 2
    if aExcludeZero
        vThreshold = 3;
    end
end

%
% Set the upper bound.
% A value of 0 here means that there will be no upper bound.
```

```
% A value greater than 0 means that voxels greater than the
entered value will be ignored.
% This is useful because you only want break the parts of the
image that represent tissue into percentiles.
% This can be useful if you want to include voxels with a
value of 0 (e.g. overlapping the surfaces), but still have
regions to exclude.
% So mask the area that does not represent tissue to a value
of 255,
% then run Peyer binVoxels from 0 to 255 to exclude all the
voxels equal to 255 (i.e. the ones that do not represent
tissue).
%

vUpperThreshold = 0;
if nargin == 1
   vUpperAnswer = inputdlg({'Exclude Voxels greater than'},
'Peyer binVoxels', 1, {'255'});
   if ~isempty(vUpperAnswer)
       vUpperThreshold = str2double(vUpperAnswer(1));
   else
       return;
   end
elseif nargin == 2
    if aExcludeZero
        vUpperThreshold = 0;
    end
end

%
% Select the Channel of interest on which to make the surfaces
% The top channel in the Imaris display is Channel 1, then 2,
and so on.
%

vSurfaceChannel = 0;
if nargin == 1
   vSurfaceChannelAnswer = inputdlg({'Select the channel to
make volumetric surfaces'}, 'Peyer binVoxels', 1, {'1'});
   disp(vSurfaceChannelAnswer);
   vSurfaceChannel = str2double(vSurfaceChannelAnswer);
   disp(vSurfaceChannel);
elseif nargin == 2
    if aExcludeZero
        vSurfaceChannel = 1;
```

```
    end
end

% Select the number of equal volumes that you wish to divide
the channel into
% Standard here is 100, to give the value for each 1% of
volume.
vNumberVolumes = 0;
if nargin == 1
   vNumberVolumesAnswer = inputdlg({'Select the number of
equal volumes to divide the channel into'}, 'Peyer_binVoxels',
1, {'100'});
   vNumberVolumes = str2double(vNumberVolumesAnswer);
elseif nargin == 2
    if aExcludeZero
        vNumberVolumes = 10;
    end
end

% Start Waitbar
vProgressDisplay = waitbar(0,'Peyer binVoxels');


% fetch 1d array data from open Imaris file for the selected
channel.
% For large images, it is common to get a memory overload.
% Try converting a distance transformation to 8 bits before
running Peyer binVoxels if you get memory overloads.

if strcmp(vImarisApplication.GetDataSet.GetType,'eTypeUInt8')
             vImage =
vImarisApplication.GetDataSet.GetDataVolumeAs1DArrayBytes( ...
                         vSurfaceChannel-1,0);
                   disp('8 bit image');
            vImage = typecast(vImage,'uint8');
            vImage = double(vImage);
        elseif strcmp(vImarisApplication.GetDataSet.GetType,
'eTypeUInt16')
            vImage =
vImarisApplication.GetDataSet.GetDataVolumeAs1DArrayShorts(
...
                        vSurfaceChannel-1,0);
                   disp('16 bit image');
            vImage = double(vImage);
```

```
        elseif strcmp(vImarisApplication.GetDataSet.GetType,
'eTypeFloat')
            vImage =
vImarisApplication.GetDataSet.GetDataVolumeAs1DArrayFloats(
...
                        vSurfaceChannel-1,0);
                    disp('32 bit image');
            vImage = double(vImage);
end
% display the normal maximum and minimum of the data received
disp(max(vImage));
disp(min(vImage));
% reshape the 1d array to exclude pre-defined minimum and
maximum values
if vUpperThreshold == 0
     vDataVector = vImage((vImage>=vThreshold));
     else
          vDataVector = vImage((vImage>=vThreshold) &
(vImage<vUpperThreshold));
end
% Reshape the vector and display the new maximum and minimum
values.
vDataVector = reshape(vDataVector,1,[],1);
disp(max(vDataVector));
disp(min(vDataVector));

% Create the boundaries for the table.
% The first column will be the percents of volume, the second
column will be the voxel intensities
vBins(1:101,1) = 0;
vBins(1:101,2) = vThreshold;
vVoxels = size(vDataVector);
nVox = num2str(vVoxels);
disp(['Number of Voxels being analyzed: ' nVox]);
% Put the total number of voxels analyzed in the table
vBins(1,3:4) = vVoxels;
int64 i=1;
for i = 1:vNumberVolumes
    vBins(i+1,1) = (100*i/vNumberVolumes);
     waitbar(i/vNumberVolumes,vProgressDisplay);
    i=i+1;
end
Y = vBins (2:vNumberVolumes+1,1);
disp(isvector(Y));
Z = reshape(Y,1,[]);
```

```
disp(isvector(Z));
dZ = double(Z);
disp(isvector(dZ));
prcs = prctile(vDataVector,dZ);
disp(prcs);
vBins(2:vNumberVolumes+1,2) = prcs;

% The program will create a save file with the name of a
channel in the folder you specify
% EACH USER MUST MANUALLY SET THE FOLDER LOCATION IN THIS
PROGRAM BY CHANGING THE VALUE FOR "aXls"
aChName =
char(vImarisApplication.GetDataSet.GetChannelName(vSurfaceChan
nel-1));
% Change the value of aXls to specify a save location. You can
copy the directory and paste it over the
% "C:\Users\Public\Documents\" portion of aXls
aXls = ['C:\Users\Public\Documents\Percentiles_' aChName
'.xlsx'];
xlswrite(aXls,vBins);
disp(['Data saved to ' aXls]);

close(vProgressDisplay);
```

B.1.2 Example of output of above program.

Marrow Percentile	*Distance to bone (microns)*		*Total Marrow Voxels*
0	0		6.23E+08
1	1		
2	2		
3	3		
4	4		
5	5		
6	6		
7	7		
8	8		
9	9		
10	9		
11	11		
12	11		
13	13		

14	13		
15	15		
16	15		
17	17		
18	17		
19	18		
20	19		
21	21		
22	21		
23	22		
24	23		
25	25		
26	25		
27	27		
28	28		
29	29		
30	30		
31	31		
32	32		
33	33		
34	34		
35	35		
36	36		
37	38		
38	39		
39	40		
40	41		
41	42		
42	43		
43	45		
44	46		
45	47		
46	48		
47	49		
48	51		
49	52		
50	53		
51	55		
52	56		
53	57		

54	58		
55	60		
56	61		
57	62		
58	64		
59	65		
60	67		
61	68		
62	70		
63	71		
64	72		
65	74		
66	75		
67	77		
68	79		
69	80		
70	82		
71	83		
72	85		
73	87		
74	89		
75	90		
76	92		
77	94		
78	96		
79	98		
80	100		
81	102		
82	104		
83	106		
84	109		
85	111		
86	113		
87	116		
88	118		
89	121		
90	124		
91	127		
92	130		
93	134		
94	137		
95	141		

96	146		
97	151		
98	158		
99	168		
100	201		

Table 2: Example output of "Peyer_binVoxels."

B.2.1 Separating bone marrow volume into progressive shells.

```
%
%
%  Peyer_binVoxels for Imaris 7.7.1
%
%  Copyright James Peyer 2015
%
%  Installation:
%
%  - Copy this file into the XT\matlab folder in the Imaris
installation directory.
%  - Set the value of aXls in this file to specify the
location you want to save the table this program generates
%  - You will find this function in the Image Processing menu
%
%    <CustomTools>
%      <Menu>
%        <Item name="Peyer_createShellChannels" icon="Matlab"
tooltip="Uploads channels of equal volumes according to
percentiles.">
%
<Command>MatlabXT::Peyer_createShellChannels(%i)</Command>
%        </Item>
%      </Menu>
%    </CustomTools>
%
%
%  Description:
%
%   Creates a series of concentric shells of equal volumes
radiating away from an Imaris surface.
%
%
```

```
function Peyer_createShellChannels(aImarisApplicationID,
aExcludeZero)

% connect to Imaris interface
if ~isa(aImarisApplicationID, 'Imaris.IApplicationPrxHelper')
    javaaddpath ImarisLib.jar
    vImarisLib = ImarisLib;
    if ischar(aImarisApplicationID)
        aImarisApplicationID =
round(str2double(aImarisApplicationID));
    end
    vImarisApplication =
vImarisLib.GetApplication(aImarisApplicationID);
else
    vImarisApplication = aImarisApplicationID;
end

%
% Set the lower bound.
% A value of 0 here means that all voxels >=0 will be counted.
% A value greater than 0 means that voxels less than the
entered value will be ignored.
% This is useful because you only want break the parts of the
image that represent tissue into percentiles.
%

vThreshold = 0;
if nargin == 1
   vAnswer = inputdlg({'Exclude Voxels less than'}, 'Peyer
binVoxels', 1, {'1'});
   if ~isempty(vAnswer)
       vThreshold = str2double(vAnswer(1));
   else
       return;
   end
elseif nargin == 2
    if aExcludeZero
        vThreshold = 3;
    end
end

%
% Set the upper bound.
% A value of 0 here means that there will be no upper bound.
```

```
% A value greater than 0 means that voxels greater than the
entered value will be ignored.
% This is useful because you only want break the parts of the
image that represent tissue into percentiles.
% This can be useful if you want to include voxels with a
value of 0 (e.g. overlapping the surfaces), but still have
regions to exclude.
% So mask the area that does not represent tissue to a value
of 255,
% then run Peyer Peyer_createShellChannels from 0 to 255 to
exclude all the voxels equal to 255 (i.e. the ones that do not
represent tissue).
%

vUpperThreshold = 0;
if nargin == 1
   vUpperAnswer = inputdlg({'Exclude Voxels greater than'},
'Peyer Peyer_createShellChannels', 1, {'255'});
   if ~isempty(vUpperAnswer)
       vUpperThreshold = str2double(vUpperAnswer(1));
   else
       return;
   end
elseif nargin == 2
    if aExcludeZero
        vUpperThreshold = 0;
    end
end

%
% Select the Channel of interest on which to make the surfaces
% The top channel in the Imaris display is Channel 1, then 2,
and so on.
%

vSurfaceChannel = 0;
if nargin == 1
   vSurfaceChannelAnswer = inputdlg({'Select the channel to
make volumetric surfaces'}, 'Peyer Peyer_createShellChannels',
1, {'1'});
   disp(vSurfaceChannelAnswer);
   vSurfaceChannel = str2double(vSurfaceChannelAnswer);
   disp(vSurfaceChannel);
elseif nargin == 2
    if aExcludeZero
```

```
        vSurfaceChannel = 1;
    end
end

% Select the number of equal volumes that you wish to divide
the channel into
% Standard here is 100, to give the value for each 1% of
volume.
vNumberVolumes = 0;
if nargin == 1
   vNumberVolumesAnswer = inputdlg({'Select the number of
equal volumes to divide the channel into'},
'Peyer_createShellChannels', 1, {'10'});
   vNumberVolumes = str2double(vNumberVolumesAnswer);
elseif nargin == 2
    if aExcludeZero
        vNumberVolumes = 10;
    end
end

try

vImarisApplication.DataSetPushUndo('Peyer_createShellChannels'
);
catch er
  % nothing to do
  er.message;
end

try
  % get the data set
  vDataSet = vImarisApplication.GetDataSet.Clone;

catch er
  msgbox(['Invalid dataset\n\n', er.message])
  return
end

% Get DataSet
% Convert the image into 8 bit first to avoid memory
overloads.
vProgressDisplay = waitbar(0,'Peyer createShellChannels');

 if strcmp(vDataSet.GetType,'eTypeUInt8')
```

```
            vImage =
typecast(vDataSet.GetDataVolumeAs1DArrayBytes( ...
                vSurfaceChannel-1, 0), 'uint8');
            vImage = typecast(vImage,'uint8');
            vImage = double(vImage);
        elseif strcmp(vDataSet.GetType, 'eTypeUInt16')
            msgbox(['First Convert Dataset to 8bit
integers!\n\n', er.message]);
        elseif strcmp(vDataSet.GetType, 'eTypeFloat')
            msgbox(['First Convert Dataset to 8bit
integers!\n\n', er.message]);
 end

 aX = vImarisApplication.GetDataSet.GetSizeX;
 aY = vImarisApplication.GetDataSet.GetSizeY;
 aZ = vImarisApplication.GetDataSet.GetSizeZ;

 vDataSet3d = reshape(vImage,aX,aY,aZ);

        % display the normal maximum and minimum of the data
received
          disp(max(vImage));
          disp(min(vImage));
          % reshape the 1d array to exclude pre-defined
minimum and maximum values
          if vUpperThreshold == 0
               vDataVector = vImage((vImage>=vThreshold));
               else
                    vDataVector = vImage((vImage>=vThreshold)
& (vImage<vUpperThreshold));
          end
          disp(max(vDataVector));
          disp(min(vDataVector));

        vBins(1:101,1) = 0;
        vBins(1:101,2) = vThreshold;

    % Clone the DataSet to put in the new Intensities
        vNewDataSet = vDataSet3d;
          int64 i=1;
        for i = 1:vNumberVolumes
            waitbar(i/vNumberVolumes,vProgressDisplay);

            vBins(i+1,1) = (100*i/vNumberVolumes);
```

```
            vBins(i+1,2) =
prctile(vDataVector,(100*i/vNumberVolumes));

            % Set values between the last and current shell as
1 in
            % NewDataSet. Other Values become 0
            vNewDataSet((vDataSet3d<(vBins(i,2))) |
(vDataSet3d>=(vBins(i+1,2))))=0;
            vNewDataSet((vDataSet3d>=(vBins(i,2))) &
(vDataSet3d<(vBins(i+1,2))))=1;
            aMin = int2str(vBins(i,2));
            aMax = int2str(vBins(i+1,2));

            % Create a new channel where the result will be
sent
            vNumberOfChannels =
vImarisApplication.GetDataSet.GetSizeC;

vImarisApplication.GetDataSet.SetSizeC(vNumberOfChannels + 1);
            shellNum = int2str(i);
            aCName = ['Shell ' shellNum ' - ' aMin ' to '
aMax];
            disp(aCName);

vImarisApplication.GetDataSet.SetChannelName(vNumberOfChannels
,aCName);

vImarisApplication.GetDataSet.SetChannelColorRGBA(vNumberOfCha
nnels, 255*256*256);

            %Set the values of vNewDataSet as the intensities
of the new
            %channel

            if aY > 3000
                vSet = vNewDataSet(:,1:1500,:);

vImarisApplication.GetDataSet.SetDataSubVolumeBytes(vSet,0, 0,
0, vNumberOfChannels,0);
                aStatus = ['Shell ' shellNum ' part 1
written.'];
                disp(aStatus);
                vSet2 = vNewDataSet(:,1501:3000,:);
```

```
vImarisApplication.GetDataSet.SetDataSubVolumeBytes(vSet2,0,
1500, 0, vNumberOfChannels,0);
                aStatus = ['Shell ' shellNum ' part 2
written.'];
                disp(aStatus);
                vSet3 = vNewDataSet(:,3001:end,:);

vImarisApplication.GetDataSet.SetDataSubVolumeBytes(vSet3,0,
3000, 0, vNumberOfChannels,0);
                aStatus = ['Shell ' shellNum ' part 3
written.'];
                disp(aStatus);
            else

vImarisApplication.GetDataSet.SetDataVolumeBytes(vNewDataSet,v
NumberOfChannels,0);
            end
            i=i+1;

        end

% The program will create a save file with the name of a
channel in the folder you specify
% EACH USER MUST MANUALLY SET THE FOLDER LOCATION IN THIS
PROGRAM BY CHANGING THE VALUE FOR "aXls"
aChName =
char(vImarisApplication.GetDataSet.GetChannelName(vSurfaceChan
nel-1));
% Change the value of aXls to specify a save location. You can
copy the directory and paste it over the
% "C:\Users\Public\Documents\" portion of aXls
aXls = ['C:\Users\Public\Documents\Percentiles_' aChName
'.xlsx'];
xlswrite(aXls,vBins);
disp(['Data saved to ' aXls]);


close(vProgressDisplay);
```

B.2.2 Example of output of Peyer_createShellChannels program.

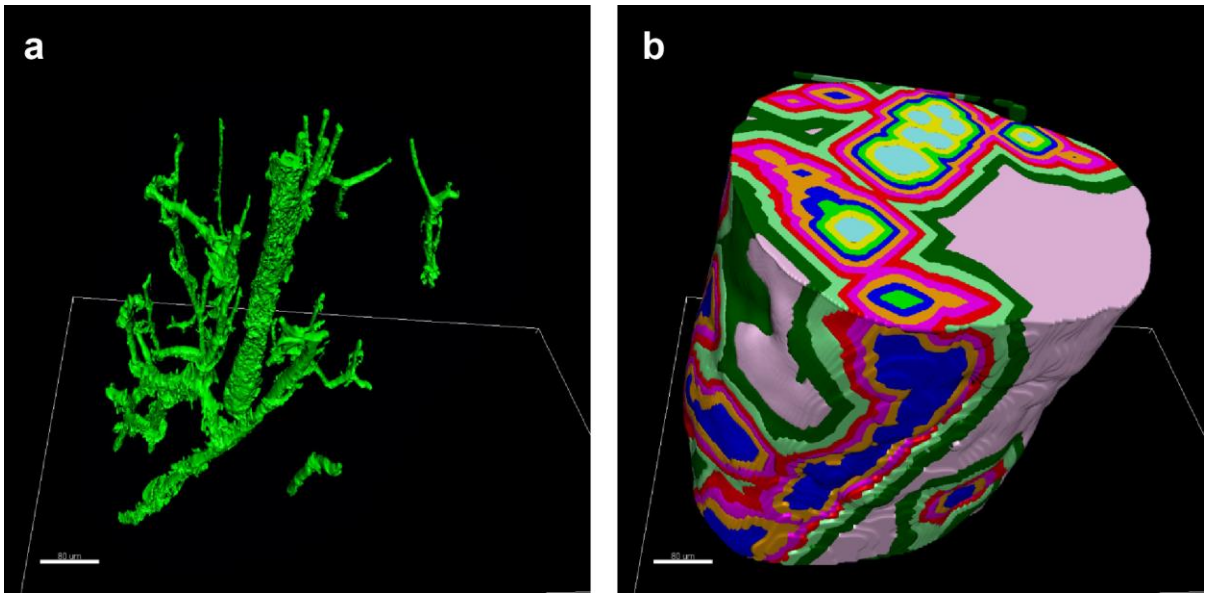

Figure 29: Creation of progressive shells around a bone marrow landmark. a, Manually created digital surface of bone marrow arterioles. A distance transformation from this surface was fed into the program in B.2.1. **b,** Output of the above program. Each color represents 10% of the total bone marrow volume. The 10% of marrow volume closest to the arterioles is in teal, the volume furthest from the arterioles is in pink. Scale bar represents 80 microns.

BIBLIOGRAPHY

Açar, M., Kocherlakota, K.S., Murphy, M.M., Peyer, J.G., Oguro, H., Inra, C.N., Jaiyeola, C., Zhao, Z., Luby-Phelps, K., and Morrison, S.J. (2015). Deep imaging of bone marrow shows non-dividing stem cells are perisinusoidal. Nature *Submitted*.

Afan, A.M., Broome, C.S., Nicholls, S.E., Whetton, A.D., and Miyan, J.A. (1997). Bone marrow innervation regulates cellular retention in the murine haemopoietic system. Br. J. Haematol. *98*, 569–577.

Aloe, L., Rocco, M.L., Bianchi, P., and Manni, L. (2012). Nerve growth factor: from the early discoveries to the potential clinical use. J. Transl. Med. *10*, 239.

Ara, T., Tokoyoda, K., Sugiyama, T., Egawa, T., Kawabata, K., and Nagasawa, T. (2003). Long-term hematopoietic stem cells require stromal cell-derived factor-1 for colonizing bone marrow during ontogeny. Immunity *19*, 257–267.

Arai, F., Hirao, A., Ohmura, M., Sato, H., Matsuoka, S., Takubo, K., Ito, K., Koh, G.Y., and Suda, T. (2004). Tie2/angiopoietin-1 signaling regulates hematopoietic stem cell quiescence in the bone marrow niche. Cell *118*, 149–161.

Arranz, L., Sánchez-Aguilera, A., Martín-Pérez, D., Isern, J., Langa, X., Tzankov, A., Lundberg, P., Muntión, S., Tzeng, Y.-S., Lai, D.-M., et al. (2014). Neuropathy of haematopoietic stem cell niche is essential for myeloproliferative neoplasms. Nature.

Avecilla, S.T., Hattori, K., Heissig, B., Tejada, R., Liao, F., Shido, K., Jin, D.K., Dias, S., Zhang, F., Hartman, T.E., et al. (2004). Chemokine-mediated interaction of hematopoietic progenitors with the bone marrow vascular niche is required for thrombopoiesis. Nat. Med. *10*, 64–71.

Barker, J.N., Weisdorf, D.J., DeFor, T.E., Blazar, B.R., McGlave, P.B., Miller, J.S., Verfaillie, C.M., and Wagner, J.E. (2005). Transplantation of 2 partially HLA-matched umbilical cord blood units to enhance engraftment in adults with hematologic malignancy. Blood *105*, 1343–1347.

Becker, K., Jährling, N., Saghafi, S., Weiler, R., and Dodt, H.-U. (2012). Chemical clearing and dehydration of GFP expressing mouse brains. PLoS One *7*, e33916.

Becker, K., Jährling, N., Saghafi, S., and Dodt, H.-U. (2013). Immunostaining, dehydration, and clearing of mouse embryos for ultramicroscopy. Cold Spring Harb. Protoc. *2013*, 743–744.

Billingham, R.E., Brent, L., and Medawar, P.B. (1953). Actively acquired tolerance of foreign cells. Nature *172*, 603–606.

Blaese, R.M., Culver, K.W., Miller, A.D., Carter, C.S., Fleisher, T., Clerici, M., Shearer, G., Chang, L., Chiang, Y., Tolstoshev, P., et al. (1995). T lymphocyte-directed gene therapy for ADA- SCID: initial trial results after 4 years. Science *270*, 475–480.

Boitano, A.E., Wang, J., Romeo, R., Bouchez, L.C., Parker, A.E., Sutton, S.E., Walker, J.R., Flaveny, C. a, Perdew, G.H., Denison, M.S., et al. (2010). Aryl Hydrocarbon Receptor Antagonists Promote the Expansion of Human Hematopoietic Stem Cells. Science *1345*.

Bowman, T. V, and Zon, L.I. (2009). Lessons from the Niche for Generation and Expansion of Hematopoietic Stem Cells. Drug Discov. Today. Ther. Strateg. *6*, 135–140.

Bruns, I., Lucas, D., Pinho, S., Ahmed, J., Lambert, M.P., Kunisaki, Y., Scheiermann, C., Schiff, L., Poncz, M., Bergman, A., et al. (2014). Megakaryocytes regulate hematopoietic stem cell quiescence through CXCL4 secretion. Nat. Med.

C.W. Bill Young Cell Transplantation Program (2015). HRSA Report on Hematopoietic Stem Cell Transplantation.

Calvi, L.M., Adams, G.B., Weibrecht, K.W., Weber, J.M., Olson, D.P., Knight, M.C., Martin, R.P., Schipani, E., Divieti, P., Bringhurst, F.R., et al. (2003). Osteoblastic cells regulate the haematopoietic stem cell niche. Nature *425*, 841–846.

Calvo, W., and Forteza-Vila, J. (1969). On the development of bone marrow innervation in new-born rats as studied with silver impregnation and electron microscopy,. Am. J. Anat. *126*, 355–371.

Carmen, I.H. (1985). Cloning and the Constitution: An Inquiry into Governmental Policymaking and Genetic Experimentation. (Madison: University of Wisconsin Press).

Carpenter, A.T.C. (1975). Electron microscopy of meiosis in Drosophila melanogaster females. Chromosoma *51*, 157–182.

Cartier, N., Hacein-Bey-Abina, S., Bartholomae, C.C., Veres, G., Schmidt, M., Kutschera, I., Vidaud, M., Abel, U., Dal-Cortivo, L., Caccavelli, L., et al. (2009). Hematopoietic stem cell gene therapy with a lentiviral vector in X-linked adrenoleukodystrophy. Science *326*, 818–823.

Casanova-Acebes, M., Pitaval, C., Weiss, L.A., Nombela-Arrieta, C., Chèvre, R., A-González, N., Kunisaki, Y., Zhang, D., van Rooijen, N., Silberstein, L.E., et al. (2013). Rhythmic modulation of the hematopoietic niche through neutrophil clearance. Cell *153*, 1025–1035.

Cavazzana-Calvo, M., Hacein-Bey, S., de Saint Basile, G., Gross, F., Yvon, E., Nusbaum, P., Selz, F., Hue, C., Certain, S., Casanova, J.L., et al. (2000). Gene therapy of human severe combined immunodeficiency (SCID)-X1 disease. Science *288*, 669–672.

Lo Celso, C., Fleming, H.E., Wu, J.W., Zhao, C.X., Miake-Lye, S., Fujisaki, J., Côté, D., Rowe, D.W., Lin, C.P., and Scadden, D.T. (2009). Live-animal tracking of individual haematopoietic stem/progenitor cells in their niche. Nature *457*, 92–96.

Chandley, A.C. (1966). Studies on oogenesis in Drosophila melanogaster with 3H-thymidine label. Exp. Cell Res. *44*, 201–215.

Chinwalla, A.T., Cook, L.L., Delehaunty, K.D., Fewell, G.A., Fulton, L.A., Fulton, R.S., Graves, T.A., Hillier, L.W., Mardis, E.R., McPherson, J.D., et al. (2002). Initial sequencing and comparative analysis of the mouse genome. Nature *420*, 520–562.

Chung, K., Wallace, J., Kim, S.-Y., Kalyanasundaram, S., Andalman, A.S., Davidson, T.J., Mirzabekov, J.J., Zalocusky, K.A., Mattis, J., Denisin, A.K., et al. (2013). Structural and molecular interrogation of intact biological systems. Nature *497*, 332–337.

Crowley, C., Spencer, S.D., Nishimura, M.C., Chen, K.S., Pitts-Meek, S., Armanini, M.P., Ling, L.H., McMahon, S.B., Shelton, D.L., and Levinson, a D. (1994). Mice lacking nerve growth factor display perinatal loss of sensory and sympathetic neurons yet develop basal forebrain cholinergic neurons. Cell *76*, 1001–1011.

Cullum, V.A., Farmer, J.B., Jack, D., and Levy, G.P. (1969). Salbutamol: a new, selective beta-adrenoceptive receptor stimulant. Br. J. Pharmacol. *35*, 141–151.

Decotto, E., and Spradling, A.C. (2005). The Drosophila ovarian and testis stem cell niches: similar somatic stem cells and signals. Dev. Cell *9*, 501–510.

DeFalco, J., Tomishima, M., Liu, H., Zhao, C., Cai, X., Marth, J.D., Enquist, L., and Friedman, J.M. (2001). Virus-assisted mapping of neural inputs to a feeding center in the hypothalamus. Science *291*, 2608–2613.

Dexter, T.M., Allen, T.D., and Lajtha, L.G. (1977). Conditions controlling the proliferation of haemopoietic stem cells in vitro. J. Cell. Physiol. *91*, 335–344.

Ding, L., and Morrison, S.J. (2013). Haematopoietic stem cells and early lymphoid progenitors occupy distinct bone marrow niches. Nature *495*, 231–235.

Ding, L., Saunders, T.L., Enikolopov, G., and Morrison, S.J. (2012). Endothelial and perivascular cells maintain haematopoietic stem cells. Nature *481*, 457–462.

Dodt, H.-U., Leischner, U., Schierloh, A., Jährling, N., Mauch, C.P., Deininger, K., Deussing, J.M., Eder, M., Zieglgänsberger, W., and Becker, K. (2007). Ultramicroscopy: three-dimensional visualization of neuronal networks in the whole mouse brain. Nat. Methods *4*, 331–336.

Draenert, K., and Draenert, Y. (1980). The vascular system of bone marrow. Scan. Electron Microsc. 113–122.

Ertürk, A., Becker, K., Jährling, N., Mauch, C.P., Hojer, C.D., Egen, J.G., Hellal, F., Bradke, F., Sheng, M., and Dodt, H.-U. (2012). Three-dimensional imaging of solvent-cleared organs using 3DISCO. Nat. Protoc. *7*, 1983–1995.

Esler, M., Jennings, G., Lambert, G., Meredith, I., Horne, M., and Eisenhofer, G. (1990). Overflow of catecholamine neurotransmitters to the circulation: source, fate, and functions. Physiol Rev *70*, 963–985.

Fares, I., Chagraoui, J., Gareau, Y., Gingras, S., Ruel, R., Mayotte, N., Csaszar, E., Knapp, D.J.H.F., Miller, P., Ngom, M., et al. (2014). Pyrimidoindole derivatives are agonists of human hematopoietic stem cell self-renewal. Science (80-.). *345*, 1509–1512.

Ford, C.E., Hamerton, J.L., Barnes, D.W.H., and Loutit, J.F. (1956). Cytological Identification of Radiation-Chimæras. Nature *177*, 452–454.

Foudi, A., Hochedlinger, K., Van Buren, D., Schindler, J.W., Jaenisch, R., Carey, V., and Hock, H. (2009). Analysis of histone 2B-GFP retention reveals slowly cycling hematopoietic stem cells. Nat. Biotechnol. *27*, 84–90.

Friedmann, T. (1989). Progress toward human gene therapy. Science *244*, 1275–1281.

Friedmann, T., and Roblin, R. (1972). Gene therapy for human genetic disease? Science *175*, 949–955.

Fukuda, S., Bian, H., King, A.G., and Pelus, L.M. (2007). The chemokine GRObeta mobilizes early hematopoietic stem cells characterized by enhanced homing and engraftment. Blood *110*, 860–869.

Gatti, R.A., Meuwissen, H.J., Allen, H.D., Hong, R., and Good, R.A. (1968). Immunological reconstitution of sex-linked lymphopenic immunological deficiency. Lancet (London, England) *2*, 1366–1369.

Gibson, T., and Medawar, P.B. (1943). The fate of skin homografts in man. J. Anat. *77*, 299–310.4.

Gilbert, S.F. (2000). Developmental Biology.

Gómez-Casati, M.E., Murtie, J.C., Rio, C., Stankovic, K., Liberman, M.C., and Corfas, G. (2010). Nonneuronal cells regulate synapse formation in the vestibular sensory epithelium via erbB-dependent BDNF expression. Proc. Natl. Acad. Sci. U. S. A. *107*, 17005–17010.

Gragert, L., Eapen, M., Williams, E., Freeman, J., Spellman, S., Baitty, R., Hartzman, R., Rizzo, J.D., Horowitz, M., Confer, D., et al. (2014). HLA match likelihoods for hematopoietic stem-cell grafts in the U.S. registry. N. Engl. J. Med. *371*, 339–348.

Greenbaum, A., Hsu, Y.-M.S., Day, R.B., Schuettpelz, L.G., Christopher, M.J., Borgerding, J.N., Nagasawa, T., and Link, D.C. (2013). CXCL12 in early mesenchymal progenitors is required for haematopoietic stem-cell maintenance. Nature *495*, 227–230.

Gruber, H.E., Finley, K.D., Hershberg, R.M., Katzman, S.S., Laikind, P.K., Seegmiller, J.E., Friedmann, T., Yee, J.K., and Jolly, D.J. (1985). Retroviral vector-mediated gene transfer into human hematopoietic progenitor cells. Science *230*, 1057–1061.

Hacein-Bey-Abina, S. (2003). LMO2-Associated Clonal T Cell Proliferation in Two Patients after Gene Therapy for SCID-X1. Science (80-.). *302*, 415–419.

Hama, H., Kurokawa, H., Kawano, H., Ando, R., Shimogori, T., Noda, H., Fukami, K., Sakaue-Sawano, A., and Miyawaki, A. (2011). Scale: a chemical approach for fluorescence imaging and reconstruction of transparent mouse brain. Nat. Neurosci. *14*, 1481–1488.

Hanoun, M., Zhang, D., Mizoguchi, T., Pinho, S., Pierce, H., Kunisaki, Y., Lacombe, J., Armstrong, S.A., Dührsen, U., and Frenette, P.S. (2014). Acute Myelogenous Leukemia-Induced Sympathetic Neuropathy Promotes Malignancy in an Altered Hematopoietic Stem Cell Niche. Cell Stem Cell 365–375.

Hanoun, M., Maryanovich, M., Arnal-Estapé, A., and Frenette, P.S. (2015). Neural regulation of hematopoiesis, inflammation, and cancer. Neuron *86*, 360–373.

Herzog, R.W., Cao, O., and Srivastava, A. (2010). Two decades of clinical gene therapy--success is finally mounting. Discov. Med. *9*, 105–111.

Hooper, A.T., Butler, J.M., Nolan, D.J., Kranz, A., Iida, K., Kobayashi, M., Kopp, H.-G., Shido, K., Petit, I., Yanger, K., et al. (2009). Engraftment and reconstitution of hematopoiesis is dependent on VEGFR2-mediated regeneration of sinusoidal endothelial cells. Cell Stem Cell *4*, 263–274.

Hu, Y., and Smyth, G.K. (2009). ELDA: extreme limiting dilution analysis for comparing depleted and enriched populations in stem cell and other assays. J. Immunol. Methods *347*, 70–78.

Inoue, S., and Osmond, D.G. (2001). Basement membrane of mouse bone marrow sinusoids shows distinctive structure and proteoglycan composition: a high resolution ultrastructural study. Anat. Rec. *264*, 294–304.

Irizarry, R.A., Hobbs, B., Collin, F., Beazer-Barclay, Y.D., Antonellis, K.J., Scherf, U., and Speed, T.P. (2003). Exploration, normalization, and summaries of high density oligonucleotide array probe level data. Biostatistics *4*, 249–264.

Jackson, D.A., Symons, R.H., and Berg, P. (1972). Biochemical Method for Inserting New Genetic Information into DNA of Simian Virus 40: Circular SV40 DNA Molecules Containing Lambda Phage Genes and the Galactose Operon of Escherichia coli. Proc. Natl. Acad. Sci. *69*, 2904–2909.

Jacobson, L.O., Marks, E.K., Robson, M.J., Gaston, E.O., and Zirkle, R.E. (1949). Effect of spleen protection on mortality following x-irradiation. J. Lab. Clin. Med. *34*, 1538–1543.

Janssens, B., Staes, K., and van Roy, F. (1999). Human alpha-catulin, a novel alpha-catenin-like molecule with conserved genomic structure, but deviating alternative splicing. Biochim. Biophys. Acta *1447*, 341–347.

Katayama, Y., Battista, M., Kao, W.-M., Hidalgo, A., Peired, A.J., Thomas, S. a, and Frenette, P.S. (2006). Signals from the sympathetic nervous system regulate hematopoietic stem cell egress from bone marrow. Cell *124*, 407–421.

Kelly, J.J., and Karcher, D.S. (2005). Lymphoma and peripheral neuropathy: a clinical review. Muscle Nerve *31*, 301–313.

Kiel, M.J., Yilmaz, O.H., Iwashita, T., Terhorst, C., and Morrison, S.J. (2005). SLAM family receptors distinguish hematopoietic stem and progenitor cells and reveal endothelial niches for stem cells. Cell *121*, 1109–1121.

Kiel, M.J., Radice, G.L., and Morrison, S.J. (2007a). Lack of evidence that hematopoietic stem cells depend on N-cadherin-mediated adhesion to osteoblasts for their maintenance. Cell Stem Cell *1*, 204–217.

Kiel, M.J., He, S., Ashkenazi, R., Gentry, S.N., Teta, M., Kushner, J.A., Jackson, T.L., and Morrison, S.J. (2007b). Haematopoietic stem cells do not asymmetrically segregate chromosomes or retain BrdU. Nature *449*, 238–242.

Kiel, M.J., Acar, M., Radice, G.L., and Morrison, S.J. (2009). Hematopoietic stem cells do not depend on N-cadherin to regulate their maintenance. Cell Stem Cell *4*, 170–179.

Kobayashi, H., Butler, J.M., O'Donnell, R., Kobayashi, M., Ding, B.-S., Bonner, B., Chiu, V.K., Nolan, D.J., Shido, K., Benjamin, L., et al. (2010). Angiocrine factors from Akt-activated endothelial cells balance self-renewal and differentiation of haematopoietic stem cells. Nat. Cell Biol.

Koch, E.A., and King, R.C. (1966). The origin and early differentiation of the egg chamber of Drosophila melanogaster. J. Morphol. *119*, 283–303.

Kopp, H.-G., Hooper, A.T., Avecilla, S.T., and Rafii, S. (2009). Functional heterogeneity of the bone marrow vascular niche. Ann. N. Y. Acad. Sci. *1176*, 47–54.

Kotova, P.D., Turin-Kuzmin, P.A., Rogachevskaja, O.A., Fadeeva, J.I., Sysoeva, V.Y., Tkachuk, V.A., and Kolesnikov, S.S. (2014). Calcium-induced calcium release mediates all-or-nothing responses of mesenchymal stromal cells to noradrenaline. Biochem. Suppl. Ser. A Membr. Cell Biol. *8*, 82–88.

Kunisaki, Y., Bruns, I., Scheiermann, C., Ahmed, J., Pinho, S., Zhang, D., Mizoguchi, T., Wei, Q., Lucas, D., Ito, K., et al. (2013). Arteriolar niches maintain haematopoietic stem cell quiescence. Nature *502*, 637–643.

Li, L., and Clevers, H. (2010). Coexistence of quiescent and active adult stem cells in mammals. Science *327*, 542–545.

Li, P., and Zon, L.I. (2010). Resolving the controversy about N-cadherin and hematopoietic stem cells. Cell Stem Cell *6*, 199–202.

Li, X.-M., Hu, Z., Jorgenson, M.L., Wingard, J.R., and Slayton, W.B. (2008). Bone marrow sinusoidal endothelial cells undergo nonapoptotic cell death and are replaced by proliferating sinusoidal cells in situ to maintain the vascular niche following lethal irradiation. Exp. Hematol. *36*, 1143–1156.

Li, X.-M., Hu, Z., Jorgenson, M.L., and Slayton, W.B. (2009). High levels of acetylated low-density lipoprotein uptake and low tyrosine kinase with immunoglobulin and epidermal growth factor homology domains-2 (Tie2) promoter activity distinguish sinusoids from other vessel types in murine bone marrow. Circulation *120*, 1910–1918.

Lichtman, M.A., Chamberlain, J.K., Simon, W., and Santillo, P.A. (1978). Parasinusoidal location of megakaryocytes in marrow: a determinant of platelet release. Am. J. Hematol. *4*, 303–312.

Lin, H., and Spradling, A.C. (1993). Germline stem cell division and egg chamber development in transplanted Drosophila germaria. Dev. Biol. *159*, 140–152.

Lindsay, R.M. (1988). Nerve growth factors (NGF, BDNF) enhance axonal regeneration but are not required for survival of adult sensory neurons. J. Neurosci. *8*, 2394–2405.

Liu, P., Jenkins, N.A., and Copeland, N.G. (2003). A highly efficient recombineering-based method for generating conditional knockout mutations. Genome Res. *13*, 476–484.

Logan, M., Martin, J.F., Nagy, A., Lobe, C., Olson, E.N., and Tabin, C.J. (2002). Expression of Cre Recombinase in the developing mouse limb bud driven by a Prxl enhancer. Genesis *33*, 77–80.

Lord, B.I., and Hendry, J.H. (1972). The distribution of haemopoietic colony-forming units in the mouse femur, and its modification by x rays. Br. J. Radiol. *45*, 110–115.

Lord, B.I., Testa, N.G., and Hendry, J.H. (1975). The relative spatial distributions of CFUs and CFUc in the normal mouse femur. Blood *46*, 65–72.

Lorenz, E., Uphoff, D., Reid, T.R., and Shelton, E. (1951). Modification of irradiation injury in mice and guinea pigs by bone marrow injections. J. Natl. Cancer Inst. *12*, 197–201.

Lucas, D., Battista, M., Shi, P.A., Isola, L., and Frenette, P.S. (2008). Mobilized hematopoietic stem cell yield depends on species-specific circadian timing. Cell Stem Cell *3*, 364–366.

Lucas, D., Scheiermann, C., Chow, A., Kunisaki, Y., Bruns, I., Barrick, C., Tessarollo, L., and Frenette, P.S. (2013). Chemotherapy-induced bone marrow nerve injury impairs hematopoietic regeneration. Nat. Med. *19*, 695–703.

Lymperi, S., Horwood, N., Marley, S., Gordon, M.Y., Cope, A.P., and Dazzi, F. (2008). Strontium can increase some osteoblasts without increasing hematopoietic stem cells. Blood *111*, 1173–1181.

Ma, L., Lopez, G.F., and Krimm, R.F. (2009). Epithelial-derived brain-derived neurotrophic factor is required for gustatory neuron targeting during a critical developmental period. J. Neurosci. *29*, 3354–3364.

Madisen, L., Zwingman, T.A., Sunkin, S.M., Oh, S.W., Zariwala, H.A., Gu, H., Ng, L.L., Palmiter, R.D., Hawrylycz, M.J., Jones, A.R., et al. (2010). A robust and high-throughput Cre reporting and characterization system for the whole mouse brain. Nat. Neurosci. *13*, 133–140.

Main, J.M., and Prehn, R.T. (1955). Successful skin homografts after the administration of high dosage X radiation and homologous bone marrow. J. Natl. Cancer Inst. *15*, 1023–1029.

Malide, D., Métais, J.-Y., and Dunbar, C.E. (2012). Dynamic clonal analysis of murine hematopoietic stem and progenitor cells marked by 5 fluorescent proteins using confocal and multiphoton microscopy. Blood *120*, e105–e116.

Margolis, J., and Spradling, A. (1995). Identification and behavior of epithelial stem cells in the Drosophila ovary. Development *121*, 3797–3807.

Mathe, G., Amiel, J.L., Schwarzenberg, L., Cattan, A., and Schneider, M. (1963). HAEMATOPOIETIC CHIMERA IN MAN AFTER ALLOGENIC (HOMOLOGOUS) BONE-MARROW TRANSPLANTATION. (CONTROL OF THE SECONDARY SYNDROME. SPECIFIC TOLERANCE DUE TO THE CHIMERISM). Br. Med. J. *2*, 1633–1635.

Mayo Clinic (2015). Volumes and Success Measures - Bone Marrow Transplant - Mayo Clinic.

Medawar, P.B. (1944). The behaviour and fate of skin autografts and skin homografts in rabbits: A report to the War Wounds Committee of the Medical Research Council. J. Anat. *78*, 176–199.

Méndez-Ferrer, S., Lucas, D., Battista, M., and Frenette, P.S. (2008). Haematopoietic stem cell release is regulated by circadian oscillations. Nature *452*, 442–447.

Méndez-Ferrer, S., Battista, M., and Frenette, P.S. (2010a). Cooperation of beta(2)- and beta(3)-adrenergic receptors in hematopoietic progenitor cell mobilization. Ann. N. Y. Acad. Sci. *1192*, 139–144.

Méndez-Ferrer, S., Michurina, T. V., Ferraro, F., Mazloom, A.R., MacArthur, B.D., Lira, S.A., Scadden, D.T., Ma'ayan, A., Enikolopov, G.N., and Frenette, P.S. (2010b). Mesenchymal and haematopoietic stem cells form a unique bone marrow niche. Nature *466*, 829–834.

Micali, G. (1993). The Italian contribution to plastic surgery. Ann. Plast. Surg. *31*, 566–571.

Molineux, G., Foote, M., and Arvedson, T. (2012). Twenty Years of G-CSF: Clinical and Nonclinical Discoveries (Springer Science & Business Media).

Molinoff, P.B. (1984). Alpha- and beta-adrenergic receptor subtypes properties, distribution and regulation. Drugs *28 Suppl 2*, 1–15.

Morikawa, S., Mabuchi, Y., Kubota, Y., Nagai, Y., Niibe, K., Hiratsu, E., Suzuki, S., Miyauchi-Hara, C., Nagoshi, N., Sunabori, T., et al. (2009). Prospective identification, isolation, and systemic transplantation of multipotent mesenchymal stem cells in murine bone marrow. J. Exp. Med. *206*, 2483–2496.

Morita, Y., Ema, H., and Nakauchi, H. (2010). Heterogeneity and hierarchy within the most primitive hematopoietic stem cell compartment. J. Exp. Med. *207*, 1173–1182.

Morris, J.B., and Schirmer, W.J. (1990). The "right stuff": five Nobel Prize-winning surgeons. Surgery *108*, 71–80.

Morrison, S.J., and Scadden, D.T. (2014). The bone marrow niche for haematopoietic stem cells. Nature *505*, 327–334.

Morrison, S.J., Uchida, N., and Weissman, I.L. (1995). The biology of hematopoietic stem cells. Annu. Rev. Cell Dev. Biol. *11*, 35–71.

Naldini, L. (2009). A Comeback for Gene Therapy. *326*.

Ng, Y.Y., Baert, M.R.M., de Haas, E.F.E., Pike-Overzet, K., and Staal, F.J.T. (2009). Isolation of human and mouse hematopoietic stem cells. Methods Mol. Biol. *506*, 13–21.

Nilsson, S.K., Johnston, H.M., and Coverdale, J.A. (2001). Spatial localization of transplanted hemopoietic stem cells: inferences for the localization of stem cell niches. Blood *97*, 2293–2299.

Nombela-Arrieta, C., Pivarnik, G., Winkel, B., Canty, K.J., Harley, B., Mahoney, J.E., Park, S.-Y., Lu, J., Protopopov, A., and Silberstein, L.E. (2013). Quantitative imaging of haematopoietic stem and progenitor cell localization and hypoxic status in the bone marrow microenvironment. Nat. Cell Biol. *15*, 533–543.

Norkin, M., Lazarus, H.M., and Wingard, J.R. (2012). Umbilical cord blood graft enhancement strategies: has the time come to move these into the clinic? Bone Marrow Transplant. 1–6.

Notta, F., Doulatov, S., Laurenti, E., Poeppl, A., Jurisica, I., and Dick, J.E. (2011). Isolation of single human hematopoietic stem cells capable of long-term multilineage engraftment. Science *333*, 218–221.

Oguro, H., Ding, L., and Morrison, S.J. (2013). SLAM family markers resolve functionally distinct subpopulations of hematopoietic stem cells and multipotent progenitors. Cell Stem Cell *13*, 102–116.

Omatsu, Y., Sugiyama, T., Kohara, H., Kondoh, G., Fujii, N., Kohno, K., and Nagasawa, T. (2010). The Essential Functions of Adipo-osteogenic Progenitors as the Hematopoietic Stem and Progenitor Cell Niche. Immunity *33*, 387–399.

Omatsu, Y., Seike, M., Sugiyama, T., Kume, T., and Nagasawa, T. (2014). Foxc1 is a critical regulator of haematopoietic stem/progenitor cell niche formation. Nature *508*, 536–540.

Owen, R.D. (1945). IMMUNOGENETIC CONSEQUENCES OF VASCULAR ANASTOMOSES BETWEEN BOVINE TWINS. Science *102*, 400–401.

Ozdemir, O., Soylu, M., Alyan, O., Geyik, B., Demir, A.D., Aras, D., Cihan, G., Cagirci, G., Kacmaz, F., Balbay, Y., et al. (2004). Association between mean platelet volume and autonomic nervous system functions: Increased mean platelet volume reflects sympathetic overactivity. Exp. Clin. Cardiol. *9*, 243–247.

Park, B., Nguyen, N.T., Dutt, P., Merdek, K.D., Bashar, M., Sterpetti, P., Tosolini, A., Testa, J.R., and Toksoz, D. (2002). Association of Lbc Rho guanine nucleotide exchange factor with alpha-catenin-related protein, alpha-catulin/CTNNAL1, supports serum response factor activation. J. Biol. Chem. *277*, 45361–45370.

Parmar, K., Mauch, P., Vergilio, J.-A., Sackstein, R., and Down, J.D. (2007). Distribution of hematopoietic stem cells in the bone marrow according to regional hypoxia. Proc. Natl. Acad. Sci. U. S. A. *104*, 5431–5436.

Patapoutian, A., and Reichardt, L.F. (2001). Trk receptors: mediators of neurotrophin action. Curr. Opin. Neurobiol. *11*, 272–280.

Pawliuk, R., Eaves, C., and Humphries, R.K. (1996). Evidence of both ontogeny and transplant dose-regulated expansion of hematopoietic stem cells in vivo. Blood *88*, 2852–2858.

Pelus, L.M., and Fukuda, S. (2008). Chemokine-mobilized adult stem cells; defining a better hematopoietic graft. Leukemia *22*, 466–473.

Ploemacher, R.E., van der Sluijs, J.P., Voerman, J.S., and Brons, N.H. (1989). An in vitro limiting-dilution assay of long-term repopulating hematopoietic stem cells in the mouse. Blood *74*, 2755–2763.

Pongratz, G., and Straub, R.H. (2014). The sympathetic nervous response in inflammation. Arthritis Res. Ther. *16*, 504.

Poulos, M.G., Guo, P., Kofler, N.M., Pinho, S., Gutkin, M.C., Tikhonova, A., Aifantis, I., Frenette, P.S., Kitajewski, J., Rafii, S., et al. (2013). Endothelial Jagged-1 is necessary for homeostatic and regenerative hematopoiesis. Cell Rep. *4*, 1022–1034.

Powles, R.L., Barrett, A.J., Clink, H., Kay, H.E., Sloane, J., and McElwain, T.J. (1978). Cyclosporin A for the treatment of graft-versus-host disease in man. Lancet (London, England) *2*, 1327–1331.

Rafii, S., Shapiro, F., Rimarachin, J., Nachman, R.L., Ferris, B., Weksler, B., Moore, M.A., and Asch, A.S. (1994). Isolation and characterization of human bone marrow microvascular endothelial cells: hematopoietic progenitor cell adhesion. Blood *84*, 10–19.

Rafii, S., Shapiro, F., Pettengell, R., Ferris, B., Nachman, R.L., Moore, M.A., and Asch, A.S. (1995). Human bone marrow microvascular endothelial cells support

long-term proliferation and differentiation of myeloid and megakaryocytic progenitors. Blood *86*, 3353–3363.

Rafii, S., Mohle, R., Shapiro, F., Frey, B.M., and Moore, M.A. (1997). Regulation of hematopoiesis by microvascular endothelium. Leuk. Lymphoma *27*, 375–386.

Reiss, K., Maretzky, T., Ludwig, A., Tousseyn, T., de Strooper, B., Hartmann, D., and Saftig, P. (2005). ADAM10 cleavage of N-cadherin and regulation of cell-cell adhesion and beta-catenin nuclear signalling. EMBO J. *24*, 742–752.

Renier, N., Wu, Z., Simon, D.J., Yang, J., Ariel, P., and Tessier-Lavigne, M. (2014). iDISCO: A Simple, Rapid Method to Immunolabel Large Tissue Samples for Volume Imaging. Cell *159*, 896–910.

Rodríguez, C.I., Buchholz, F., Galloway, J., Sequerra, R., Kasper, J., Ayala, R., Stewart, A.F., and Dymecki, S.M. (2000). High-efficiency deleter mice show that FLPe is an alternative to Cre-loxP. Nat. Genet. *25*, 139–140.

Ronen, K., Negre, O., Roth, S., Colomb, C., Malani, N., Denaro, M., Brady, T., Fusil, F., Gillet-Legrand, B., Hehir, K., et al. (2011). Distribution of lentiviral vector integration sites in mice following therapeutic gene transfer to treat β-thalassemia. Mol. Ther. *19*, 1273–1286.

Rossant, J., and McMahon, A. (1999). “Cre”-ating mouse mutants---a meeting review on conditional mouse genetics. Genes Dev. *13*, 142–145.

Sacchetti, B., Funari, A., Michienzi, S., Di Cesare, S., Piersanti, S., Saggio, I., Tagliafico, E., Ferrari, S., Robey, P.G., Riminucci, M., et al. (2007). Self-renewing osteoprogenitors in bone marrow sinusoids can organize a hematopoietic microenvironment. Cell *131*, 324–336.

Schofield, R. (1978). The relationship between the spleen colony-forming cell and the haemopoietic stem cell. Blood Cells *4*, 7–25.

Schroeder, C., and Jordan, J. (2012). Norepinephrine transporter function and human cardiovascular disease. Am. J. Physiol. Heart Circ. Physiol. *303*, H1273–H1282.

Schupbach, T., Wieschaus, E., and Nothiger, R. (1978). A study of the female germ line in mosaics ofDrosophila. Wilhelm Roux’s Arch. Dev. Biol. *184*, 41–56.

Sharkis, S.J., Wiktor-Jedrzejczak, W., Ahmed, A., Santos, G.W., McKee, A., and Sell, K.W. (1978). Antitheta-sensitive regulatory cell (TSRC) and hematopoiesis:

regulation of differentiation of transplanted stem cells in W/Wv anemic and normal mice. Blood *52*, 802–817.

Shiffman, M., and Di Giuseppe, A. (2013). Advanced Aesthetic Rhinoplasty: Art, Science, and New Clinical Techniques. (Springer Science & Business Media.).

Siminovitch, L., McCulloch, E.A., and Till, J.E. (1963). The distribution of colony-forming cells among spleen colonies. J. Cell. Comp. Physiol. *62*, 327–336.

Sipkins, D. a, Wei, X., Wu, J.W., Runnels, J.M., Côté, D., Means, T.K., Luster, A.D., Scadden, D.T., and Lin, C.P. (2005). In vivo imaging of specialized bone marrow endothelial microdomains for tumour engraftment. Nature *435*, 969–973.

Song, X., and Xie, T. (2002). DE-cadherin-mediated cell adhesion is essential for maintaining somatic stem cells in the Drosophila ovary. Proc. Natl. Acad. Sci. U. S. A. *99*, 14813–14818.

Song, X., and Xie, T. (2003). Wingless signaling regulates the maintenance of ovarian somatic stem cells in Drosophila. Development *130*, 3259–3268.

Spencer, J.A., Ferraro, F., Roussakis, E., Klein, A., Wu, J., Runnels, J.M., Zaher, W., Mortensen, L.J., Alt, C., Turcotte, R., et al. (2014). Direct measurement of local oxygen concentration in the bone marrow of live animals. Nature *508*, 269–273.

Srinivas, S., Watanabe, T., Lin, C.S., William, C.M., Tanabe, Y., Jessell, T.M., and Costantini, F. (2001). Cre reporter strains produced by targeted insertion of EYFP and ECFP into the ROSA26 locus. BMC Dev. Biol. *1*, 4.

Stolberg, S.G. (1999). The Biotech Death of Jesse Gelsinger. New York Times.

Straub, R.H., Wiest, R., Strauch, U.G., Härle, P., and Schölmerich, J. (2006). The role of the sympathetic nervous system in intestinal inflammation. Gut *55*, 1640–1649.

Sugimura, R., He, X.C., Venkatraman, A., Arai, F., Box, A., Semerad, C., Haug, J.S., Peng, L., Zhong, X.-B., Suda, T., et al. (2012). Noncanonical Wnt signaling maintains hematopoietic stem cells in the niche. Cell *150*, 351–365.

Sugiyama, T., Kohara, H., Noda, M., and Nagasawa, T. (2006a). Maintenance of the hematopoietic stem cell pool by CXCL12-CXCR4 chemokine signaling in bone marrow stromal cell niches. Immunity *25*, 977–988.

Sugiyama, T., Kohara, H., Noda, M., and Nagasawa, T. (2006b). Maintenance of the hematopoietic stem cell pool by CXCL12-CXCR4 chemokine signaling in bone marrow stromal cell niches. Immunity *25*, 977–988.

Susaki, E.A., Tainaka, K., Perrin, D., Kishino, F., Tawara, T., Watanabe, T.M., Yokoyama, C., Onoe, H., Eguchi, M., Yamaguchi, S., et al. (2014). Whole-brain imaging with single-cell resolution using chemical cocktails and computational analysis. Cell *157*, 726–739.

Tagliacozzi, G. (1597). Gasparis Taliacotii... De curtorum chirurgia per insitionem libri duo... (apud Gasparem Bindonum iuniorem).

Taichman, R.S., and Emerson, S.G. (1994). Human osteoblasts support hematopoiesis through the production of granulocyte colony-stimulating factor. J. Exp. Med. *179*, 1677–1682.

Takaku, T., Malide, D., Chen, J., Calado, R.T., Kajigaya, S., and Young, N.S. (2010). Hematopoiesis in 3 dimensions: human and murine bone marrow architecture visualized by confocal microscopy. Blood *116*, e41–e55.

Takefman, D., and Bryan, W. (2012). The state of gene therapies: the FDA perspective. Mol. Ther. *20*, 877–878.

Tamplin, O.J., Durand, E.M., Carr, L.A., Childs, S.J., Hagedorn, E.J., Li, P., Yzaguirre, A.D., Speck, N.A., and Zon, L.I. (2015). Hematopoietic Stem Cell Arrival Triggers Dynamic Remodeling of the Perivascular Niche. Cell *160*, 241–252.

Terenghi, G. (1999). Peripheral nerve regeneration and neurotrophic factors. J. Anat. *194 (Pt 1*, 1–14.

Tesfaye, S., and Selvarajah, D. (2012). Advances in the epidemiology, pathogenesis and management of diabetic peripheral neuropathy. Diabetes. Metab. Res. Rev. *28 Suppl 1*, 8–14.

Thomas, E.D., Lochte, H.L., Lu, W.C., and Ferrebee, J.W. (1957). Intravenous infusion of bone marrow in patients receiving radiation and chemotherapy. N. Engl. J. Med. *257*, 491–496.

Thomas, E.D., Lochte, H.L., Cannon, J.H., Sahler, O.D., and Ferrebee, J.W. (1959). Supralethal whole body irradiation and isologous marrow transplantation in man. J. Clin. Invest. *38*, 1709–1716.

Thomas, E.D., Collins, J.A., Herman, E.C., and Ferrebee, J.W. (1962). Marrow transplants in lethally irradiated dogs given methotrexate. Blood *19*, 217–228.

Thomas, E.D., Storb, R., Clift, R.A., Fefer, A., Johnson, F.L., Neiman, P.E., Lerner, K.G., Glucksberg, H., and Buckner, C.D. (1975). Bone-marrow transplantation (first of two parts). N. Engl. J. Med. *292*, 832–843.

Thrasher, A.J., Gaspar, H.B., Baum, C., Modlich, U., Schambach, A., Candotti, F., Otsu, M., Sorrentino, B., Scobie, L., Cameron, E., et al. (2006). Gene therapy: X-SCID transgene leukaemogenicity. Nature *443*, E5–E6; discussion E6–E7.

Till, J.E., and McCulloch, E.A. (1961). A direct measurement of the radiation sensitivity of normal mouse bone marrow cells. Radiat. Res. *14*, 213–222.

Travlos, G.S. (2006). Normal structure, function, and histology of the bone marrow. Toxicol. Pathol. *34*, 548–565.

Tubsuwan, A., Abed, S., Deichmann, A., Kardel, M.D., Bartholomä, C., Cheung, A., Negre, O., Kadri, Z., Fucharoen, S., von Kalle, C., et al. (2013). Parallel assessment of globin lentiviral transfer in induced pluripotent stem cells and adult hematopoietic stem cells derived from the same transplanted β-thalassemia patient. Stem Cells *31*, 1785–1794.

Visnjic, D., Kalajzic, Z., Rowe, D.W., Katavic, V., Lorenzo, J., and Aguila, H.L. (2004). Hematopoiesis is severely altered in mice with an induced osteoblast deficiency. Blood *103*, 3258–3264.

Walasek, M. a, van Os, R., and de Haan, G. (2012). Hematopoietic stem cell expansion: challenges and opportunities. Ann. N. Y. Acad. Sci. *1266*, 138–150.

Wan, G., Gómez-Casati, M.E., Gigliello, A.R., Liberman, M.C., and Corfas, G. (2014). Neurotrophin-3 regulates ribbon synapse density in the cochlea and induces synapse regeneration after acoustic trauma. Elife *3*.

Wang, L.D., and Wagers, A.J. (2011). Dynamic niches in the origination and differentiation of haematopoietic stem cells. Nat. Rev. Mol. Cell Biol. *12*, 643–655.

Wieschaus, E., and Szabad, J. (1979). The development and function of the female germ line in Drosophila melanogaster: A cell lineage study. Dev. Biol. *68*, 29–46.

Wilson, A., and Trumpp, A. (2006). Bone-marrow haematopoietic-stem-cell niches. Nat. Rev. Immunol. *6*, 93–106.

Wilson, A., Laurenti, E., and Trumpp, A. (2009). Balancing dormant and self-renewing hematopoietic stem cells. Curr. Opin. Genet. Dev. *19*, 461–468.

Woods, N.-B., Bottero, V., Schmidt, M., von Kalle, C., and Verma, I.M. (2006). Gene therapy: therapeutic gene causing lymphoma. Nature *440*, 1123.

Xie, T., and Spradling, A.C. (1998). decapentaplegic is essential for the maintenance and division of germline stem cells in the Drosophila ovary. Cell *94*, 251–260.

Xie, T., and Spradling, A.C. (2000). A niche maintaining germ line stem cells in the Drosophila ovary. Science *290*, 328–330.

Yamashita, Y.M., Fuller, M.T., and Jones, D.L. (2005). Signaling in stem cell niches: lessons from the Drosophila germline. J. Cell Sci. *118*, 665–672.

Yamazaki, K., and Allen, T.D. (1990). Ultrastructural morphometric study of efferent nerve terminals on murine bone marrow stromal cells, and the recognition of a novel anatomical unit: the “neuro-reticular complex”. Am. J. Anat. *187*, 261–276.

Yamazaki, S., Ema, H., Karlsson, G., Yamaguchi, T., Miyoshi, H., Shioda, S., Taketo, M.M., Karlsson, S., Iwama, A., and Nakauchi, H. (2011). Nonmyelinating Schwann Cells Maintain Hematopoietic Stem Cell Hibernation in the Bone Marrow Niche. Cell *147*, 1146–1158.

Yang, B., Treweek, J.B., Kulkarni, R.P., Deverman, B.E., Chen, C.-K., Lubeck, E., Shah, S., Cai, L., and Gradinaru, V. (2014). Single-Cell Phenotyping within Transparent Intact Tissue through Whole-Body Clearing. Cell *158*, 945–958.

Yokomizo, T., Yamada-Inagawa, T., Yzaguirre, A.D., Chen, M.J., Speck, N.A., and Dzierzak, E. (2012). Whole-mount three-dimensional imaging of internally localized immunostained cells within mouse embryos. Nat. Protoc. *7*, 421–431.

Zhang, J., Niu, C., Ye, L., Huang, H., He, X., Tong, W.-G., Ross, J., Haug, J., Johnson, T., Feng, J.Q., et al. (2003). Identification of the haematopoietic stem cell niche and control of the niche size. Nature *425*, 836–841.

Zhou, B.O., Yue, R., Murphy, M.M., Peyer, J.G., and Morrison, S.J. (2014). Leptin-receptor-expressing mesenchymal stromal cells represent the main source of bone formed by adult bone marrow. Cell Stem Cell *15*, 154–168.

Zhou, B.O., Ding, L., and Morrison, S.J. (2015). Hematopoietic stem and progenitor cells regulate the regeneration of their niche by secreting Angiopoietin-1. Elife *4*, e05521.

Zhu, D., Larin, K. V, Luo, Q., and Tuchin, V. V (2013). Recent progress in tissue optical clearing. Laser Photon. Rev. *7*, 732–757.

Zhu, J., Garrett, R., Jung, Y., Zhang, Y., Kim, N., Wang, J., Joe, G.J., Hexner, E., Choi, Y., Taichman, R.S., et al. (2007). Osteoblasts support B-lymphocyte commitment and differentiation from hematopoietic stem cells. Blood *109*, 3706–3712.

Zhu, X., Hill, R.A., Dietrich, D., Komitova, M., Suzuki, R., and Nishiyama, A. (2011). Age-dependent fate and lineage restriction of single NG2 cells. Development *138*, 745–753.

Zou, Y.R., Kottmann, A.H., Kuroda, M., Taniuchi, I., and Littman, D.R. (1998). Function of the chemokine receptor CXCR4 in haematopoiesis and in cerebellar development. Nature *393*, 595–599.